Centre Énergie, Matériaux et Télécommunications (INRS-EMT)

ACCÉLÉRATION DE L'IMAGERIE PAR GÉNÉRATION DE SECONDE HARMONIQUE RÉSOLUE EN POLARISATION À L'AIDE DE MÉTHODES D'AMÉLIORATION DE RÉSOLUTION BASÉES SUR L'APPRENTISSAGE AUTOMATIQUE

Par

Melika Sadat Mohammadi

Mémoire présenté pour l'obtention du grade de

Maître ès Sciences, M.Sc.

en sciences de l'énergie et des matériaux

Jury d'évaluation

Président du jury et examinateur interne	Tsuneyuki Ozaki INRS
Examinateur externe	Cameron Brown Queensland University of Technology (QUT)
Directeur de recherche	François Légaré INRS

ACKNOWLEDGEMENTS

The journey of writing this thesis has been an incredible learning experience, filled with challenges, discoveries, and growth. The completion of this work marks an important milestone in my academic path and brings me one step closer to my future aspirations.

First and foremost, I would like to express my deepest gratitude to my supervisor, Professor François Légaré, for his invaluable guidance, encouragement, and unwavering support throughout my research. His expertise and mentorship have played a crucial role in shaping this work.

I am also sincerely grateful to Dr. Arash Aghigh for his insightful teachings and guidance, which have greatly contributed to my research. His support and dedication have been truly inspiring. Additionally, I extend my heartfelt thanks to Dr. Maghsoud Arshadi for his continuous support, encouragement, and valuable advice throughout my master's studies.

I am deeply thankful to my parents and friends for their unwavering support, patience, and encouragement. Their belief in me has been a constant source of motivation, and I am truly grateful for their presence throughout this journey.

With sincere gratitude,

Melika Sadat Mohammadi

ABSTRACT

Polarization-resolved second-harmonic generation (P-SHG) microscopy has been increasingly used as a valuable tool to study the structure and optical features of non-symmetric biological materials, such as collagen fibers. Nevertheless, there are some practical limitations to using regular P-SHG imaging for whole biological samples, including long acquisition times, high-resolution equipment expenses, and the risk of laser-induced photodamage during imaging.

To overcome these limitations, in this thesis, we developed and tested a new way of enhancing images. This approach employs the super-resolution generative adversarial networks (ESRGAN) to clarify low-resolution P-SHG images with their structure and accuracy intact. With this deep learning technique, we reduced the imaging time from 4.5 hours to merely 13.5 minutes - a more than 95% enhancement - without compromising image quality. Using no-reference and full-reference metrics such as MS-SSIM, PSNR, and NRMSE, extensive testing demonstrated that this approach consistently preserves the key structural features necessary for biological analysis.

This approach was applied to imaging whole mammary gland samples, where precise evaluation of collagen fiber anisotropy and orientation is crucial for understanding tissue architecture and identifying pathological modification. Upscaled images indicated incredible compatibility with advanced analytical techniques such as CurveAlign, allowing for exact evaluations of collagen structures. This technique improved imaging speed and quality while also reducing laser exposure, preventing sample damage, and preserving tissue chemical and morphological integrity. Furthermore, the ability to use low-cost optical components significantly decreased the financial barriers to using P-SHG microscopy.

The ESRGAN-based approach has diverse applications, including large-scale imaging, clinical diagnostics, and tissue engineering. However, problems persist, such as dependency on high-resolution training datasets and unexpected smoothing effects which hide finer internal structural differences. Future research could address

these limitations by creating general models that learn directly from low-resolution information and using domain-specific restrictions to improve structural fidelity.

In conclusion, this thesis offers an innovative framework for high-resolution, high-throughput P-SHG microscopy that overcomes typical trade-offs between speed, resolution, and preventing sample damage. The proposed method has the potential to improve biological imaging by enabling fast, low-cost, and high-quality image acquisition, with major implications for biomedical applications.

Keywords: Polarization-resolved second harmonic generation (P-SHG); Deep learning; Super-resolution generative adversarial networks (ESRGAN); Collagen analysis; High-throughput imaging; Mammary gland development; Biological imaging; Structural fidelity.

RÉSUMÉ

La microscopie par génération de second harmonique résolu en polarisation (GSH-P) s'est imposée comme un outil précieux pour étudier la structure et les propriétés optiques des matériaux biologiques non-centrosymétriques, tels que les fibres de collagène. Cependant, l'utilisation classique de la microscopie GSH-P pour des échantillons biologiques entiers présente des limitations pratiques, notamment des temps d'acquisition prolongés, le coût élevé des équipements à haute résolution, et le risque de photo-dommages induits par le laser au cours de l'imagerie.

Pour surmonter ces obstacles, ce mémoire propose et évalue une méthode innovante d'amélioration d'images. Cette approche s'appuie sur les réseaux de génération adversariales (GAN) à super-résolution (ESRGAN) pour clarifier les images GSH-P à faible résolution tout en préservant leur structure et leur précision. Grâce à cette technique d'apprentissage profond, le temps d'imagerie a été réduit de 4.5 heures à seulement 13.5 minutes, soit une amélioration de plus de 95 %, sans compromis sur la qualité des images. Une évaluation approfondie, utilisant des métriques sans référence et avec référence telles que MS-SSIM, PSNR et NRMSE, a démontré que cette méthode conserve systématiquement les caractéristiques structurelles clés nécessaires à l'analyse biologique.

Cette méthode a été appliquée à l'imagerie d'échantillons entiers de glandes mammaires, où l'évaluation précise de l'anisotropie et de l'orientation des fibres de collagène est essentielle pour comprendre l'architecture tissulaire et identifier les modifications pathologiques. Les images revalorisées ont montré une excellente compatibilité avec des techniques analytiques avancées telles que CurveAlign, permettant une évaluation précise des structures de collagène. Cette technique a permis d'améliorer simultanément la vitesse et la qualité de l'imagerie tout en réduisant l'exposition au laser, en prévenant les dommages aux échantillons et en préservant l'intégrité chimique et morphologique des tissus. De plus, la possibilité d'utiliser des composants optiques à faible coût a considérablement diminué les barrières financières à l'adoption de la microscopie GSH-P.

L’approche basée sur ESRGAN offre des applications variées, y compris l’imagerie à grande échelle, le diagnostic clinique et l’ingénierie tissulaire. Cependant, certaines limitations subsistent, comme la dépendance aux ensembles de données d’entraînement haute résolution et les effets de lissage inattendus qui peuvent masquer des variations internes plus fines des structures. Les recherches futures pourraient résoudre ces limites en développant des modèles généraux capables d’apprendre directement à partir de données basse résolution et en intégrant des contraintes spécifiques au domaine pour améliorer la fidélité structurelle.

En conclusion, ce mémoire propose un cadre novateur pour l’imagerie GSH-P à haute résolution et à haut débit, qui surmonte les compromis habituels entre vitesse, résolution et sécurité des échantillons. La méthode proposée a le potentiel d’améliorer considérablement l’imagerie biologique en permettant une acquisition rapide, économique et de haute qualité des images, avec des implications majeures pour la recherche et les applications médicales.

Mots-clés: Génération de second harmonique résolu en polarisation (GSH-P) ; Apprentissage profond ; Réseaux antagonistes génératifs à super-résolution (ESRGAN) ; Analyse du collagène ; Imagerie à haut débit ; Développement de la glande mammaire ; Imagerie biologique ; Fidélité structurelle.

SYNOPSIS

Au cours de mon programme de maîtrise sous la supervision du Professeur François Légaré, j'ai travaillé sur un projet combinant l'optique non linéaire et l'intelligence artificielle pour améliorer les techniques d'imagerie biologique. Avant de commencer ce programme, mon expérience avec les méthodes optiques avancées était limitée. Au cours des deux dernières années, ce projet m'a permis d'acquérir une expertise approfondie en microscopie non linéaire et en apprentissage profond. Plus précisément, mes recherches se sont concentrées sur le développement d'une approche innovante d'imagerie par génération de second harmonique polarisée (GSH-P) pour l'étude des tissus biologiques, en particulier les fibres de collagène.

L'imagerie GSH-P a émergé comme un outil essentiel pour étudier les propriétés structurelles des tissus biologiques non centrosymétriques, tels que les fibres de collagène. Malgré ses capacités avérées, les techniques d'imagerie GSH-P conventionnelles rencontrent des défis importants, notamment des temps d'acquisition prolongés, la nécessité d'équipements coûteux à haute résolution, et le risque de photo-dommages aux échantillons biologiques sensibles pendant l'imagerie. Ces limitations ont freiné l'adoption plus large de l'imagerie GSH-P dans les études biologiques à grande échelle et les diagnostics cliniques.

Pour répondre à ces défis, ce mémoire propose une approche innovante qui intègre des techniques avancées d'apprentissage profond aux méthodes traditionnelles d'imagerie GSH-P. Plus précisément, nous avons développé et validé une méthode basée sur les réseaux antagonistes génératifs à super-résolution améliorée (ESRGAN) pour améliorer la résolution des images GSH-P à basse résolution d'un facteur de 16×. Cette approche réduit considérablement le temps d'imagerie—de 4.5 heures à seulement 13.5 minutes—tout en maintenant la fidélité structurelle et la précision analytique des images. En s'appuyant sur cette base, ce mémoire vise à relever ces défis en proposant un cadre innovant qui combine les forces de l'apprentissage profond et de l'imagerie optique non linéaire. Dans les sections suivantes, nous

introduisons brièvement le contexte, les objectifs et la méthodologie de ce travail, en mettant en évidence ses contributions au domaine.

Introduction et Défis

La microscopie optique biomédicale est un domaine en constante évolution, essentielle pour l'analyse des structures biologiques complexes. Parmi les différentes techniques, la génération de second harmonique (GSH) est un processus optique non linéaire qui a émergé comme un outil puissant pour l'imagerie biologique. En exploitant l'interaction de la lumière laser incidente avec des structures non centrosymétriques, la GSH permet une imagerie sans marquage avec une haute résolution spatiale. Ce phénomène découle des propriétés intrinsèques des tissus biologiques comme le collagène, qui ne possèdent pas de centre d'inversion. La microscopie GSH s'est imposée grâce à sa capacité à fournir des images à fort contraste sans photoblanchiment ni utilisation de colorants fluorescents, ce qui la rend particulièrement adaptée à l'étude des structures biologiques délicates. La technique est largement utilisée dans des applications allant de l'ingénierie tissulaire au diagnostic du cancer, en raison de sa nature non invasive et de sa capacité à révéler des détails structurels et fonctionnels au niveau moléculaire. Pour mieux contextualiser ces avancées, il convient de rappeler que la microscopie GSH tire son origine des travaux pionniers sur les phénomènes non linéaires dans les années 1960, avec la démonstration expérimentale de la génération de second harmonique par Franken et al. en 1961. Depuis lors, cette technique a évolué pour devenir un pilier de l'imagerie biomédicale, en particulier pour visualiser des composants comme le collagène sans altérer les échantillons. Cependant, malgré ces atouts, l'imagerie GSH reste confrontée à des défis techniques persistants qui limitent son déploiement à grande échelle.

En s'appuyant sur les principes de la GSH, la génération de second harmonique polarisée (GSH-P) étend les capacités de l'imagerie GSH traditionnelle en fournissant des informations supplémentaires sur l'orientation et l'anisotropie des structures fibrillaires, telles que les fibres de collagène. La GSH-P y parvient en analysant comment le signal GSH varie avec l'état de polarisation de la lumière laser incidente,

offrant des informations sur l'organisation et l'alignement des fibres au sein des tissus. Cela en fait un outil précieux pour étudier des processus tels que le développement tissulaire et les altérations pathologiques.

Malgré ses avantages, l'imagerie GSH-P conventionnelle est contrainte par des limitations pratiques, notamment des temps d'acquisition prolongés, la nécessité de composants optiques à haute résolution et le risque de photo-dommages induits par le laser sur les échantillons. Ces défis soulignent la nécessité d'innovations permettant d'améliorer la vitesse et la résolution de l'imagerie tout en préservant l'intégrité des échantillons.

Il est important de noter que ces limitations ne sont pas uniquement techniques mais aussi économiques et pratiques. Par exemple, les temps d'acquisition longs augmentent non seulement le risque de dommages aux échantillons sensibles, mais ils rendent également l'imagerie GSH-P moins viable pour des applications en temps réel ou en milieu clinique, où la rapidité est essentielle. De plus, la dépendance à des équipements haut de gamme exclut souvent les laboratoires avec des ressources limitées, freinant ainsi la démocratisation de cette technologie prometteuse.

Dans ce contexte, les réseaux antagonistes génératifs à super-résolution améliorée (ESRGAN), une méthode basée sur l'apprentissage profond, offrent une solution prometteuse pour améliorer la résolution des images tout en réduisant le temps d'acquisition et les coûts. Cette approche propose une solution transformatrice pour surmonter les compromis entre vitesse, résolution et sécurité des échantillons en imagerie biologique. En s'appuyant sur le cadre des réseaux antagonistes génératifs à super-résolution (SRGAN), ESRGAN améliore la qualité perceptuelle et la précision de reconstruction grâce à des innovations telles que les blocs denses résiduels-dans-résiduels (RRDB). Ces raffinements surmontent les limites des méthodes traditionnelles, qui privilégient souvent la précision numérique au détriment des détails visuels. En exploitant des architectures avancées de réseaux neuronaux, ESRGAN offre une approche transformatrice pour l'imagerie biomédicale, répondant aux défis clés en matière de résolution et d'efficacité.

Pour approfondir, ESRGAN se distingue par son utilisation d'un discriminateur relativiste, qui évalue non seulement si une image est réelle ou générée, mais aussi le degré de réalisme relatif entre les deux. Cela permet une reconstruction plus fidèle des textures et des structures fines, ce qui est particulièrement pertinent pour l'imagerie GSH-P où la préservation des orientations fibrillaires est cruciale. Ainsi, cette intégration d'apprentissage profond représente un pont entre l'optique traditionnelle et les technologies numériques modernes, ouvrant la voie à des innovations hybrides.

Objectifs et Innovations

L'objectif principal de ce mémoire est de surmonter les limitations des techniques d'imagerie GSH-P conventionnelles en développant une approche innovante utilisant ESRGAN pour améliorer les images GSH-P à basse résolution. Cette méthode permet une augmentation de la résolution des images tout en réduisant le temps d'acquisition de plus de 95 %, ouvrant de nouvelles possibilités pour une analyse biologique rapide et précise.

Sur le plan expérimental, des protocoles stricts de calibration ont été établis pour garantir la comparabilité entre images LR et HR. Cela inclut la correction d'intensité liée à la réponse du détecteur, l'alignement spatial entre acquisitions polarisées et la gestion des aberrations optiques via des étalonnages réguliers.

Les objectifs spécifiques de cette recherche incluent:

1. Préserver les détails structurels critiques nécessaires à l'analyse biologique : La préservation de l'intégrité structurelle est essentielle pour analyser des structures non centrosymétriques comme les fibres de collagène. L'imagerie GSH-P traditionnelle repose sur des données haute résolution pour capturer avec précision l'orientation et l'anisotropie des fibres. En utilisant ESRGAN, cette méthode garantit que les images à basse résolution améliorées conservent les détails essentiels. Les fonctionnalités avancées telles que les blocs denses résiduels-dans-résiduels (RRDB) améliorent à la fois la qualité perceptuelle et la fidélité structurelle, permettant une analyse précise à l'aide d'outils comme

CurveAlign tout en soutenant des interprétations biologiques exactes. Cet objectif s'inscrit dans une perspective plus large où la fidélité structurelle n'est pas seulement une question technique, mais un enjeu scientifique fondamental. Par exemple, dans l'étude des tissus mammaires, une perte de détails pourrait masquer des anomalies pathologiques subtiles, comme des réarrangements collagéniques associés au cancer. ESRGAN, en maintenant ces détails, facilite une analyse plus robuste et reproductible, renforçant ainsi la validité des conclusions biologiques tirées des images.

2. Améliorer la vitesse d'acquisition tout en minimisant les photo-dommages : Les temps d'imagerie prolongés dans l'imagerie GSH-P traditionnelle augmentent l'exposition au laser, entraînant des risques de photo-dommages susceptibles d'altérer l'intégrité des échantillons. En exploitant ESRGAN, le temps d'imagerie est réduit de plus de 95 % sans compromettre la qualité des images. Cette amélioration significative minimise l'exposition au laser, préservant l'intégrité chimique et morphologique des échantillons, rendant la méthode hautement adaptée aux études biologiques sensibles. Au-delà de la réduction temporelle, cette innovation a des implications éthiques et pratiques, notamment en minimisant les dommages aux échantillons rares ou précieux, tels que ceux issus de modèles animaux ou de biopsies humaines. Elle permet également d'envisager des protocoles d'imagerie in vivo plus sûrs, où l'exposition laser prolongée pourrait autrement causer des effets indésirables sur les tissus vivants.
3. Réduire les coûts en permettant l'utilisation de composants optiques moins coûteux : L'imagerie haute résolution nécessite généralement des composants optiques coûteux, tels que des objectifs et des détecteurs avancés, limitant l'accessibilité. Cette approche réduit la dépendance à ces équipements en générant des images de haute qualité à partir de données basse résolution. Cette stratégie économique abaisse les barrières à l'adoption, rendant l'imagerie GSH-P accessible aux petites institutions et évolutive pour des applications à haut débit, y compris les diagnostics cliniques et les usages industriels. Cette réduction des coûts n'est pas anecdotique ; elle pourrait démocratiser l'accès à l'imagerie avancée dans des contextes sous-financés, comme les pays en développement ou

les laboratoires universitaires modestes. De plus, en favorisant l'utilisation de composants standards, elle encourage l'innovation ouverte et la collaboration interdisciplinaire entre opticiens, biologistes et informaticiens.

Méthodologie

Cette recherche adopte une approche interdisciplinaire, combinant l'optique non linéaire et les techniques d'apprentissage profond. Les principales étapes sont les suivantes:

- Configuration d'imagerie: Le système d'imagerie se compose d'une configuration de microscopie GSH et GSH-P personnalisée, conçue pour une haute précision et flexibilité. Un laser femtoseconde est utilisé comme source lumineuse, et un objectif à haute ouverture numérique assure une focalisation efficace du faisceau laser. L'imagerie GSH-P est réalisée en faisant varier la polarisation du faisceau laser incident et en capturant les signaux GSH résultants à travers plusieurs états de polarisation. Cette configuration permet l'acquisition d'images GSH haute résolution ainsi que d'images GSH-P basse résolution avec des temps d'acquisition réduits. Cette configuration a été optimisée pour équilibrer sensibilité et robustesse, en intégrant des éléments comme un modulateur acousto-optique pour contrôler l'intensité laser et minimiser les artefacts. Des tests préliminaires ont validé sa stabilité sur des échantillons de référence, assurant une reproductibilité des données essentielles pour les étapes ultérieures d'analyse.
- Acquisition de données : Des images GSH haute résolution d'échantillons de glandes mammaires ont été capturées à l'aide d'un système d'imagerie avancé, atteignant une résolution de 1800 × 800 pixels avec une taille de pixel de 10 μm. Ce niveau de détail élevé permet une visualisation claire des caractéristiques structurelles complexes, telles que la ramification épithéliale et la formation de bourgeons terminaux, essentielles à la compréhension du développement des glandes mammaires. Chaque image GSH nécessite environ 18 minutes de temps d'imagerie, fournissant une référence robuste pour des analyses ultérieures. Pour étendre ces capacités, l'imagerie GSH polarisée (GSH-P) a été utilisée,

permettant une analyse détaillée de l'orientation et de l'anisotropie des fibres de collagène. Les images ont été enregistrées à 18 angles de polarisation, par pas de 10° de 0° à 170°. Cette méthode exploite une lame demi-onde pour contrôler la polarisation laser et capture des détails structurels critiques tout en réduisant significativement les temps d'acquisition. Ensemble, l'imagerie GSH et GSH-P fournissent un ensemble de données complet pour évaluer l'alignement du collagène et l'organisation des tissus. L'acquisition a été menée sur des échantillons provenant de modèles murins, préparés avec soin pour préserver l'intégrité tissulaire. Des protocoles de fixation et de montage ont été affinés pour éviter toute altération artificielle des structures collagéniques, garantissant que les données reflètent fidèlement les propriétés biologiques in vivo.

- Amélioration des images via ESRGAN: L'algorithme ESRGAN a été utilisé pour améliorer la résolution des images GSH-P basse résolution. La méthode garantit la fidélité structurelle et préserve la qualité perceptuelle critique, permettant aux images améliorées de répondre aux normes de leurs homologues haute résolution. Le modèle ESRGAN a été entraîné sur un ensemble de données spécifiques à l'imagerie GSH, incluant des paires d'images basse et haute résolution pour affiner ses paramètres. Des hyperparamètres comme le taux d'apprentissage et le facteur de scaling ont été ajustés itérativement pour optimiser la performance sur nos échantillons biologiques.
- Validation des résultats : Les images améliorées ont été rigoureusement évaluées par rapport aux références haute résolution à l'aide de métriques de qualité établies, notamment MS-SSIM (Indice de Similarité de Structure Multi-Échelle), PSNR (Rapport Signal sur Bruit de Pic) et NRMSE (Erreur Quadratique Moyenne Normalisée). Ces métriques confirment que les images améliorées conservent les détails structurels essentiels nécessaires à une analyse biologique précise. La validation a inclus des tests statistiques avancés, comme l'ANOVA, pour détecter toute différence significative entre les images originales et améliorées. Ces évaluations ont été complétées par des analyses qualitatives impliquant des experts en biologie pour confirmer la pertinence biologique des résultats.

Résultats et Applications

Les images GSH et GSH-P haute résolution ont fourni des informations détaillées sur la structure des échantillons de glandes mammaires, capturant des caractéristiques complexes nécessaires à l'analyse du collagène. Cependant, les images basse résolution (225 × 100 pixels) manquaient de netteté pour des études GSH-P efficaces. Pour y remédier, nous avons utilisé le modèle Ultrasharp_4X basé sur ESRGAN, qui a amélioré ces images à 3600 × 1600 pixels, réalisant une amélioration de résolution de 16×. Les métriques de contrôle qualité, notamment MS-SSIM, PSNR et NRMSE, ont validé la fidélité structurelle des images améliorées par rapport à leurs homologues haute résolution. De plus, des métriques sans référence telles que NIQE et PIQE ont confirmé des améliorations de la qualité perceptuelle, tandis qu'une analyse ANOVA n'a révélé aucune différence structurelle significative, soulignant la fiabilité des résultats améliorés. Les images améliorées se sont révélées compatibles avec CurveAlign, un outil avancé pour analyser l'alignement et l'anisotropie des fibres de collagène. L'amélioration a permis une évaluation précise de l'orientation des fibres de collagène dans l'ensemble de la glande mammaire, essentielle pour comprendre les processus de développement et les changements pathologiques. Les courbes d'intensité GSH-P normalisées ont confirmé que le processus d'amélioration préserve les propriétés biophysiques essentielles des échantillons tout en améliorant la clarté visuelle. Cette méthode a significativement réduit le temps d'imagerie de 4.5 heures à 13.5 minutes, minimisé l'exposition au laser et pris en charge l'utilisation de composants optiques moins coûteux. Ces avancées non seulement améliorent l'efficacité de l'imagerie, mais ouvrent également de nouvelles possibilités pour des études à grande échelle, des diagnostics cliniques et d'autres applications d'imagerie non linéaire.

Parmi les applications potentielles, on peut citer l'intégration de cette méthode dans des pipelines de diagnostic automatisés pour détecter précocement des pathologies comme le cancer du sein, où les modifications collagéniques sont des biomarqueurs clés. De plus, elle pourrait s'étendre à d'autres tissus fibrillaires, comme les tendons

ou les vaisseaux sanguins, élargissant son impact en médecine régénérative et en ingénierie tissulaire.

En résumé, l'approche basée sur ESRGAN équilibre efficacement la vitesse, la résolution et la précision en imagerie GSH-P, fournissant une solution robuste et évolutive pour diverses applications biomédicales.

Introduction au Contenu du Mémoire

Pour offrir une vue d'ensemble complète de la recherche, le mémoire est organisé en six chapitres, chacun abordant un aspect critique du travail:

Chapitre 1 - Introduction : Ce chapitre introduit le domaine de la microscopie optique biomédicale et son importance dans l'analyse des structures biologiques. Il expose la signification du collagène dans le développement des glandes mammaires et explique les principes de la génération de second harmonique (GSH) pour l'imagerie du collagène. De plus, il introduit la microscopie GSH polarisée et examine comment les techniques d'apprentissage profond peuvent répondre aux limitations de l'imagerie conventionnelle. Ce chapitre pose les bases théoriques en reliant l'histoire de la microscopie non linéaire à ses applications contemporaines, soulignant comment les avancées en intelligence artificielle comblent les lacunes actuelles pour une imagerie plus accessible et performante.

Chapitre 2 - Génération de Second Harmonique : Ce chapitre fournit un cadre mathématique détaillé pour la GSH, y compris la polarisation non linéaire, l'appariement de phase et les considérations d'intensité. Il explore l'application de la GSH dans les tissus de collagène et examine les principes sous-jacents à l'imagerie GSH polarisée. Il approfondit les modèles physiques, tels que la susceptibilité non linéaire et les tensors d'hyperpolarisabilité, pour expliquer pourquoi le collagène est un émetteur SHG privilégié, et discute des implications pour l'analyse polarimétrique.

Chapitre 3 - Apprentissage Machine : Ce chapitre présente un aperçu de l'apprentissage machine, en mettant l'accent sur ses applications dans l'amélioration d'images. Il discute des réseaux neuronaux artificiels, de l'apprentissage profond et

de l'architecture ESRGAN, en soulignant les avancées en matière d'imagerie à super-résolution pour les applications biologiques. En particulier, il compare ESRGAN à d'autres modèles GAN pour illustrer ses avantages en termes de qualité perceptuelle et de fidélité structurelle, avec des exemples d'applications en imagerie médicale.

Chapitre 4 - Configuration Expérimentale et Préparation des Échantillons : Ce chapitre détaille la configuration expérimentale pour l'imagerie GSH et GSH-P, y compris les sources laser, les systèmes d'imagerie et les protocoles de préparation des échantillons. Il établit la base méthodologique pour l'application d'ESRGAN à l'imagerie biologique. Des schémas détaillés et des descriptions des calibrations sont inclus pour assurer une reproductibilité, en soulignant les adaptations spécifiques aux échantillons mammaires.

Chapitre 5 - Accélération de l'Imagerie GSH-P avec l'Amélioration par Apprentissage Machine : Ce chapitre constitue la contribution principale du mémoire. Il décrit l'application d'ESRGAN pour améliorer la résolution des images GSH-P, évalue les performances du modèle à l'aide de métriques de qualité, et démontre les avantages pratiques de cette approche pour réduire le temps d'imagerie et améliorer la qualité des images. Il présente des résultats quantitatifs et qualitatifs, avec des comparaisons visuelles et des analyses statistiques, pour valider l'efficacité de l'approche dans des contextes biologiques réels.

Chapitre 6 - Conclusion : Le dernier chapitre résume les principales conclusions, met en évidence les contributions de la recherche au domaine de l'imagerie biologique et suggère des directions potentielles pour les travaux futurs, notamment le développement de modèles généralisés et l'application de ces techniques à d'autres modalités d'imagerie.

Ce synopsis sert d'introduction complète au mémoire, fournissant aux lecteurs une compréhension claire des objectifs, des méthodologies, des résultats de la recherche et de leurs implications plus larges dans le domaine de l'imagerie biologique.

TABLE OF CONTENTS

LIST OF FIGURES

LIST OF TABLES

LIST OF ABBREVIATIONS AND SYMBOLS

- SHG Second Harmonic Generation
- P-SHG Polarization-Resolved Second Harmonic Generation
- THG Third-Harmonic Generation
- CARS Coherent anti-Stokes Raman Scattering
- SRS Stimulated Raman Scattering
- MPEF Multiphoton Excitation Fluorescence
- SFG Sum-Frequency Generation
- FWM Four-Wave Mixing
- ECM Extracellular Matrix
- QPM Quasi-Phase Matching
- CNN Convolutional Neural Networks
- SR Super-Resolution
- LR Low-Resolution
- HR High-Resolution
- GAN Generative Adversarial Networks
- SRGAN Super-Resolution Generative Adversarial Networks
- EESN Edge-Enhanced Sub-Network
- UDSN Ultra-Dense Sub-Network
- ESRGAN Super-Resolution Generative Adversarial Network
- 2PEF Two-Photon Excitation Fluorescence
- O.I. Orientation Index
- AI Artificial Intelligence
- NN Neural Network
- SVM Support Vector Machines
- RF Random Forests
- ANN Artificial Neural Network
- MLP Multi-Layer Perceptron

- CNN Convolutional Neural Network
- LSTM Long Short-Term Memory
- RNN Recurrent Neural Network
- SISR Single Image Super-Resolution
- MSE Mean Squared Error
- PSNR Peak Signal-to-Noise Ratio
- SNR Signal-to-Noise Ratio
- RaGAN Relativistic average GAN
- RRDBs Residual-in-Residual Dense Blocks
- BN Batch Normalization
- RaD Relativistic average Discriminator
- ND Neutral Density
- AOM Acousto-Optic Modulator
- RF Radio Frequency
- PMT Photomultiplier tube
- I/O Input/output
- PIQE Perceptual Image Quality Evaluator
- NIQE Naturalness Image Quality Evaluator
- SSIM Structural Similarity Index
- RMS Root Mean Square
- GLCM Gray-Level Co-occurrence Matrix
- EPR Edge Preservation Ratio
- VIF Visual Information Fidelity
- FSIM Feature Similarity Index Metric
- LBP Local Binary Patterns
- ANOVA Analysis of Variance
- ROI Regions of Interest

Chapter 1: Introduction

1.1 Biomedical Optical Microscopy

Optical microscopy has been a cornerstone of biomedical research since the 17th century, when Robert Hooke first described the cellular structure of cork, introducing the concept of "cells" [1]. The contributions of Antonie von Leeuwenhoek in the late 17th century significantly advanced the field, with his meticulous observations of bacteria, spermatozoa, and muscle banding patterns using improved lenses [2,3]. These discoveries established optical microscopy as a vital tool for exploring life at microscopic level. In the early 19th century, Marie François Xavier Bichat [4] and Rudolf Carl Virchow [5] pioneered the use of microscopes in pathological anatomy, enabling the visualization of tissue structures associated with disease, such as cellular patterns in plague patients [6]. Toward the late 19th century, microscopy was limited by poor resolution, chromatic aberrations, and the absence of a theoretical framework for optical design. Ernst Abbe addressed these challenges by formulating a wave-based theory of image formation and defining the diffraction limit of resolution. Carl Zeiss applied Abbe's theory in manufacturing, standardizing high-performance microscopes. Meanwhile, Otto Schott developed new optical glasses with controlled dispersion, enabling the creation of apochromatic lenses that minimized color distortion. Their combined efforts led to the development of apochromatic lenses and marked a turning point in achieving higher resolution and image fidelity in optical microscopy [7]. These innovations laid the foundation for modern microscopy, greatly enhancing its precision and diagnostic capabilities.

The evolution of optical microscopy has been driven by a range of technological advancements, including improved optical components (such as high numerical aperture objectives and advanced lens coatings), the development of diverse light sources (e.g., lasers, LEDs, and halogen lamps) [8,9], the introduction of highly sensitive photodetectors [10,11], and significant progress in computational power, data transfer speeds, and software capabilities. These developments have expanded the scope of microscopy, enabling high-resolution imaging of complex biological systems. Recent innovations in optical imaging, such as nonlinear microscopy, super-resolution, and other advanced modalities, have significantly expanded its impact

across biology, medicine, physics, and chemistry [13]. Nonlinear optical microscopy, in particular, has gained prominence over the past three decades due to its ability to image non-centrosymmetric structures, such as collagen fibers, myosin, and microtubules without exogenous labels [14]. The theoretical foundations of two photon absorption and emission processes were established by Maria Göppert-Mayer in 1951 [15]. The low probability of nonlinear processes necessitates high-intensity light sources, and the invention of the laser [8] was a pivotal milestone. The first nonlinear optical phenomenon, second-harmonic generation (SHG), was demonstrated by Franken et al. in 1961, using a ruby laser to generate second-harmonic light from a quartz crystal [16].

The application of nonlinear optical microscopy marked a significant advancement in biomedical imaging. The first scanning nonlinear optical microscope, developed by Sheppard and Kompfner in 1978, utilized second-harmonic generation (SHG) to produce high-contrast images without exogenous labels [17]. Contemporary nonlinear optical microscopy encompasses a range of modalities, including SHG [17,18], third-harmonic generation (THG) [19], coherent anti-Stokes Raman scattering (CARS) [20], stimulated Raman scattering (SRS) [21], multiphoton excitation fluorescence (MPEF) [22], sum-frequency generation (SFG) [23], and four-wave mixing (FWM) [24]. These techniques leverage the nonlinear interaction of intense laser light with biological tissues to achieve high-resolution, depth-resolved imaging with minimal phototoxicity, making them invaluable for studying complex biological systems [14].

In recent decades, these modalities have been applied across diverse disciplines. For instance, MPEF has enabled in vivo imaging of human skin in dermatology, revealing cellular details without invasive procedures [25], and long-term imaging of synaptic plasticity in the adult cortex, advancing neurobiology [26]. In embryology, MPEF facilitates non-destructive monitoring of embryo development over 24-hour intervals, providing insights into developmental dynamics [27]. THG has been instrumental in eye biology for visualizing corneal structures [28], and in pathology for analyzing tissue morphology [29]. SHG, the focus of this thesis, has been widely used in

pathology to distinguish normal from diseased tissues by visualizing structural changes in non-centrosymmetric molecules such as collagen, myosin in muscle fibers, and microtubules in neurons. In particular, collagen remodeling serves as a key biomarker in diseases like breast cancer [32-33]. SHG has been adapted for in vivo imaging through endoscopic configurations, allowing label-free structural visualization of tissues in clinical and preclinical settings [34].

SHG is a coherent second-order nonlinear optical process, in which two photons of identical frequency interact simultaneously with a non-centrosymmetric medium to generate a single photon at exactly twice the frequency (or half the wavelength) [18]. Unlike MPEF microscopy, SHG does not involve real electronic transitions or molecular absorption; instead, it proceeds via a virtual energy state and arises from the induced nonlinear polarization in the medium. This absence of real electronic excitation substantially minimizes photobleaching and phototoxicity in biological samples, making SHG highly suitable for label-free imaging [18]. The intensity and polarization of the emitted SHG signal are determined by both the structural organization of the SHG-active material and the polarization state of the incident laser beam [18, 35].

Beyond the overall SHG intensity, the sample's response to variations in incident polarization—as well as the polarization characteristics of the emitted SHG signal—provides critical insight into the molecular alignment and orientation of SHG-active structures. These polarization-dependent properties form the basis of polarimetric SHG (P-SHG) microscopy, which involves systematically modulating the polarization state of the excitation beam and analyzing the resulting SHG signal [35-38]. While SHG intensity reflects the density and structural organization of nonlinear emitters, P-SHG allows for more nuanced characterization by resolving fibrillar orientation and degree of anisotropy.

This technique is particularly valuable in biological tissues, where non-centrosymmetric molecules such as collagen serve as strong SHG sources. Collagen, a major component of the extracellular matrix, exhibits a triple-helical molecular structure that makes it highly responsive to P-SHG analysis [18]. In this thesis, we

employ P-SHG microscopy to investigate the orientation and spatial organization of collagen fibrils in mammary gland samples. Mapping collagen alignment and remodeling can provide meaningful biomarkers of physiological and pathological changes, including tissue development and cancer progression [32].

Despite its powerful capabilities, P-SHG microscopy faces practical limitations, such as long acquisition times and the requirement for high-intensity laser excitation, which constrain its application in large-scale or in vivo imaging. These challenges motivate the development of advanced strategies to enhance acquisition speed, sensitivity, and overall imaging throughput for clinical and biomedical use.

1.2 Mammary gland development

The mammary gland is a highly specialized organ critical for the nourishment and survival of mammalian offspring, exhibiting remarkable structural and functional adaptability throughout development and into adulthood [1,40]. Its ability to undergo dynamic remodeling in response to hormonal and environmental cues underscores its significance in both normal physiology and pathological conditions [41].

Mammary gland development progresses through four primary stages: embryonic, pubertal, adult, and reproductive. During embryogenesis, a rudimentary ductal system forms, comprising a primary duct with limited branching [1]. This ductal framework is evident at birth and remains quiescent before puberty, growing at a pace matching with overall body development [40]. At puberty, estrogen and other systemic hormones stimulate ductal elongation and branching, leading to increased structural complexity. From puberty to adulthood, progesterone-driven estrous cycles promote side branching, resulting in an intricate ductal network that spans the entire fat pad [40]. During pregnancy, progesterone and prolactin, among other hormones, induce the formation of alveolar clusters on small side branches, preparing the gland for lactation [1,40].

Following the weaning period, the mammary gland undergoes a remodeling process, the involution, reverting the gland almost to its adult state. Overall, the development of the mammary gland is controlled by a complicated system of hormones from the

body and growth factors in the surrounding area [42]. It is interesting to note that a lot of the pathways and processes disrupted in breast cancer are connected to those that regulate the normal development and restructuring of the mammary gland (Fig. 1.1) [42].

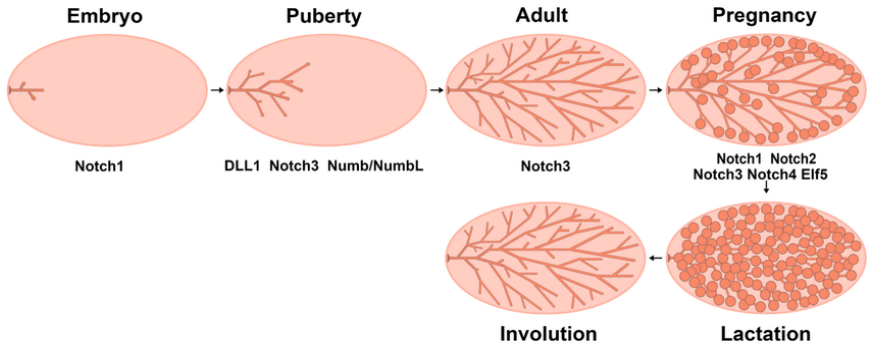

Fig. 1.1 Illustration showing the growth of the mammary gland after birth. Development of mammary glands consists of four main stages: embryonic, pubertal, adult, and reproductive. As per previous studies, Notch1 controls the differentiation of epithelial cells in embryonic development. DLL1, Notch3, and Numb/NumbL impact the mammary gland. Stretching of the duct and growth of side branches occur during puberty. Additionally, Notch3 controls the development of ductal side branches in adult stages. Throughout pregnancy, the Notch1-4 proteins play a role in controlling the formation of alveolar cells and milk production. Furthermore, Elf5 may also play a role in pregnancy by interacting with Notch signaling [42].

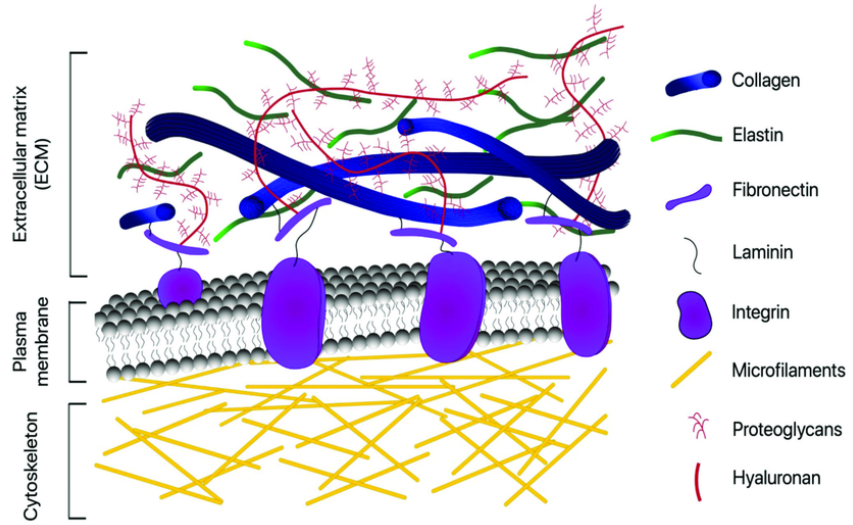

Fig. 1.2 Schematic overview of extracellular matrix and its major components. Although the ECM composition varies depending on the tissue, the matrix is mainly composed of a variety of fibrous proteins (collagen, elastin, fibronectin, and laminin) and polysaccharides that are secreted locally and assembled into an organized meshwork in close association with the surface of the cell that produced them [43].

During its entire development, from prepuberty to involution, the mammary glands undergo various changes involving different types of cells composing the epithelium and the stroma, including components of the extracellular matrix (ECM) shown in Fig. 1.2 [44]. Reorganization of the ECM is a key process in both ductal elongation at puberty and alveologenesis during the pregnancy and lactation cycle [45]. The ECM is the cellular scaffolding in tissues and organs without cells. The ECM also significantly impacts tissue development, specialization, and balance [41]. ECM is primarily made up of water, proteins, and polysaccharides. However, the structure and arrangement of ECM in every tissue is distinct because of varying biochemical and biophysical interactions among cellular components and the microenvironment during organ development [46,47]. The ECM mainly comprises two categories of large molecules: glycoproteins like fibronectin, proteoglycans and laminin, and fibrous proteins such as collagen and elastin.

1.3 Collagen Structure

Collagen is the body's most plentiful structural protein and makes up a large part of the extracellular matrix in multicellular organisms, particularly in connective tissues like tendons, ligaments and skin [48]. Its structure is organized in a hierarchical manner from the molecular to the fibrillar level, which contributes to its mechanical strength and functional versatility. The unique characteristics of collagen (with over twenty genetically distinct varieties) in any tissue or organ are influenced by its primary structure, post-translational modifications, and interactions with other connective tissue components [48]. The various collagens are classified into fibrillar or nonfibrillar types, depending on their supramolecular organizational patterns [49]. In general, collagen can be classified as fibrillar collagen, FACITs, MACITs, and MULTIPEXINs, which consist of various triple-helix domains and interruptions [50]. There are total of 28 various forms of collagen made up of at minimum 46 separate polypeptide chains, each serving a diverse array of functions, including offering tensile strength, controlling cell adhesion, aiding chemotaxis and movement, and guiding tissue growth [47].

In this study, we concentrate on fibrillar collagens, mainly type I collagen, which is the most common type in the body and a primary target in SHG microscopy. This preference arises because SHG microscopy is particularly effective to image type I and type II collagens due to their strong nonlinear optical properties, which enhance signal generation. The collagens that form fibers generally comprise a triple-helical macromolecule with brief, nonhelical extensions at both ends [51].

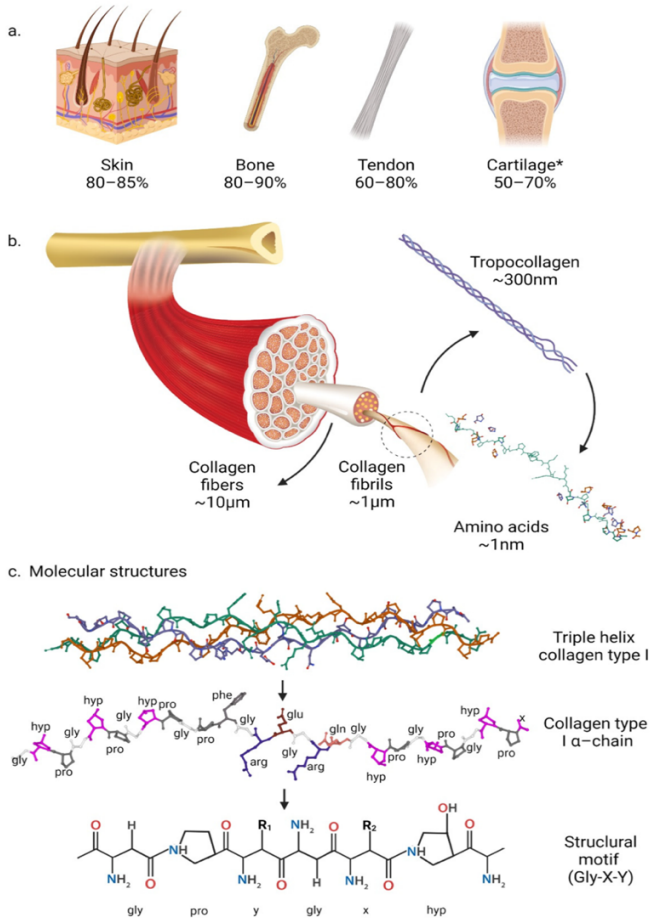

Fig. 1.3 (a) Sources of collagen type I and estimated amounts in various tissues. The cartilage percentage reflects the total collagen in dry weight, with type II collagen being the dominant type. (b) Structure of collagen fibers, fibrils, triple helices formed by alpha chains as tropocollagen, and specific amino acid residues. (c) The molecular arrangement of triple-helix and single-chain collagen type I, featuring gly-x-y repeats, where x-y usually denotes proline and hydroxyproline, respectively [54].

Collagen serves as the primary structural component of the ECM. A triple helix protein makes up 30% of the total protein in the human body [50]. Collagen can be

found in different tissues and organs [52] like tendons, cartilage, bones, skin, ligaments, corneas, and basement membranes [53]. The way collagen is structured and organized in three dimensions within the tissue plays a key role in determining the functional properties of collagen-based tissues. Examining the alterations in collagen assembly's microstructure is crucial in comprehending developmental, disease, and regeneration mechanisms. As a result, it is essential to assess the structural characteristics of collagen at various levels of hierarchy, spanning from individual fibrils to groups of fibrils within the tissue.

Therefore, it is unsurprising that collagen has been extensively researched using various chemical and physical techniques in recent decades to explore its chemical and mechanical characteristics and its role in different tissues and settings [55]. The collagen structure consists of three α polypeptide chains twisted around each other in a right-handed triple-helix shape, resembling a rope (Fig. 1.3) Every polypeptide chain is made up of a series of amino acids with a pattern where every third amino acid is glycine (Gly), creating a repetitive X-Y-Gly sequence known as a triple-helical motif. X and Y are commonly occupied by Proline (Pro) and Hydroxyproline (Hyp). However, they can be any amino acid, resulting in Pro-Hyp-Gly being the most prevalent motif in collagen [50]. This primary unit measures 290 nm in length and has a diameter of 1.5 nm [56].

Collagen fibers possess a hierarchical organization within the tissue. In the initial phase, the triple helical configuration self-organizes into medium-sized fibril sections, referred to as microfibrils. Additionally, microfibrils cluster to form fibrils. The diameter of collagen fibrils ranges from 10 to 500 nm, varying by tissue type [57,61]. Collagen fibrils exhibit a regular pattern along the longitudinal axis known as the D–periodic gap/overlap spacing or "D–spacing".

This consistent pattern of gap and overlap areas is visible in TEM images of collagen fibrils, with the reported value of D = 67 nm in the literature [50]. The D–spacing results from a displacement between adjacent molecules arranged in a staggered formation. In the end, fibrils combine to form macroscopic fibers and networks seen in tissues, bones, and basement membranes through cross-linking molecules. In

tendons, fibrils measure 100–300 nm in diameter that combine to form fibers and bundles, with a diameter ranging from 100–200 μm [56]. In the cornea, the fibrils are slender and exhibit a distinct higher-order arrangement. The self-assembly mechanisms associated with collagen fibrillogenesis modify collagen characteristics in various tissues, affecting the cornea's transparency, the tendon's high tensile strength, the bone's resistance, and the skin's elasticity. Moreover, these changes are crucial in ECM pathology.

1.4 Second Harmonic Generation in Collagen

SHG microscopy is the favored technique for visualizing collagen in tissues due to its excellent spatial resolution, minimal phototoxicity and photobleaching, selectivity of the focal plane, and simple sample preparation [62]. This label-free imaging method allows for observing alterations in fibrillar collagen within the mammary gland, a feature unrivaled by other imaging techniques [62].

In Fig. 1.4, an illustration comparing one-photon and two-photon fluorescence, as well as SHG, is presented alongside their energy diagrams. In fluorescent microscopy, a fluorophore is initially excited to a higher energy state after absorbing a high-energy photon. As a result, a portion of the absorbed energy is dissipated via vibrational relaxation, and the leftover energy is emitted as a lower-energy photon when the fluorophore reverts to its ground state [58]. In two-photon fluorescence, two photons of lower energy are absorbed simultaneously to excite the fluorophore with the help of an intermediate "virtual" state. Just like in the one-photon scenario, the shift from the ground state to the excited state also includes molecular absorption and the subsequent release of a fluorescence photon [58]. Fluorescence is incoherent with the excitation photons, as it is a spontaneous emission process. Furthermore, the intrinsic energy absorption associated with both one-photon and two-photon fluorescence has the potential to induce photodamage in the fluorophore as well as in surrounding biological tissues.

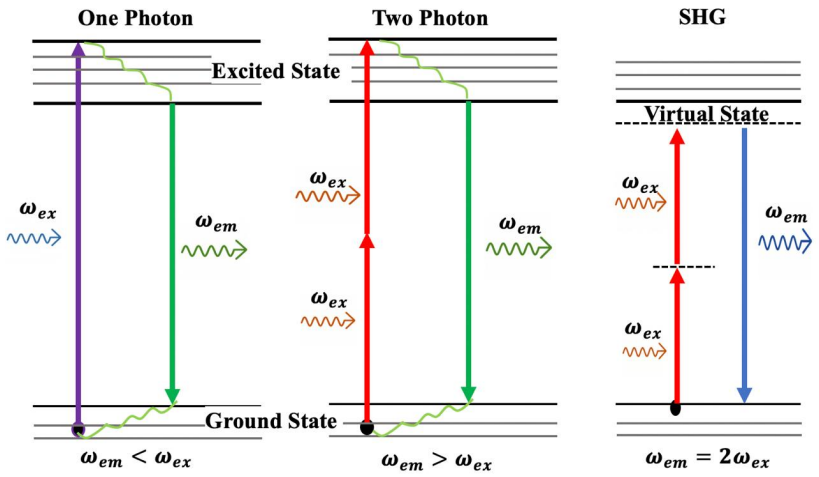

Fig. 1.4 Illustration of one-photon, two-photon and SHG energy diagram. The thick black lines represent the ground state. Thin gray lines represent electronic states, and dashed lines represent virtual states. Different colored solid arrows indicate the incident and generated photons.

Upon photon absorption, a fluorophore undergoes a transition to an excited state; the subsequent relaxation mechanisms may produce heat or reactive species, which can result in chemical alterations or degradation [59]. In comparison, SHG functions through a process that does not require medium absorption. Two lower-energy photons interact within a nonlinear medium, generating a single photon with twice the energy (or half the wavelength) of the original photons [58]. In this process, molecular absorption does not occur, significantly minimizing photo-damage. The correlation between the incoming photons and the emitted SHG photon is preserved [58].

1.4.1 Origin of SHG from collagen

As mentioned, SHG can only be generated from samples with non-centrosymmetric structures, such as collagen [60]. At the macroscopic level, the SHG signal is represented by the second-order susceptibility tensor, $\chi^{(2)}$. In contrast, on a molecular scale, the strength of SHG is characterized by the first hyperpolarizability tensor, β. The hyperpolarizability relies on the composition and arrangement of the molecules that make up collagen. Numerous studies have examined the connection between the first hyperpolarizability, the molecular makeup and arrangement of collagen, and the

second–order susceptibility of collagen [56,63-69]. Nonetheless, investigating this relationship experimentally is not straightforward. Consequently, computational and modeling methods can address this issue [68].

A collagen triple–helix can be considered as a set of simple dipoles placed along the protein backbone (Fig. 1.5) [65]. Presuming that all the collagen triple–helix components are properly aligned along a shared axis, the SHG signal for fibrillar collagen can be understood as the coherent summation of the hyperpolarizabilities of the individual building blocks [71,72].

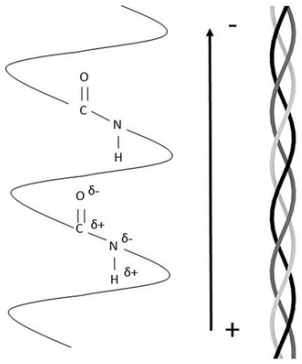

Fig. 1.5 Representation of SHG signal generation from collagen-I. The peptide bonds of the collagen chains create a permanent dipole moment along the triple helix that allows second harmonic generation [65].

While this interpretation is broadly accepted in the discipline, another study has challenged it [70]. In research conducted by Tuer et al., a modelling approach (Segment Additivity Model) is utilized to assess the impact of different amino acids, and the findings were illustrated using a creative technique known as Unit Sphere Representation [70]. The findings indicated that several non-zero elements exist in the hyper-polarizability tensors of the amino acids, contradicting earlier reported results [70]. Nonetheless, due to the arrangement of the amino acids within the collagen triple-helix, the coherent summation of hyperpolarizabilities yields SHG dipoles adjacent to the Cα–N–C backbone, as suggested by Plotnikov et al [71]. This outcome may clarify why the SHG signal reaches its peak when the polarization of the incoming laser beam is nearly aligned with the axis of the collagen fibrils. The collagen molecules subsequently organize into fibrils exhibiting identical polarity [73].

1.4.2 Current models interpret SHG based on collagen's structure

Various models have been suggested to account for the notable backward-generated SHG from collagen tissues. Williams et al. assign the SHG to a thin surface layer measuring ten of nanometers in thickness, which decreases the interaction length within the collagen, making it comparable to the coherence length for backward SHG [67]. To support this, Fig. 1.6 shows the hollow tube-like structure of the resolvable fibrils [67]. Nonetheless, this model only tackles the SHG from one fibril. Collagen fibers consist of numerous fibrils, and as SHG is a coherence phenomenon, the SHG generated by one fibril can interact with the SHG produced by neighboring fibrils. This interaction can significantly affect the overall SHG signal within the focal volume of the imaging system, influencing the observed results [65]. Therefore, this model is unable to account for the collective contribution of all fibrils in the fiber to the total SHG signal.

An additional explanation arises from the observation that type I collagen fibrils typically create highly structured quasi-crystalline formations. It has been acknowledged that the biological realm has developed a wide array of systems that function to control light transmission and vibrant appearance. The direction of emission relies on both the fibrils' size and the fibril structure's density and organization [74]. LaComb et al. connect the various phase mismatches Δk in both forward and backward directions to the diameter and packing of fibrils within the quasi-phase matching (QPM) theory framework [75,76]. QPM attains effective phase matching by adjusting the relative phase at consistent intervals, utilizing a periodic structure incorporated in the nonlinear medium [77]. Nonetheless, the authors only offer a heuristic approach, leaving the relationship between the Δk and the actual fibril structure unexplained.

As a result, SHG microscopy has been crucial in collagen research; nonetheless, using only SHG intensity for orientation studies may cause interference [79] and complicating the imaging of fibril orientation [63]. To overcome these limitations, polarization-resolved SHG microscopy (P-SHG) has been developed, providing the advantages of SHG microscopy and polarimetry [51,63].

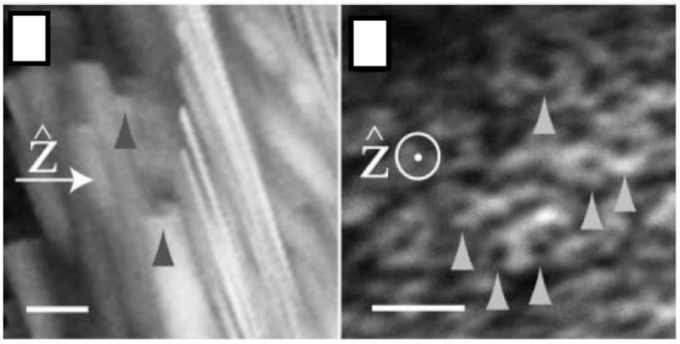

Fig. 1.6 High resolution images revealing the hollow tube appearance of thick fibrils which can be resolved by SHG microscopy. The hollow cores are marked by arrows [67].

1.5 Polarization resolved SHG microscopy

Polarization resolved second harmonic generation (PSHG) microscopy is an advanced imaging technique that extends the capabilities of SHG microscopy by integrating polarimetry to derive detailed alignment insights from non-centrosymmetric biological entities [18]. This method enhances the ability to probe the molecular alignment of samples by systematically varying the polarization state of the incident laser beam and measuring the resulting SHG signal's intensity and polarization characteristics [36]. This approach facilitates the mapping of fibril alignment and the evaluation of structural anisotropy, which are essential for understanding tissue development and pathology [38].

The unique structure of collagen, which lacks inversion symmetry at the wavelength scale of light, enables it to generate SHG light in collagen. However, due to the slight birefringence of collagen fibers, biological tissues do not perfectly satisfy the strict phase-matching condition required for SHG. Instead, they exhibit quasi-phase matching. In this scenario, the SHG light generated by collagen operates under a non-phase-matching condition, where multiple scattering events within a coherent length in the tissue cause the SHG light from individual collagen molecules to constructively interfere. This constructive interference leads to coherent enhancement of the SHG signal. Fig. 1.7 provides a summary of the relationship between collagen orientation and laser polarization regarding SHG light. When the incident light is normal to the cross-section of the collagen fiber, the SHG light from collagen is not obtained at any

polarization angle. In an incidence configuration like this, the cylindrical symmetry along the longitudinal axis in collagen molecules makes any laser polarization centrosymmetric with respect to the collagen orientation, resulting the non-generation of SHG light. However, other configurations induce SHG light because the relation between the collagen orientation and the laser polarization is non-centrosymmetric [79].

In particular, when the laser polarization is parallel to the collagen orientation, a strong SHG light is observed. The polarization direction of the resultant SHG light is consistent with that of the incident laser light. On the other hand, SHG light is significantly weaker when the laser polarization is perpendicular to the collagen orientation [79]. These polarization dependences reflect the nonzero elements of the second-order susceptibility tensor ($\chi^{(2)}$) in collagen molecules, the analytical model of which is discussed elsewhere [18]. To confirm these relations, Yasui et al. measured the collagen SHG light on the human Achilles tendon, which possesses a well-defined uniaxial orientation in the collagen fiber [79].

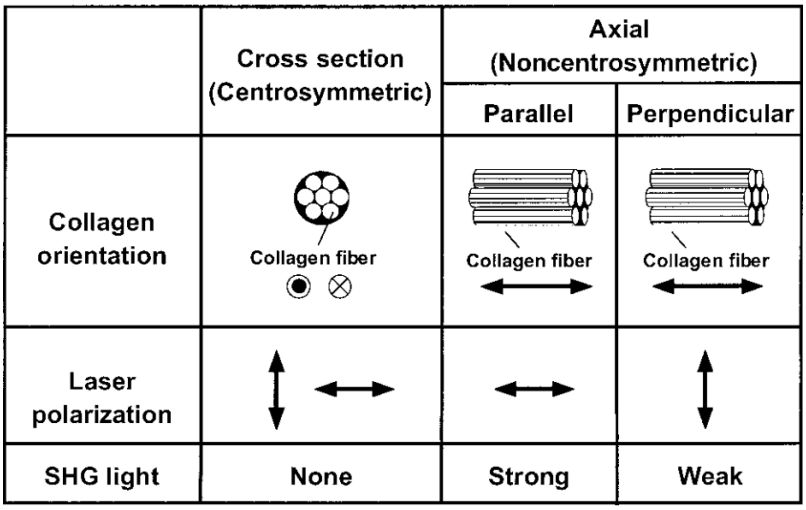

Fig. 1.7 Relationship between collagen orientation and laser polarization with respect to the generation of SHG light [79].

The resulting SHG was as anticipated strongest when the incident light polarization direction was parallel to the longitudinal fiber direction and significantly weaker when the collagen orientation and laser polarization were perpendicular to one another (The ratio of SHG intensity between the two configurations was 50:1) [79].

This outcome suggests that SHG polarimetry serves as an orientation-specific probe, applicable not only to collagen but also to other non-centrosymmetric biological structures [79]. Polarization-resolved SHG (P-SHG) microscopy offers additional information and means of contrast beyond intensity-based SHG. As a conclusion, P-SHG allows for the reconstruction of alignment maps by providing information on several physiologically and pathologically relevant aspects that would not be possible to obtain from intensity measurements alone such as the arrangement and structure of the constitutive biomolecules [80]. The holistic perspective this method provides on collagen alignment throughout the entire gland is crucial for a thorough understanding of the developmental processes at work. However, it may have the drawback of omitting some finer variations and fibers. Our study took advantage of deep learnings capabilities to get around the cost and time constraints of whole-sample P-SHG imaging.

1.6 Deep Learning for Image Enhancement

Recent advancements in deep learning have significantly impacted biomedical image analysis, enabling accurate segmentation, classification, and enhancement of complex imaging data [81-85]. One particularly promising application is enhancing the resolution — the process of reconstructing high-resolution (HR) images from low-resolution (LR) inputs — which is critical in biomedical contexts where hardware limitations or acquisition speed impose constraints on imaging quality [88]. Deep learning methods have shown remarkable success across a wide range of tasks, including image classification [86], speech and text recognition [87], by effectively capturing complex and nonlinear patterns in high-dimensional data. Building on these capabilities, deep learning has been increasingly applied to biomedical domains, demonstrating outstanding performance in tasks such as brain image segmentation [88], mitosis detection [89], disease diagnosis, and cellular structure analysis [90].

In microscopy, deep learning has been successfully applied to image analysis tasks including tissue segmentation, cell detection, and image classification [91]. Artificial Neural Networks (ANNs) are a class of machine learning models inspired by the structure and function of biological neurons. They consist of interconnected layers of

simple processing units (neurons) that learn to approximate complex mappings between input and output data. Among the various ANN architectures, Convolutional Neural Networks (CNNs) have emerged as particularly powerful for image-related tasks [81,92]. CNNs are designed to automatically extract hierarchical features from input images through convolutional layers, pooling operations, and nonlinear activations. This ability to learn spatial hierarchies of features makes CNNs especially well-suited for biomedical imaging applications, where complex patterns and fine structural details must be efficiently recognized [93-95]. CNNs excel at target classification because they learn hierarchical data representations [96] - progressively abstracted features of input images - through supervised training, which uses labelled datasets to guide the learning process. However neural networks for representation learning can also use unsupervised learning, which uses unlabeled data to identify patterns or structures [97,98]. For example, autoencoder, a type of unsupervised neural network, has shown promise in microscopy image analysis by extracting meaningful features on their own, eliminating the need for costly human annotations [99]. This feature makes unsupervised learning particularly useful in applications such as super-resolution techniques, which require high-quality outputs from low-resolution data [97,98].

In recent years super-resolution (SR) methods have been developed for both natural and medical images, enhancing the effectiveness of medical imaging as an essential tool for diagnosing and treating patients [100]. Isotropic medical images in high-resolution (HR) with comprehensive textural and structural information are necessary for quantitative analysis and precise diagnosis [100]. The quality of medical images is influenced by several factors, making it challenging to obtain high-quality images in clinical practice. These factors include physiological movements, the time required for image acquisition, hardware limitations, and the radiation dose that patients can safely tolerate [100]. Along with being expensive upgrading image-capturing equipment has limited potential to improve image quality [100]. Deep learning offers a viable approach to have HR images.

Among deep learning-based super-resolution methods, Generative Adversarial Networks (GAN) based methods have demonstrated significant improvement

[101,102]. The GAN architecture makes use of the perceptual or content-based loss function, i.e., the VGG19 loss to get around the drawbacks of CNN-based SR techniques. The application of a GAN which quantifies the perceptual feature difference between the generated image and the high-resolution ground-truth image is one essential component [62]. The discriminators' ability to identify real data as real and generated data as fake is gauged by its loss function. The ability of the generator to trick the discriminator into acknowledging the generated data as authentic data is gauged by the generator loss function. The generator seeks to increase the likelihood that the discriminator will make a mistake [62].

The first SR technique based on GANs, known as Super-Resolution GAN (SRGAN), was introduced in [103]. The ResNet34 architecture serves as the SRGANs generator extracting features from LR images. Upsampling was achieved through the use of a sub-pixel convolution layer, which works by rearranging the feature map's pixels into a higher resolution output, effectively increasing the image's size while preserving details. Wang et al. made additional modifications to this approach [104]. They employed multi-residual networks, i.e., residual-in-residual dense blocks. After each convolutional layer, they also removed the batch normalization layer. When the batch normalization layer was removed, the conventional SRGAN architecture performed better. Compute complexity is increased by using nested or multiple residual blocks. Jiang and co-workers proposed an edge-enhanced GAN for satellite image super-resolution [105]. The architecture is composed of two main networks: The Edge-Enhanced Sub-Network (EESN) and the Ultra-Dense Sub-Network (UDSN). The EESN focuses on improving the sharpness of the edges in the image while also removing any artifacts that may arise during the feature extraction process in the UDSN. On the other hand, the UDSN is responsible for extracting important features from the image and producing high-resolution output, with an emphasis on preserving sharp edges for better detail [105]. Garnavi et al. used a GAN in combination with a saliency map to generate HR retinal fundus images [106]. A saliency map emphasizes the most important regions of an image, usually those that are most relevant for analysis, such as blood vessels or lesions in retinal fundus images [106]. By minimizing the GAN cost function, the saliency map effect effectively enhances the

performance of GAN-based HR image generation [107]. Fig. 1.8 shows an example of how LR can change to HR image by using GAN's network [107].

Another advanced form of GAN is Enhanced Super-Resolution Generative Adversarial Network (ESRGAN), which is a deep learning-based approach for image super-resolution. The architecture of ESRGAN expands on the concept of GANs but it adjusts enhance the super-resolution procedure [104].

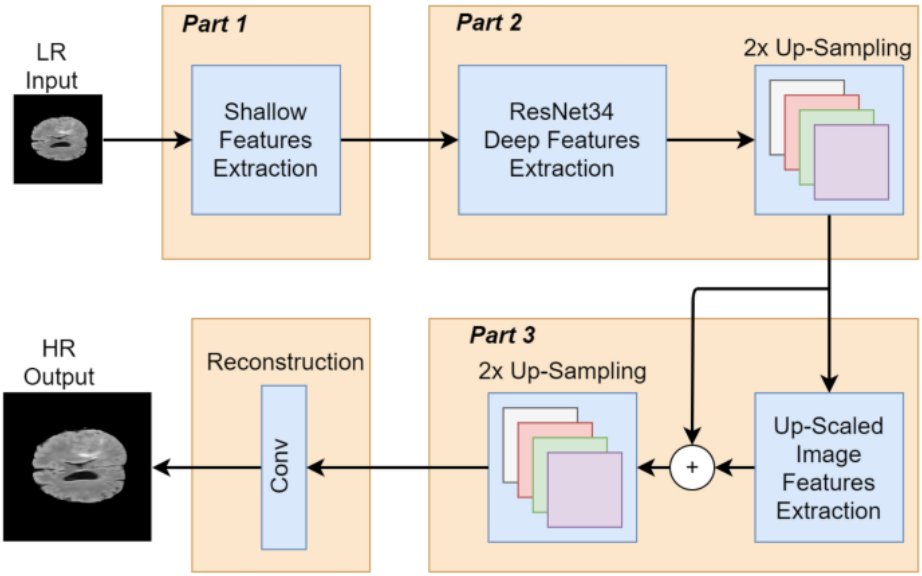

Fig. 1.8 An overall block diagram to show the two rounds of the feature extraction and 2x GAN's upscaling [107].

Rather than depending only on pixel-wise similarity ESRGAN can concentrate on capturing high-level features of an image like edges textures and structures thanks to the perceptual loss function [104]. Images produced by ESRGAN seem realistic and visually plausible to human viewers. A combination of perceptual loss (to preserve visual quality) and adversarial loss (to guarantee realism) is used to train the ESRGAN model. Iteratively updating the discriminator and generator networks during the training process enhances the quality of the produced image over time [104]. In Chapter 3, we will explore machine learning methods in more detail, with a particular focus on ESRGAN, which was employed in our work to upscale the low-quality P-SHG images of samples.

In this work, we address key limitations in polarization-resolved SHG imaging of biological tissues, particularly the trade-off between spatial resolution, acquisition speed, and the risk of photodamage from prolonged laser exposure. High-resolution P-SHG imaging of large samples, such as whole mammary gland tissues, often requires long scanning times (up to several hours) and high numerical aperture optics, making it impractical for routine or high-throughput applications. To overcome these constraints, we explore the application of ESRGAN, specifically the Ultrasharp_4X variant, for reconstructing high-resolution images from low-resolution acquisitions. ESRGAN was selected due to its perceptual-driven architecture, which excels at preserving fine structural features such as collagen fiber orientation and anisotropy—critical for SHG analysis—while outperforming conventional interpolation or CNN-based methods. By integrating this deep learning approach with nonlinear optical microscopy, our goal is to significantly reduce imaging time and hardware demands, while maintaining the fidelity of structural information required for accurate biological interpretation.

Chapter 2: Second Harmonic Generation

2.1 Introduction

While traditional linear optical microscopes are highly effective tools, they struggle with scattering and cannot provide optical sectioning in dense or intricate samples [107]. However, advanced imaging techniques, such as harmonic generation imaging, have seen remarkable advancements in the past few decades. Imaging based on harmonic generation, which usually involves second- and third-order mechanisms, is a significant aspect of nonlinear optics with a rich historical background [108]. Like many other nonlinear optical contrast mechanisms, the theoretical origins of two photon absorption can be linked to Dr. Maria Göppert-Mayer's theoretical research in the 1930s [109]. The proof of SHG experimentally demands high peak power of excitation light, which was made achievable with the development of the laser in the 1960s [110]. Franken and his colleagues were the first to show SHG in ruby laser interacting with quartz, which marked the beginning of practical applications in nonlinear optics [110]. After this time, the importance of harmonic generation in laser physics and solid-state material characterization has been widely acknowledged, leading to numerous exciting developments in both areas [111]. Nevertheless, the commencement of using harmonic generation for examining biological specimens occurred at a later time. Therefore, SHG microscopy has emerged as a crucial technique for optical imaging, with numerous applications in both materials and biomedical research [111]. Some of the pioneering works included the generation of second harmonic from amino acid crystals in 1965 [112]. In 1971, Fine and colleagues showed second-harmonic generation from biological samples, such as collagen, an important natural structure giving a robust second-harmonic signal [113]. During the late 1970s, Sheppard and his colleagues discovered that the nonlinear aspect of harmonic generation causes optical interaction to be localized in three dimensions at the focal point of a high numerical aperture objective [114]. This discovery led to the development of a scanning second-harmonic generation microscope with 3D imaging capabilities [115]. After 15 years, Freund and colleagues showed one of the earliest biological second-harmonic imaging experiments in 1986, which involved mapping collagen structures in tendons.

However, this study had low spatial resolution and did not consider depth sectioning [60].

In 1990, Denk and coworkers were the first to show two-photon fluorescence imaging (2PEF) in biological samples, displaying high-quality 3D images of embryos [116]. This landmark study sparked interest among biomedical researchers in nonlinear optical microscopy [116]. The growing interest led to the creation of reliable and user-friendly commercial nonlinear microscopes capable of imaging through fluorescence and harmonic generation methods. These researchers have shown the correlations between SHG signals and tissue conditions, identifying various molecular structures that produce strong SHG, and developing contrast agents sensitive to biochemical environments and resistant to photobleaching [108]. These successful pioneering works have firmly established SHG imaging as a crucial tool for microscopists.

On the other hand, advancements in the development of reliable and robust ultrafast mode-locked laser technologies have been essential for enhancing non-linear optical microscopy methods, particularly in the field of biomedical imaging [108]. These ultrafast laser sources have been used to create complete microscopes that are now commonly found in research labs. SHG microscopy requires the structures of interest to be non-centrosymmetric [117], making it very sensitive to filamentous proteins in biological samples [118]. Otherwise, samples need to be dyed with suitable SHG dyes [119]. While this requirement limits SHG application to a small number of structures, it is a positive aspect since the signals are highly specific and offer sharp contrast images [111]. Moreover, SHG microscopy offers multiple benefits compared to fluorescence imaging because it relies on an intrinsic contrast instead of a dye or fluorophore. Finally, SHG is different from fluorescence as it does not suffer from photobleaching and happens instantly (no limit on laser repetition rate) [120].

In the context of microscopy, 2PEF and SHG share numerous technical similarities, enabling effortless and effective integration in a single instrument. Since the obtained imaging depth depends on the excitation wavelength [111,120], lasers within the NIR-I range (700–1000 nm) (700–1000 nm) [119] are typically chosen to minimize absorption by biomaterials like water and hemoglobin [121]. Utilizing longer

wavelengths like NIR-2 (1000-1300 nm) can reduce scattering and increase tissue penetration depth [107,120], but with the trade-off of decreased spatial resolution [111]. Despite the higher penetration depth provided by longer wavelengths, it has been shown that for imaging collagenous tissues, longer wavelengths lead to a weaker SHG signal due to a reduction in hyperpolarizability tensor [122]. In addition, utilizing longer wavelength lasers (1230 nm) like Cr:forsterite lasers allows for the concurrent conduction of SHG and third harmonic generation (THG) microscopy in the visible spectrum, preventing UV absorption by biological samples [123].

To favor the efficient generation of the SHG, the typical laser pulse duration is about 100 fs at a repetition rate of a few tens of MHz [120]. Objectives with a high numerical aperture (NA >1) are employed to precisely focus the light onto the sample and localize laser pulse energy spatially [124]. To efficiently gather the light in the forward direction from thin samples, a high numerical aperture condenser is included [118]. Both modalities (2PEF and SHG) exhibit a quadratic dependence of the generated signal on the input laser intensity, resulting in an inherent three-dimensional spatial resolution because the signal is confined within the focal volume [125,126].

Although SHG and 2PEF techniques are similar in some ways, they rely on fundamentally different mechanisms. In SHG, the conversion of frequency is accomplished using virtual states without any overall energy transfer to the system (Fig. 1.4). This is different from 2PEF which includes transferring population from the electronic ground state to excited electronic states [111]. The diverse sources result in significantly different, and frequently complementary characteristics that account for the increasing appeal of SHG microscopy [111].

2.2 Mathematical Framework of SHG

2.2.1 Nonlinear polarization

Nonlinear optics focuses on how optical fields interact in a medium with nonlinearity. When the medium is not treated linearly and the properties like refractive index and

absorption coefficient do not depend on intensity, the nonlinear interaction between fields and material is not common at low optical intensities [117]. Nonlinear optical processes are observed only after the advent of lasers, which could provide the required high intensities to excite the nonlinear effects [117].

In the case of linear optics, the induced polarization $\boldsymbol{P}(t)$ depends linearly on the electric field strength $\boldsymbol{E}(t)$ in a manner that can be described by [117]:

$$\boldsymbol{P}(t) = \varepsilon_0 \chi^{(1)} \boldsymbol{E}(t) \qquad 2\text{-}1$$

where, $\chi^{(1)}$ is known as the linear susceptibility and ε_0 is the permittivity of free space.

However, under high intensities the medium properties become intensity dependent, and as a result the medium acts as a mediator for interaction between optical fields [117]. The optical response can be described by generalizing Eq. 2-1 by expressing the polarization $\boldsymbol{P}(t)$ as a power series in the field strength $\boldsymbol{E}(t)$ as:

$$\begin{aligned} \boldsymbol{P}(t) &= \varepsilon_0 \left[\chi^{(1)} \boldsymbol{E}^1(t) + \chi^{(2)} \boldsymbol{E}^2(t) + \chi^{(3)} \boldsymbol{E}^3(t) + \cdots \right] \\ &= \boldsymbol{P}^{(1)}(t) + \boldsymbol{P}^{(2)}(t) + \boldsymbol{P}^{(3)}(t) + \cdots \end{aligned} \qquad 2\text{-}2$$

The quantities $\chi^{(2)}$ and $\chi^{(3)}$ are known as the second and third order nonlinear optical susceptibilities, respectively. Here, $\boldsymbol{P}(t)$ and $\boldsymbol{E}(t)$ are vectors, while $\chi^{(1)}$ is a second rank tensor, $\chi^{(2)}$ is a third-rank tensor, and so forth. The term $\chi^{(1)} \boldsymbol{E}^1(t)$ corresponds to the linear response, $\boldsymbol{P}^{(2)}(t) = \varepsilon_0 \chi^{(2)} \boldsymbol{E}^2(t)$ defines second-order non-linear interactions, such as SHG, sum and difference frequency generation [117], two-photon absorption [126], and the third term, $\boldsymbol{P}^{(3)}(t) = \varepsilon_0 \chi^{(3)} \boldsymbol{E}^3(t)$ describes third-order non-linear effects, like third harmonic generation [127], Kerr effect [128], self-phase modulation [129], cross-phase modulation [130], and stimulated Raman scattering [131]. In writing the equation, we can simplify the term by treating both $P(t)$ and $E(t)$ as scalar quantities. Equations 2-1 and 2-2 are commonly used methods to describe varying levels of nonlinearity in previous works such as Ref. [117]. When writing equations, we have also assumed that the polarization at time t depends only on the instantaneous value of the electric field strength.

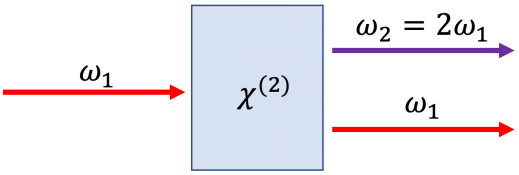

Fig. 2.1 Second-harmonic generation [117].

For SHG, which is illustrated schematically in Fig. 1.4 and its geometry is shown in Fig. 2.1. A laser beam with an electric field strength $E(t) = Ee^{-i\omega t} + c.c.$ is directed towards a material with a non-zero second-order susceptibility $\chi^{(2)}$. Nonlinear polarization arising in a material is determined by equation 2-2. As for $P^{(2)}(t) = \varepsilon_0 \chi^{(2)} E^2(t)$, it can also be written explicitly as:

$$P^{(2)}(t) = 2\varepsilon_0 \chi^{(2)} EE^* + \left(\varepsilon_0 \chi^{(2)} E^2 e^{-2i\omega t} + c.c\right) \qquad 2\text{-}3$$

We see that the second-order polarization consists of a contribution at zero frequency (the first term) and a contribution at frequency 2ω (the second term) which can lead to the generation of radiation at the second-harmonic frequency.

Therefore, SHG can be efficiently described through an anharmonic oscillator model in which a non-linear restoring force is generated by the molecular potential [117]. At the molecular level, for collagen and tubulin, SHG originates from the hyperpolarizability of peptide bonds, usually considered as single SHG emitters [132]. Indeed, an electric field oscillating at a high frequency and reaching an harmonophore will repeatedly pull the electrons back and forth, leading to the induction of a molecular dipole [126,133]. More precisely, the second order polarization can be expressed as:

$$P_i^{2\omega} = \chi_{ijk}^{(2\omega)} E_j^{\omega} E_k^{\omega} \qquad 2\text{-}4$$

where, the subscripts denote Cartesian components and superscripts denote the relevant frequencies. The second order susceptibility $\chi_{ijk}^{2\omega}$ describes the relation between all the components of the polarization and the electric-field vectors for sum and difference frequency generation. $\chi_{ijk}^{2\omega}$ is a third−rank tensor and contains 27 $(3 \times 3 \times 3)$ elements, in which these elements sum up to zero for materials with

inversion symmetry. Physically, this means that the ability to generate second harmonics is limited to molecules which are not centrosymmetric. To produce appreciable SHG, a material must be non-centrosymmetric over macroscopic distances [117].

2.2.2 SHG in bulk material

By assuming the medium is lossless at both the fundamental frequency ω_1 and ω_2 at the second-harmonic frequency $\omega_2 = 2\omega_1$, the nonlinear susceptibility must follow the condition of full permutation symmetry [117]. In this case, each component of the second order polarisation can be expressed at the bulk level as:

$$P_i^{(2)}(2\omega) = \sum_{j,k} \chi_{ijk}^{(2)}(\omega,\omega) E_j(\omega) E_k(\omega) \qquad 2\text{-}5$$

or at the molecular level:

$$\mu_i^{(2)}(2\omega) = \sum_{j,k} \beta_{ijk}^{(2)}(\omega,\omega) E_j(\omega) E_k(\omega) \qquad 2\text{-}6$$

Here the dipole moment $\mu_i^{(2)}$ and the hyperpolarizability $\beta_{ijk}^{(2)}$ represent the molecular counterparts of $P_i^{(2)}$ and $\chi_{ijk}^{(2)}$, which are related to polarization and susceptibility, respectively [117]. In the general case of three-wave mixing, the matrix representing the susceptibility tensor $\chi_{ijk}^{(2)}(\omega_1,\omega_2)$ consists of 27 separate elements. Second harmonic generation occurs when two input waves have the same frequency with $\omega_1 = \omega_2 = \omega$, which is a degenerate case of three-wave mixing. As a result:

$$\begin{aligned} P_i^{(2)}(2\omega) &= \sum_{j,k} \chi_{ijk}^{(2)}(\omega,\omega) E_j(\omega_1) E_k(\omega_2) \\ &= \sum_{k,j} \chi_{ikj}^{(2)}(\omega,\omega) E_k(\omega_1) E_j(\omega_2) \end{aligned} \qquad 2\text{-}7$$

Hence, the susceptibility tensor exhibits the subsequent symmetry [117]:

$$\chi_{ijk}^{(2)}(\omega,\omega) = \chi_{ikj}^{(2)}(\omega,\omega) \qquad 2\text{-}8$$

Having these symmetries reduces the tensor's number of independent elements to 18. Therefore, the second order induced polarization P_i can be expressed in terms of the tensor $\chi_{ijk}^{(2)}$ components and the electric field E_i, as follows [117]:

$$\begin{pmatrix} P_x^{(2)} \\ P_y^{(2)} \\ P_z^{(2)} \end{pmatrix} = \varepsilon_0 \begin{pmatrix} \chi_{xxx}^{(2)} & \chi_{xyy}^{(2)} & \chi_{xzz}^{(2)} & \chi_{xyz}^{(2)} & \chi_{xxz}^{(2)} & \chi_{xxy}^{(2)} \\ \chi_{yxx}^{(2)} & \chi_{yyy}^{(2)} & \chi_{yzz}^{(2)} & \chi_{yyz}^{(2)} & \chi_{yxz}^{(2)} & \chi_{yxy}^{(2)} \\ \chi_{zxx}^{(2)} & \chi_{zyy}^{(2)} & \chi_{zzz}^{(2)} & \chi_{zyz}^{(2)} & \chi_{zxz}^{(2)} & \chi_{zxy}^{(2)} \end{pmatrix} \begin{pmatrix} E_x^2 \\ E_y^2 \\ E_z^2 \\ 2E_yE_z \\ 2E_xE_z \\ 2E_xE_y \end{pmatrix} \quad \text{2-9}$$

The use of a contracted notation is made possible by the symmetry of the second harmonic generation:

$$d_{is}(\omega) \equiv \frac{1}{2}\chi_{ikj}^{(2)}(\omega, \omega) \quad \text{2-10}$$

Where, the spatial index, i, ranges from 1 to 3, and s ranges from 1 to 6. The relationship between s, j, and k can be described as:

s	1	2	3	4	5	6
j	x	y	z	y	z	x
k	x	y	z	z	x	y

If the electric field's frequency ω is significantly different from any natural frequencies, such as off-resonance, then the susceptibility can be considered constant regardless of frequency [117].

$$\chi_{ijk}^{(2)}(\omega, \omega) \cong \chi_{ikj}^{(2)} \quad \text{2-11}$$

As a consequence, all indices of the tensor can be rearranged without restriction, a condition that is known as Kleinman symmetry [117,135]:

$$\chi_{ijk}^{(2)} = \chi_{ikj}^{(2)} = \chi_{jki}^{(2)} = \chi_{jik}^{(2)} = \chi_{kji}^{(2)} = \chi_{kij}^{(2)} \quad \text{2-12}$$

The Kleinmann symmetry decreases the number of independent elements of the susceptibility tensor to 10 [117,135].

The system's symmetry can often lead to a decrease in the large quantity of tensor elements. Neumann's principle dictates that physical properties must not change in sign or amplitude under system symmetry operations [136]. We investigate how inversion symmetry affects polarization and second-harmonic generation later on. If a centro symmetric material is examined (i.e. has a center of inversion), the $\chi^{(2)}$ nonlinear susceptibility must totally disappear. The nonlinear polarization is determined as Eq. 2-4. Under inversion, the electric field and polarization transform as E changes to -E and P changes to $-P$. The equation 2-4 is transformed as follows:

$$-P_i^{(2)} = \chi_{ijk}^{(2)}[-E]^2 = \chi_{ijk}^{(2)}E^2 \;\Rightarrow\; P_i^{(2)} = -\chi_{ijk}^{(2)}E^2 \qquad 2\text{-}13$$

because we assume that the medium possesses inversion symmetry. By comparing the two equations 2-4 and 2-13 we obtain:

$$P_i^{(2)} = \chi_{ijk}^{(2)}E^2 = -\chi_{ijk}^{(2)}E^2 \qquad 2\text{-}14$$

Equation 2-14 is only valid for $\chi_{ijk}^{(2)} = 0$ and is highly significant in second-harmonic generation. A second-harmonic response is only present in systems that are non-centrosymmetric, and no SHG signal can be produced in a medium that exhibits spatial inversion symmetry [137]. This condition is easily fulfilled at the molecular level by constructing a donor–π–acceptor (D π A) system by linking an electron-donor to an electron-acceptor through a π-conjugated system [138]. In addition, non-centroymmetry in the molecular dipole arrangement is necessary to produce a second-harmonic signal [111]. Examples of these kinds of symmetries can be seen in biological membranes, where only one side is dyed, as well as in all helical molecules like protein and nucleic acid helices [111]. Additional constraints on the nonlinear susceptibility tensor's structure can be caused by different symmetry properties of the non-linear optical medium, with each system symmetry leading to a decrease in the tensor's non-vanishing components [117].

In this condition, we can write:

$$\begin{pmatrix} P_x^{(2)}(2\omega) \\ P_y^{(2)}(2\omega) \\ P_z^{(2)}(2\omega) \end{pmatrix} = 2\varepsilon_0 \begin{pmatrix} d_{11} & d_{12} & d_{13} & d_{14} & d_{15} & d_{16} \\ d_{21} & d_{22} & d_{23} & d_{24} & d_{25} & d_{26} \\ d_{31} & d_{32} & d_{33} & d_{34} & d_{35} & d_{36} \end{pmatrix} \begin{pmatrix} E_x^2(2\omega) \\ E_y^2(2\omega) \\ E_z^2(2\omega) \\ 2E_y(\omega)E_z(\omega) \\ 2E_x(\omega)E_z(\omega) \\ 2E_x(\omega)E_y(\omega) \end{pmatrix} \quad \text{2-15}$$

It is possible to represent the nonlinear polarization responsible for second-harmonic generation with a scalar relationship for a fixed geometry (fixed propagation and polarization directions) [117].

$$P(2\omega) = 2\varepsilon_0 d_{eff} E(\omega)^2 \quad \text{2-16}$$

where, d_{eff} is obtained by first determining **P** explicitly through use of Eq. 2-15 and is the effective value of the second order susceptibility. According to the geometry of the nonlinear medium, d_{eff} can be calculated. In the later section, we will calculate it for a collagen fibril.

2.2.3 SHG Intensity

To determine the intensity of the produced second harmonic, the total electric field in the nonlinear medium is considered as [117]:

$$\boldsymbol{E}(z,t) = \boldsymbol{E_1}(z,t) + \boldsymbol{E}_2(z,t) \quad \text{2-17}$$

where each component is expressed in terms of a complex amplitude $E_j(z)$ and slowly varying amplitude $A_j(z)$ according to

$$\boldsymbol{E_j}(z,t) = E_j(z)e^{-i\omega_j t} + c.c. \quad and \quad E_j(z) = A_j(z)e^{ik_j z} \quad \text{2-18}$$

where the propagation constant and refractive index are given by

$$k_j = \frac{n_j \omega_j}{c} \quad and \quad n_j = \sqrt{\epsilon^{(1)}(\omega_j)} \quad \text{2-19}$$

It is assumed that each frequency component of the electric field follows the driven wave equation [117]:

$$\nabla^2 \boldsymbol{E_j} - \frac{\epsilon^{(1)}(\omega_j)}{c^2}\frac{\partial^2 \boldsymbol{E_j}}{\partial t^2} = \frac{1}{\varepsilon_0 c^2}\frac{\partial^2}{\partial t^2}\boldsymbol{P}_j^{NL} \qquad 2\text{-}20$$

This wave equation must hold for each frequency component of the field and in particular for the SHG component at frequency $\omega_2 = 2\omega_1$. In the absence of a nonlinear source term, the solution to this equation for a plane wave at frequency ω_2 propagating in the z direction is [117]:

$$\boldsymbol{E_2}(z,t) = A_2(z)e^{i(k_2 z - \omega_2 t)} + c.c. \qquad 2\text{-}21$$

By considering the nonlinear source term appearing in Eq.2-20 as

$$\boldsymbol{P_2}(z,t) = P_2 e^{-i\omega_2 t} + c.c. \qquad 2\text{-}22$$

where according to Eq. 2-16, we have:

$$P_2 = 2\varepsilon_0 d_{eff} E_1^2 = 2\varepsilon_0 d_{eff} A_1^2 e^{2ik_1 z} \qquad 2\text{-}23$$

By neglecting the complex conjugate part and slowly varying amplitude approximation, the wave equation can be written as [117]:

$$\frac{dA_2}{dz} = \frac{2id_{eff}\omega_2^2}{k_2 c^2} A_1^2 e^{i\Delta k z} \qquad 2\text{-}24$$

where, $\Delta k = 2k_1 - k_2$ which is called the wavevector (or momentum) mismatch. Equation 2-24 is referred to as a coupled-amplitude equation, as it demonstrates the change in the amplitude of the ω_2 wave due to its interaction with the ω_1 wave. By considering the spatial changes in ω_1 waves, we can come up with similar equations for ω_1:

$$\frac{dA_1}{dz} = \frac{2i\omega_1^2 d_{eff}}{k_1 c^2} A_2 A_1^* e^{-i\Delta k z} \qquad 2\text{-}25$$

Now, by integrating over the length L of the nonlinear medium, for slowly varying amplitude of the SHG beam we have:

$$A_2(L) = \frac{id_{eff}\omega_2^2 L}{2k_2} A_1^2 \left(\frac{e^{-i\Delta k L} - 1}{\Delta k}\right) \qquad 2\text{-}26$$

Therefore, considering an incident laser beam with fixed polarization and propagation direction, and assuming the slowly varying envelop approximation, the SHG intensity can be expressed as follows:

$$I_{SHG} = 2n_2\varepsilon_0 c|A_2|^2 = \frac{4d_{eff}^2\omega_2^2L^2}{n_1^2n_2\varepsilon_0c^2}I_1^2\text{sinc}^2\left(\frac{\Delta kL}{2}\right) \qquad 2\text{-}27$$

Where, I_1 is the intensity of the incident laser beam and the effect of wavevector mismatch is included entirely in the factor $\text{sinc}^2\left(\frac{\Delta kL}{2}\right)$.

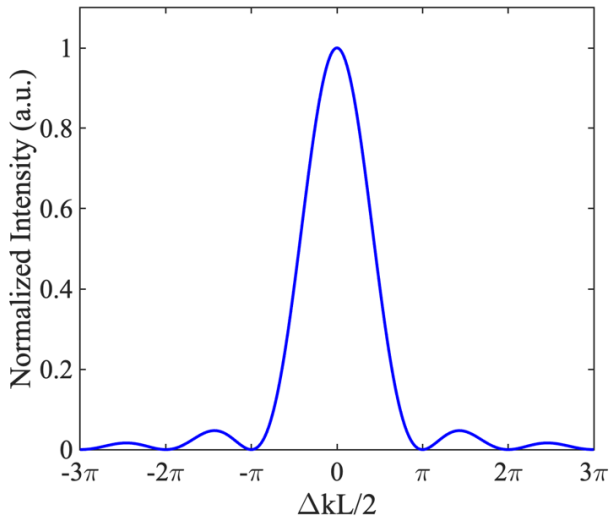

Fig. 2.2 Effects of phase mismatch on the efficiency of SHG intensity.

Fig. 2.2 illustrates the change in SHG intensity based on the phase mismatch ($\Delta kL/2$). It is evident that the highest intensity occurs when $\Delta kL/2$ is zero. This condition is referred to as phase matching condition [117]. It is clear that the effectiveness of the SHG process reduces as ΔkL increases, while some oscillations take place. The reason for this behavior is that if L is greater than about $1/\Delta k$, the output wave may become out of phase with its driving polarization, allowing power to flow from the SHG frequency, ω_2, into the incident beam frequency, ω_1 (refer to Eq. 2-24) [117].

2.2.4 Phase matching

In the Eq. 2-27, the SHG intensity varies proportionally to the square of the $\mathrm{sinc}\left(\frac{\Delta kL}{2}\right)$ function with the phase mismatch factor of ΔkL. The velocity of the fundamental and second harmonic waves varies due to the refractive index at their respective wavelengths [117]. Typically, the SHG has a higher refractive index than the fundamental due to normal dispersion, causing the two waves to travel at varying phase velocities. As a consequence, the transfer in power flow between waves is influenced by the phase difference of the waves, resulting in a change in the direction of power transfer due to the continuous phase shift caused by varying phase velocities. So, SHG is effectively generated until $\Delta kL/2 = \pi$. The coherence length is defined as the distance where the relative phase between the two waves shifts by π, corresponding to half of the growth and decay cycle of the second harmonic [111]. The SHG coherence length, L_c, is defined as:

$$L_c = \frac{2}{|\Delta k|} = \frac{2}{|2k_1 - k_2|} = \frac{2}{\left|2\frac{n_1\omega_1}{c} - \frac{n_2\omega_2}{c}\right|} \qquad 2\text{-}28$$

Since, in SHG process $\omega_2 = 2\omega_1$, so:

$$L_c = \frac{2}{2\frac{\omega_1}{c}|n_1 - n_2|} = \frac{\lambda}{2\pi\left|n_{fundamental} - n_{SHG}\right|} \qquad 2\text{-}29$$

Smaller Δk translates to longer L_c. Longer L_c allows a longer interaction length L, which in turn allows for higher SHG intensity [69]. With a non-perfect phase matching condition, where $\Delta k \neq 0$, the SHG intensity is much weaker (Fig. 2.2).

In a single direction, the phase mismatch for forward SHG is equal to $\Delta k = 2k_1 - k_2 = |2k_1| - |k_2|$ with $k_1$and k_2 both traveling in the same direction. In backward SHG, the phase mismatch is $\Delta k = 2k_1 - k_2 = |2k_1| + |k_2|$ as k_1 and k_2 travel in opposite directions. The mismatch in phase is more pronounced in the backward direction, leading to a significant decrease in coherence length within the medium.

Achieving the phase-matching condition $\Delta k = 0$ can be challenging, as materials without losses between frequencies ω_1 to ω_2 exhibit normal dispersion where the

refractive index increases with frequency. As a result, the condition for perfect phase matching with collinear beams is [117]:

$$\Delta \boldsymbol{k} = 2\boldsymbol{k}_1 - \boldsymbol{k}_2 = 2\frac{n_1\omega_1}{c} - \frac{n_2\omega_2}{c} = \frac{2\omega_1}{c}\left(n(\omega_1) - n(\omega_2)\right) = 0 \qquad 2\text{-}30$$

So, for perfect phase matching, the condition of $n(\omega_1) = n(\omega_2)$ should be satisfied. But, for normal dispersion, $n(\omega_2)$ must be greater than $n(\omega_1)$, due to $\omega_2 > \omega_1$, which demonstrates that Eq. 2-30 cannot be satisfied.

It is theoretically feasible to satisfy the phase-matching requirement by utilizing anomalous dispersion, which is the reduction in refractive index as frequency increases near an absorption peak [117]. The most used method to achieve phase matching is by utilizing the birefringence exhibited by numerous crystals. Birefringence refers to the way in which the refractive index changes based on the polarization direction of the optical radiation [117]. In particular, crystals belonging to the cubic crystal system are optically isotropic and show no birefringence, thus are not phase-matchable [117].

Another method for enabling efficient generation of the harmonic wave is quasi-phase matching which involves repeated inversion of the relative phase between the fundamental and second harmonic wave [77]. One way to invert the phase is to change the sign of the nonlinear coefficient via inverting the optical axis of a ferroelectric material periodically [117]. For example, in one dimension, when the second order susceptibility $\chi^{(2)}$ is spatially modulated at a frequency Q, the d_{eff} becomes [117],

$$d_{eff}(z) = de^{-iQz} \qquad 2\text{-}31$$

The phase matching condition in this case becomes,

$$\Delta k = 2k_1 - k_2 - Q \qquad 2\text{-}32$$

Perfect phase matching is obtained when $Q = 2k_1 - k_2$. In terms of physics, the periodic structure produces grating effects and provides a virtual momentum to assist the phase matching [117]. This leads to constructive interference in a certain

direction. By the mechanism of quasi-phase matching, efficient SHG can be generated over a relatively long distance or when the phase mismatch is relatively large [117].

2.3 SHG in collagen tissue

In order to analyze the SHG signal in collagen tissue quantitatively, we consider the non-centrosymmetric arrangement of proteins in the fiber. It is important to note that molecules with SHG emission capability have a high hyperpolarizability β, which is greatly influenced by their symmetry. The coherent nature of SHG implies that the signal results from interferences of individual contributions of harmonophores [124,133]. At macroscopic scale, SHG is described by the non-linear susceptibility $\chi^{(2)}$, which results from the coherent summation of the individual hyperpolarizabilities of all harmonophores within a volume. The relation between the molecular and macro-molecular non-linear response is given by [124,133]:

$$\chi^{(2)} = N_s \langle \beta \rangle \qquad 2\text{-}33$$

where N_s is the density of molecule S and $\langle \beta \rangle$ is the orientational average of the first hyperpolarizability [117]. For SHG to take place in this size range, the material must have a $\chi^{(2)} \neq 0$, which is only possible with a non-centrosymmetric arrangement of large molecules [124,126]. Therefore, in order to conduct SHG microscopy on biological samples, the tissue needs to have a non-centrosymmetric structure at both the molecular ($\beta \neq 0$) and macro-molecular ($\langle \beta \rangle \neq 0$) levels, along with a high concentration of harmonophores [124,133]. It is interesting that SHG signal's limited origin can be used to improve contrast, as it is unique to only a small number of biological structures, with collagen being a key illustration [124,133]. SHG can serve as a distinctive tool to investigate the multiscale distribution of molecules in the sample.

To determine the susceptibility tensor $\chi^{(2)}$ of a collagen fibril, we should examine the spatial arrangement of molecules in three dimensions. Using collagen as a model, this concept can be applied to other materials by considering their specific symmetry. A collagen fibril presents a cylindrical symmetry. We will make two assumptions:

first that the Kleinman symmetry is applicable and secondly that the chiral components of the tensor can be neglected since we do not take the out-of-focus orientation into account [139].

We select a coordinates system (Fig. 2.3) with the laser propagation direction on the z axis and x is the collagen fiber axis. The driving electric field is linearly polarized in the x-y plane and does not have any component in the optical axis direction. Therefore, it can be expressed by $\boldsymbol{E} = E_x\hat{x} + E_y\hat{y}$.

For collagen fiber, cylindrical symmetry is commonly assumed, with the symmetry axis being the fiber axis (x axis in Fig. 2.3).

The susceptibility tensor components in a system with a mirror plane change by multiplying their coordinates. Therefore, if the index of a tensor component changes following a symmetry operation, it will result in a zero value. Indeed, an easier method to confirm that $\chi^{(2)}_{ijk} = -\chi^{(2)}_{ijk}$ is true after the symmetry operation is to confirm that $ijk = -ijk$ is true [140].

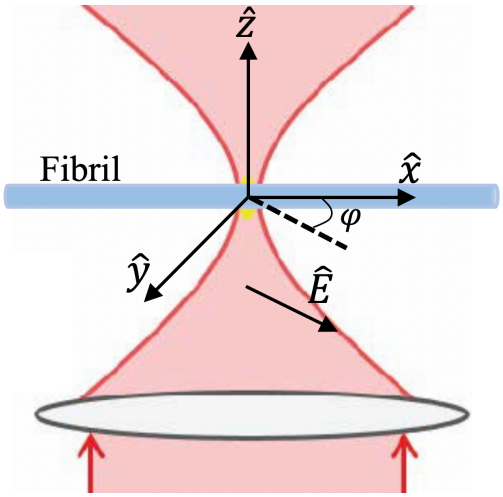

Fig. 2.3 Schematic of the coordinate system to computing the susceptibility tensor $\chi^{(2)}$ in a symmetry of scatterers like collagen fibril. The SHG scatterers are organized with a cylindrical distribution with $\hat{x}$ as the axis of symmetry. The incident beam is directed along the $\hat{z}$ axis. φ represents the angle between the electric field $\hat{E}$ and the x-axis of the filament [67].

Collagen fiber exhibits cylindrical symmetry with mirror planes in the x-z and x-y planes. When reflected on these planes, the coordinates change as follows: x→-x ,

y→y , z→ z for the y-z mirror plane; while for the x-y mirror plane, x→x , y→y , z→-z [117,133]. As a result, the mirror planes cause certain components of the second-order susceptibility tensor to disappear, while certain non-zero elements of $\chi_{ijk}^{(2)}$ become equal.

The fiber symmetry remains unchanged when rotated around the x-axis, resulting in transformations y → z and z → -y for mirror planes x-z and x-y. Therefore, we obtain:

$$\chi_{zzx}^{(2)} = \chi_{(-y)(-y)x}^{(2)} = \chi_{yyx}^{(2)} \qquad 2\text{-}34$$

Additionally, as mentioned previously, $\chi_{ijk}^{(2)}$ can be rearranged among all indices according to the Kleinman symmetry assumption like Eq. 2-12 and we obtain [140]:

$$\chi_{xyy}^{(2)} = \chi_{yyx}^{(2)} = \chi_{xzz}^{(2)} = \chi_{zxx}^{(2)} \qquad 2\text{-}35$$

Therefore, in a cylindrically symmetric distribution such as in the collagen fiber with x-z and x-y mirror planes, $\chi_{xxx}^{(2)}$ and $\chi_{xyy}^{(2)}$are the only two independent components of the susceptibility tensor. The other components of the tensor vanish instead, due to symmetries of the material [140]. The second order tensor reduces to:

$$\chi^{(2)} = \begin{pmatrix} \chi_{xxx}^{(2)} & \chi_{xyy}^{(2)} & \chi_{xyy}^{(2)} & 0 & 0 & 0 \\ 0 & 0 & 0 & 0 & 0 & \chi_{xyy}^{(2)} \\ 0 & 0 & 0 & 0 & \chi_{xyy}^{(2)} & 0 \end{pmatrix} \qquad 2\text{-}36$$

So,

$$\begin{pmatrix} P_x^{(2)} \\ P_y^{(2)} \\ P_z^{(2)} \end{pmatrix} = \begin{pmatrix} \chi_{xxx}^{(2)} & \chi_{xyy}^{(2)} & \chi_{xyy}^{(2)} & 0 & 0 & 0 \\ 0 & 0 & 0 & 0 & 0 & \chi_{xyy}^{(2)} \\ 0 & 0 & 0 & 0 & \chi_{xyy}^{(2)} & 0 \end{pmatrix} \begin{pmatrix} E_x^2 \\ E_y^2 \\ E_z^2 \\ 2E_yE_z \\ 2E_xE_z \\ 2E_xE_y \end{pmatrix} \qquad 2\text{-}37$$

Therefore, we obtain:

$$P_x^{(2)} = \chi_{xxx}^{(2)} E_x^2 + \chi_{xyy}^{(2)} E_y^2 + \chi_{xyy}^{(2)} E_z^2 \qquad 2\text{-}38$$

$$P_y^{(2)} = 2\chi_{xyy}^{(2)} E_x E_y$$
$$P_z^{(2)} = 2\chi_{xyy}^{(2)} E_x E_z$$

Thus, considering that the input laser is linearly polarized and propagates along the z-axis, the SHG intensity for every fibril is as follows [111]:

$$I_{SHG}(\varphi, \theta) = A + Bcos(2\varphi - 2\theta) + Ccos(4\varphi - 4\theta) \quad 2\text{-}39$$

Where, φ is the angle of polarization relative to the x-axis (Fig. 2.3), while θ is the azimuthal angle of the fibril with the x-axis. Coefficients A, B, and C vary based on the concentration and arrangement of the harmonophores [141]. Hence, changing the incident polarization significantly influences the SHG intensity. This allows for the examination of how harmonophores are organized at the macro-molecular level within the focal volume [142]. On the other hand, utilizing circularly polarized excitation light guarantees uniform response from all molecules, regardless of their in-plane orientation [126].

Since SHG is a coherent process, the phase is essential in the creation of the signal, from the molecular level to the macro-molecular level. This can be easily emphasized by looking at the case of SHG from bulk media. As explained in previous section, when a laser beam with fixed polarization and direction of propagation is considered and the slowly varying envelope approximation is assumed, the SHG intensity can be represented by Eq. 2-27 and it is proportional to [117]:

$$I_{SHG} \propto L^2 I_{in}^2 \mathrm{sinc}^2\left(\frac{L}{L_c}\right) \quad 2\text{-}40$$

Where, I_{in} is the incident laser beam's intensity, L is the length where SHG happens in the medium, and $L_c = 2/\Delta k$ is the coherence length. Therefore, if the phase-matching condition ($\Delta k = 0$) is fulfilled, the SHG intensity increases proportionally to both the input laser intensity squared and the length squared. However, if $\Delta k \neq 0$, the SHG intensity peaks after interaction length of $\pi L_c/2$. If the interaction length L increases within the material, the SHG intensity fluctuates between zero and the maximum value across a spatial period of $2\pi L_c$ [117].

In biological samples, it is uncommon for the perfect phase-matching condition to be met, resulting in the SHG signal being directional. Nevertheless, ΔkL is almost zero in the forward direction because the interaction length is much smaller than L_c (a few microns), thanks to the tight focusing. In contrast, when moving in the opposite direction, Δk is significantly greater and the coherence length is much smaller (a few tens of nanometers). This is the reason why "pure" backward SHG is consistently weak.

2.4 Polarization-resolved SHG (P-SHG)

Polarization-resolved second harmonic generation (P-SHG) combines the advantages of SHG microscopy (high specificity and contrast) with polarimetry (sensitivity to molecular alignment) [111]. P-SHG is typically applied to collagen, offering a more detailed and accurate representation of the complex hierarchical organization of fibrils within the imaging plane. One of the earliest demonstrations of P-SHG was performed on rat-tail tendon, a collagen-rich tissue, as documented in reference [143]. They used a model for polarization dependent SHG on rat-tail tendon fascia to determine collagen fibril orientation and study the second order nonlinear susceptibility tensor. Obtaining various linear polarization scans in both the axial and transverse planes, they found that the SHG signal was significantly influenced by the polarization of the laser light source, enabling them to determine the alignment of collagen fibers [143].

We understand that the SHG scatterers (harmonophores) within the tissue do not all align perfectly, and each has its own unique direction. When we examine a collagen fibril, we establish a set of axes (x′, y′, z′) for the individual fibril with respect to the overall axes (x, y, z) of the laboratory reference system, as depicted in Fig. 2.4. This figure shows the schematic of coordinate system for a collagen fibril for a P-SHG system.

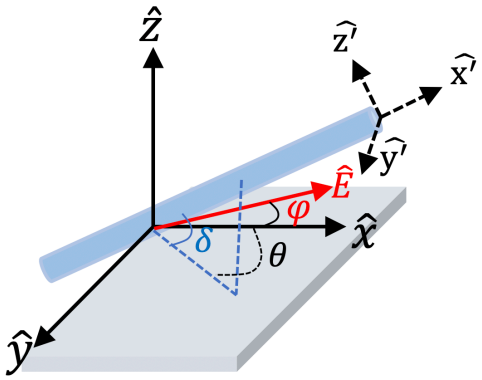

Fig. 2.4 Schematic of the coordinates of the laboratory system ($\hat{x}, \hat{y}, \hat{z}$) and of the molecular system ($\hat{x}', \hat{y}', \hat{z}'$) of each harmonofore. φ is the polarization angle and θ is the azimuthal angle of the fibril with respect to the x-axis respectively, and δ is the out-of-plane tilt angle of the fibril [139].

As long as the fibrils and the incident electric field lie both within the focal plane, an incident electric field $\boldsymbol{E}_{in}$ at angle φ to the laboratory axis (x, y, z) induces the following SHG polarization in the fibril frame (according to Eq. 2-38):

$$P_x^{(2)}(2\omega) \propto \rho \cos^2(\varphi - \theta) + \sin^2(\varphi - \theta)$$
$$P_y^{(2)}(2\omega) \propto 2\cos(\varphi - \theta)\sin(\varphi - \theta) \qquad 2\text{-}41$$

Where, ρ is the anisotropy parameter and θ is the fibrils orientation angle, with respect to the axis x in the laboratory frame (Fig. 2.4). In addition, to characterize the collagen fibrils' orientation, various parameters can be measured such as the average in-plane azimuthal angle θ, in every pixel, and the anisotropy parameter [144]:

$$\rho = \sqrt{\frac{I_{\parallel}}{I_{\perp}}} = \rho_0 \cos^2(\delta) + 3\sin^2(\delta) \qquad 2\text{-}42$$

where $I_{\parallel}$ and $I_{\perp}$ are the SHG intensity when the incident polarization is parallel and orthogonal to the fibril, δ is the out-of-plane tilt angle of the fibril (Fig. 2.4) and $\rho_0 = \rho(\delta = 0) = \chi_{xxx}^{(2)}/\chi_{xyy}^{(2)}$ is the anisotropy parameter for no tilt [145].

Alternatively, one can use the measure of the "anisotropy parameter" r for no tilt in the out-of-plane direction [124].

$$r = \frac{I_{\parallel} - I_{\perp}}{I_{\parallel} + 2I_{\perp}} \qquad 2\text{-}43$$

Here, an isotropic orientation is represented by $r = 0$, while the fully aligned case corresponds to $r = 1$. In practice, the anisotropy parameter is approximately 0.7 in highly aligned collagen tissue like tendon [124].

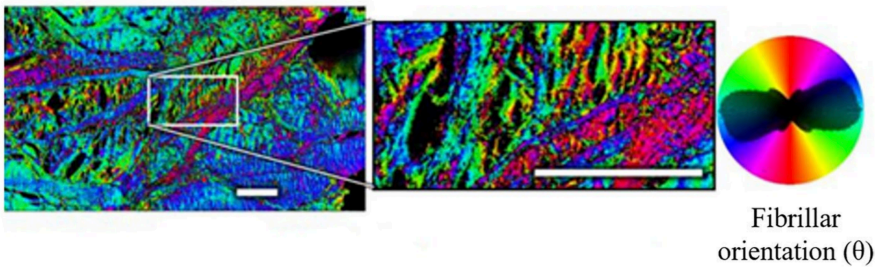

Fig. 2.5 Collagen fibril orientation in adult horse specimens measured by P-SHG. In this study, the maturation of meniscal collagen was studied in young and adult horses using P-SHG [144].

Additional measurements like the entropy of orientation [146] and the orientation index (O.I.) [80] can be obtained from P-SHG, and some research has identified the variance of contrast per pixel as relevant metrics for P-SHG [111]. One efficient method for extracting information from P-SHG involves utilizing Fourier transform analysis. In this scenario, just the input polarization is adjusted by half- and quarter-wave plates [143,147] (Fig. 2.5). Later on, the important data can be extracted from the P-SHG images by conducting an analysis that relies on the Fourier transform of the intensity measured in relation to the input polarization angle.

Chapter 3: Machine Learning

Machine learning is a prominent area in today's computing realm, with extensive research dedicated to enhancing it. Learning is an innate human activity that has been integrated into machines as a crucial element. Machine learning deals with how to develop models that enhance themselves through practice and learning. It is a quickly expanding technical field today, situated at the crossroads of computer science and statistics, and essential in artificial intelligence and data science [148]. Advancements in machine learning have been fueled by the creation of new learning algorithms and theory, as well as the continuous growth in online data and affordable computation [148]. Data-heavy machine-learning techniques are being increasingly utilized in various fields such as science, technology, and business, contributing to a rise in data-driven decision-making in numerous aspects of life including healthcare, manufacturing, education, financial modeling, law enforcement, and advertising [148,149].

3.1 Introduction

Artificial Intelligence (AI) is about creating machines that have the same level of intelligence as the human brain. In the field of Computer Science, AI refers to the examination of "intelligent agents": any technological tool that senses its surroundings and makes decisions to increase its chances of successfully accomplishing its objectives [151]. Colloquially, the term "artificial intelligence" is used to describe a machine's ability to carry out tasks typically linked to human cognitive abilities, like "learning" and "problem solving". Machines rely on learning as a crucial factor. Hence, machine learning is a branch of artificial intelligence. Computer Scientists have been working on machine learning since the 1950s [149]. In the past few decades, there have been significant efforts in advancing machine learning. This results in machines being expected to perform at a higher level. Deep learning is an effort in this same direction. This is a portion of machine learning. Research communities are constantly working on exploring new areas and finding practical applications for their work [150]. Fig. 3.1 shows the previous studies that served as the foundation for deep learning [150].

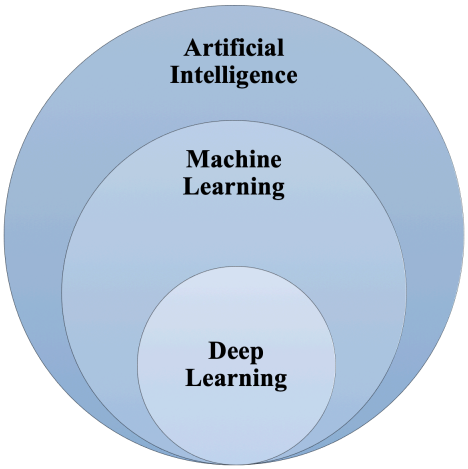

Fig. 3.1 Illustrates the original study that led to the development of deep learning. Deep learning is defined as deep artificial neural networks. The term "deep" is used to describe multiple layers within a neural network. A deep network consists of multiple hidden layers while a shallow network only has a single hidden layer 150].

3.2 Overview of Machine Learning

In the 1950s, the term Intelligent Machinery was coined to introduce a new field in which machines were striving to achieve human-like intelligence [151]. This marked the first step towards exploring a new era. In 1948, Turing and Champernowne discovered chess using only 'paper and pencil' [150,152]. It was the initial computer program for playing chess in the world. The program was created by Turing and Champernowne with pencil and paper, with the calculations being done manually by them - each step would require thirty minutes or longer to confirm [150,152]. In 1951, Dietrich Prinz created a chess machine program that solves mate-in- two moves' puzzles [150]. The program displayed a list of pieces alongside a visualization of the chess board, but on a 10x10 grid, as a knight's move consisted of two single steps [150]. By having a ply-indexed array of piece-list- index, direction and step-counter move generation was done. Christopher Strachey developed the initial Draughts algorithm in 1952. The software could engage in a complete game of Checkers at a moderate pace [149].

In 1943, the McCulloch-Pitts Model of Neuron operated by inserting a 1 or 0 for every input, with 1 indicating true and 0 indicating false. Similarly, a concrete value of 1 was assigned to the threshold, resulting in either a 0 or 1 output if the threshold

was reached or surpassed [153]. In 1949, Donald Hebb suggested that if two neurons fire simultaneously, the link between them becomes stronger [154]. Additionally, this task is a crucial operation needed for the process of acquiring knowledge and remembering information. Frank Rosenblatt developed the first perceptron in 1957, based on the McCulloch-Pitts neuron and Hebb's findings, and in 1961, he demonstrated the perceptron convergence theorem [155]. Three years later, Bernard Widrow engraved the Delta Learning rule. It is utilized for training perceptrons, also known as the Least Square problem [156]. These two are combined to create an effective linear classifier. Nevertheless, in 1969 Marvin Minsky introduced the XOR problem. He also demonstrated that perceptrons are unable to handle linearly inseparable data distributions. After that, there was a lull in NN research until the 1980s [157].

David Rumelhart and James McClelland introduced the multilayer perceptron in 1986 [158]. The Hopfield Network, also known as the Hopfield model, was introduced by John Hopfield in the early 1980s as a type of neural network [159]. The Hopfield network does not have specific input or output neurons; instead, all neurons function as both input and output, and are linked to every other neuron bidirectionally with equal weights. Hinton and Sejnowski (1986) created Boltzmann machines by merging Hopfield networks with simulated annealing [160]. It is a fully connected two-layer neural network. The primary accomplishment in machine learning was Support Vector Machines (Networks) (SVM), introduced in 1995 by Vapnik and Cortes, which had a strong theoretical basis and precise results [161]. That was when the machine learning group was divided into two groups: researchers focusing on NN and researchers focusing on SVM. In 1997, Freund and Schapire created Adaboost, a boosted ensemble of weak classifiers [162]. Breiman investigated AdaBoost in 2001 which involves combining several decision trees [163]. Each tree is built using a random subset of instances and features are randomly selected for each node. RF is the term used to refer to Random Forests. AdaBoost algorithm is susceptible to over-fitting and outlier instances in the data, whereas Random Forest is a more resilient model [149,164].

As we approach the present day, a new era of neural networks known as Deep Learning has emerged. The third rise of NN began around 2005 as a result of various findings gathered over the years by previous researchers Hinton, LeCun, and others [150]. Notably, in 2024, Geoffrey Hinton was awarded the Nobel Prize in Physics, alongside John J. Hopfield, for their foundational discoveries and inventions that enable machine learning with artificial neural networks [165].

3.3 Types of Machine Learning Techniques

Machine Learning algorithms can be categorized into four main groups: Supervised, Unsupervised, Semi-supervised, and Reinforcement learning [97], as depicted in Fig. 3.2. We will briefly talk about each type of learning.

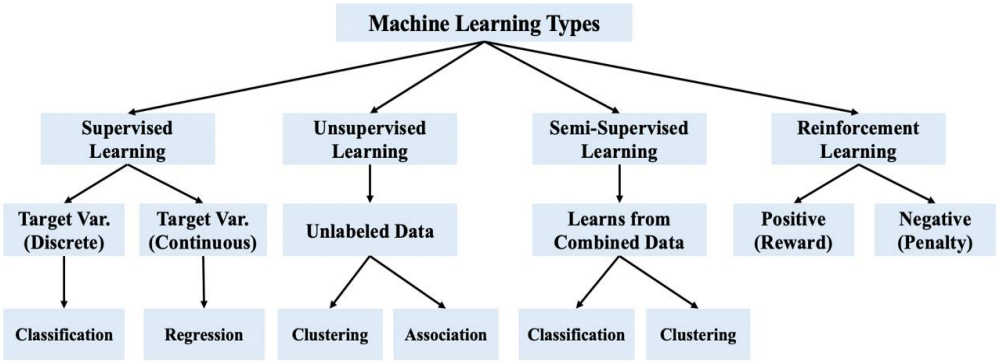

Fig. 3.2 Various types of machine learning techniques [166].

Supervised learning involves machine learning tasks where a function is learned to map input to output using sample input-output pairs [167]. It utilizes annotated training data and a set of training instances to deduce a function. Supervised learning occurs when specific objectives are established for a particular set of inputs to achieve [168]. The most frequently seen supervised tasks include 'classification' for categorizing data and 'regression' for analyzing data trends. An example of supervised learning is predicting the class label or sentiment of a piece of text, such as a tweet or product review, known as text classification [168].

Unsupervised learning is when unlabeled datasets are analyzed without human intervention, making it a data-driven process 169]. This is commonly utilized for extracting creative characteristics, recognizing significant patterns and structures, categorizations in findings, and exploratory intentions. Clustering, density estimation, feature learning, dimensionality reduction, discovering association rules, and anomaly detection are some of the most frequently encountered unsupervised learning tasks [169].

Semi-supervised learning combines supervised and unsupervised methods by using both labeled and unlabeled data [169]. Therefore, it lies somewhere in the middle of learning independently and learning under guidance. In many situations, labeled data is scarce while there is an abundance of unlabeled data, making semi-supervised learning valuable. The aim of a semi-supervised learning model is to improve the prediction outcome compared to using only the labeled data from the model. Semi-supervised learning is applied in various fields such as machine translation, fraud detection, data labeling, and text classification [169].

Reinforcement learning is a machine learning algorithm that allows software agents and machines to assess the best behavior in a specific environment to enhance efficiency, known as an environment-driven approach. This form of learning relies on receiving either rewards or punishments, with the main objective being to apply the knowledge gained [97]. It is a useful tool for developing AI models to enhance automation in complex systems like robotics, autonomous driving, manufacturing, and supply chain logistics, but not recommended for simple problems [166].

Therefore, different machine learning techniques can have a significant impact in developing effective models across various application areas, based on their learning capacities and the characteristics of the data and desired results.

3.4 Artificial Neural Network and Deep Learning

Representation learning is a key component of deep learning, which falls under the broader category of artificial neural network (ANN) based machine learning techniques [170]. Deep learning uses a computational structure with different layers

like input, hidden, and output to learn from data [169]. Deep learning has a major edge over traditional machine learning techniques due to its superior performance, especially when dealing with vast amounts of data. Fig. 3.3 illustrates the overall effectiveness of deep learning compared to machine learning as data volume grows. The extent of variation may differ based on the data features and experimental configuration [166].

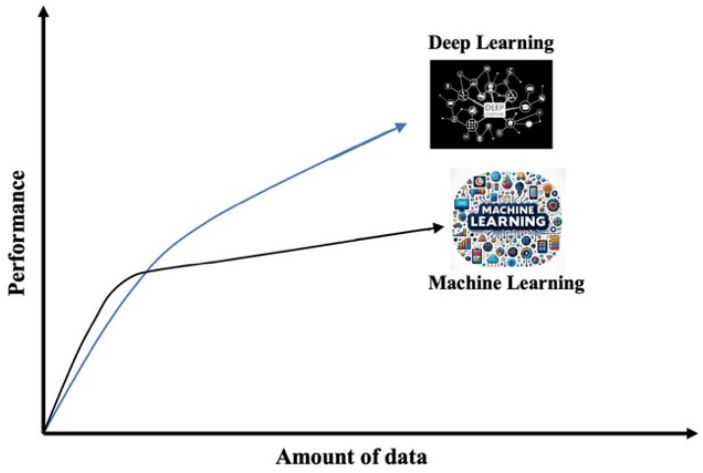

Fig. 3.3 Machine learning and deep learning performance in general with the amount of data [166].

The most common deep learning algorithms are: Multilayer Perceptron (MLP), Convolutional Neural Network (CNN, or ConvNet), and Long Short-Term Memory Recurrent Neural Network (LSTM-RNN) [168]. In the following, we discuss various types of deep learning methods that can be used to build effective data-driven models for various purposes.

MLP: Also known as the feed-forward artificial neural network, is referred to as a multilayer perceptron (MLP), as it serves as the base architecture of deep learning [171]. A standard MLP is a densely connected neural network comprised of an input layer, one or multiple hidden layers, and an output layer, as illustrated in Fig. 3.4. Every node in a particular layer is linked to every node in the next layer using a specific weight. MLP uses the "Backpropagation" method [169], which is considered the foundational element in a neural network, to internally update the weight values during model construction. MLP is affected by the scaling of features and offers the

flexibility to adjust various hyperparameters like the number of hidden layers, neurons, and iterations, leading to a potentially expensive computational model [166].

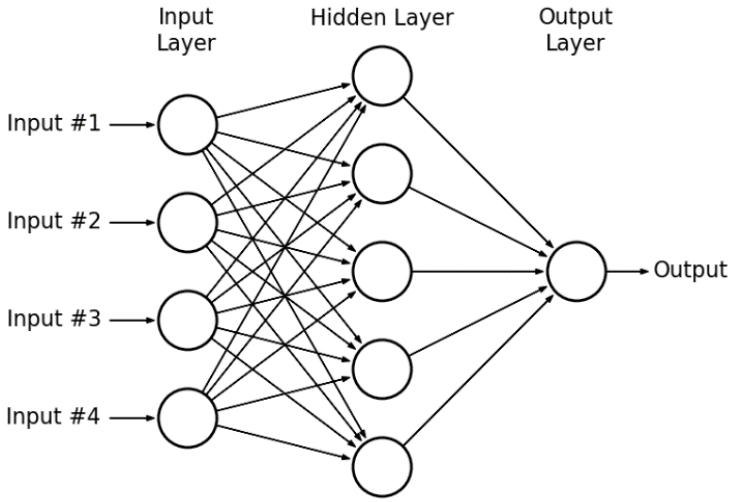

Fig. 3.4 An example of Multilayer Perceptron Network [172].

LSTM-RNN: A type of recurrent neural network (RNN) architecture in deep learning that integrates Long Short-Term Memory (LSTM) units to effectively model and learn from sequential data. Unlike regular feed-forward neural networks, LSTM incorporates feedback connections. LSTM networks excel in handling sequential data, like categorizing, manipulating, and forecasting data from time series data, setting them apart from traditional networks. Therefore, LSTM is applicable for data that is sequential in nature, like time or sentences, and is often used in fields like time-series analysis, natural language processing, and speech recognition [173]. Fig. 3.5 shows how LSTM-RNN algorithm works.

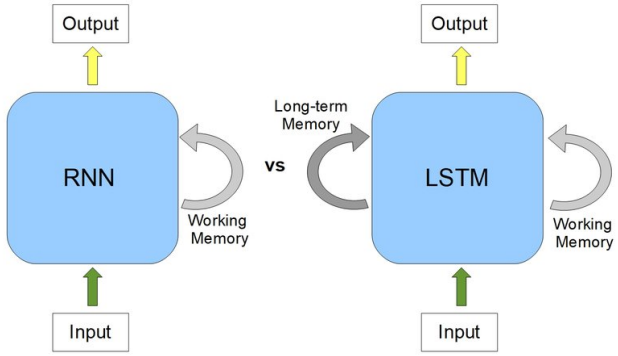

Fig. 3.5 RNN v/s LSTM: RNNs use their internal state (memory) to process sequences of inputs and Long Short-Term Memory (LSTM) network is a variant of RNN, with additional long-term memory to remember past data [174].

CNN or ConvNet: The convolutional neural network (CNN) [92] improves the traditional ANN design, including convolutional layers, pooling layers, and fully connected layers, as depicted in Fig. 3.6.

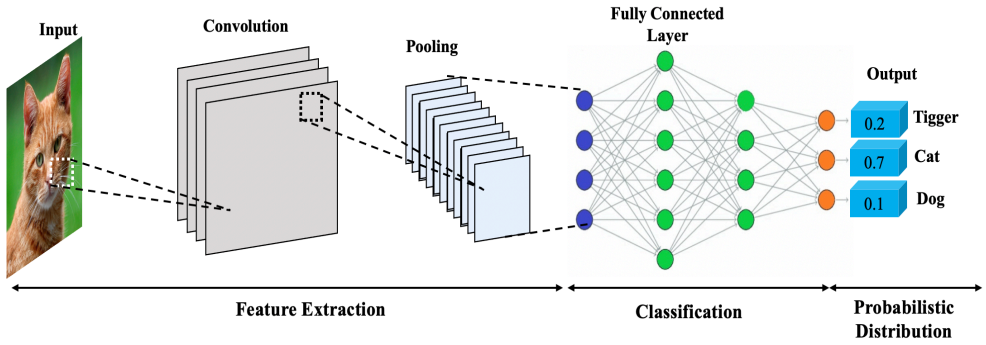

Fig. 3.6 CNN's architecture.

Due to its utilization of the 2D structure of input data, CNN is widely applied in various fields including image and video recognition, image processing and classification, medical image analysis, and natural language processing. Despite being more computationally intensive, CNN can automatically identify important features without manual intervention, making it more potent than traditional NN. Different CNN architectures, like AlexNet, Xception, Inception, VGG, and ResNet, can be applied in the image processing and classification field [92].

In the context of image super-resolution, deep convolutional neural networks have proven to be a highly effective approach for reconstructing HR images from LR inputs. Enhanced SRGAN (ESRGAN), a state-of-the-art model in this domain, represents a significant advancement by integrating multiple optimized CNN layers to improve both perceptual quality and reconstruction accuracy. The following section delves into the architecture and features of ESRGAN.

3.5 Enhanced Super Resolution Generative Adversarial Network

3.5.1 Introduction

Super-resolution (SR) involves generating a HR image from LR inputs. When this task uses only a single LR image, it is referred to as Single Image Super-Resolution (SISR). Traditionally, the objective of SISR has been to minimize the mean squared error (MSE) between the generated image and the original HR image. MSE quantifies the average squared difference between the pixel values of the two images, with smaller values indicating greater similarity. This optimization directly correlates with improving the peak signal-to-noise ratio (PSNR), a widely used metric for evaluating the quality of reconstructed images. PSNR measures the ratio between the maximum possible pixel intensity and the magnitude of noise, expressed in decibels (dB), with higher values indicating better image fidelity.

However, methods focused solely on optimizing PSNR often fail to produce images with high perceptual quality, resulting in outputs that, while quantitatively accurate, lack visually pleasing details [103]. After that, methods focused on perception were suggested. Super- Resolution Generative Adversarial Network (SRGAN) utilizes perceptual loss and generative adversarial networks (GANs) to create images that fall within the natural image dataset. ESRGAN enhances SRGAN by utilizing an architecture that includes RRDBs (Residual-in-Residual Dense Blocks) but excludes BN (Batch Normalization) layers. Furthermore, the discriminator in use was the relativistic average GAN (RaGAN) and the features were utilized pre-activation [175].

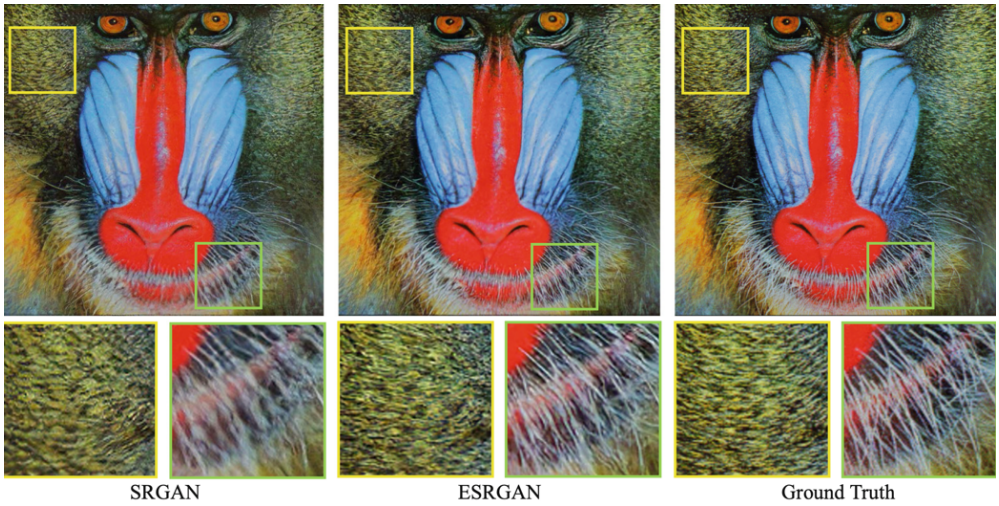

Fig. 3.7 The super-resolution results of ×4 for SRGAN, the proposed ESRGAN and the ground-truth. ESRGAN outperforms SRGAN in sharpness and details [175].

Numerous methods based on perception have been suggested to enhance the visual appearance of SR outcomes [175]. For example, the idea of perceptual loss suggests enhancing the super-resolution model in a feature space rather than in pixel space. Generative adversarial networks in SR were incorporated by to promote the generation of solutions resembling natural images. The addition of the semantic image prior enhances the restoration of texture details. One of the achievements in striving for visually appealing outcomes is SRGAN. The fundamental design incorporates residual blocks and is fine-tuned using perceptual loss within a GAN framework. Using a variety of methods, SRGAN greatly enhances the overall visual quality of reconstruction compared to techniques that focus on PSNR [175]. However, there is still a noticeable disparity between the outcomes of SRGAN and the actual ground-truth images, as illustrated in Fig. 3.7.

3.5.2 Network Architecture

Before diving into ESRGAN architecture, let's first gain a basic understanding of GAN. GANs can create artificial data that appears genuine. One of the applications of GANs is to improve the image quality. The GAN's structure (Fig. 3.8) includes two primary networks: the generator network and the discriminator network. The goal

of the generator network is to produce counterfeit data, while the discriminator network's job is to differentiate between real and fake data, ultimately aiding the generator in creating more authentic data [176].

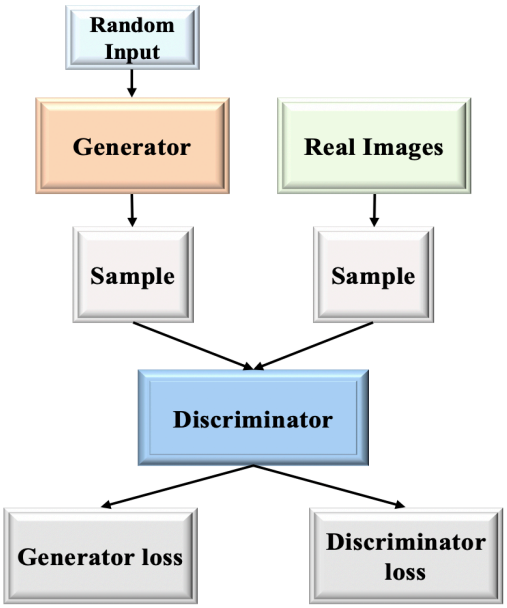

Fig. 3.8 GAN's Architecture [176].

The ESRGAN has a similar structure to the SRGAN but with certain changes (Fig. 3.9). ESRGAN features the Residual in Residual Dense Block (RRDB), which merges a multi-level residual network with dense connections while omitting Batch Normalization.

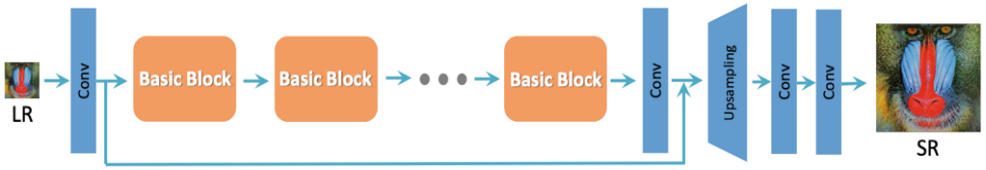

Fig. 3.9 ESRGAN Architecture. They employ the basic architecture of SRResNet, where most computation is done in the LR feature space. We could select or design "basic blocks" (e.g., residual block, dense block, RRDB) for better performance [175].

By modifying generator G to remove BN layers and substitute the Residual-in-Residual Dense Block (RRDB) for the original basic block, the quality of the

enhanced image in SRGAN can be improved [61]. The RRDB integrates multi-level residual network and dense connections, shown in Fig. 3.10 [104].

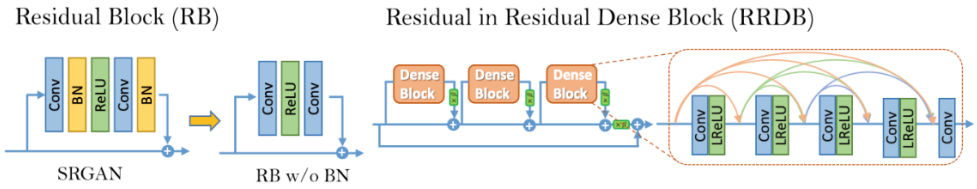

Fig. 3.10 Residual in Residual Dense Block (RRDB). We remove the BN layers in residual block in SRGAN. Right: RRDB block is used in our deeper model and β is the residual scaling parameter [61].

3.5.3 Relativistic Discriminator

In addition to upgrading the generator's structure, they also improve the discriminator using the principles of Relativistic GAN [177]. In contrast to the typical discriminator (D) in SRGAN, which assesses whether an input image x is authentic and natural, a relativistic discriminator aims to determine if a real image x_r appears more realistic compared to a fake image x_f, as illustrated in Fig. 3.11 [104].

More specifically, the standard discriminator is substituted with the Relativistic average Discriminator (RaD) [177], known as D_{Ra}. In SRGAN, the common discriminator can be represented as $D(x) = \sigma(C(x))$, where σ represents the sigmoid function and $C(x)$ is the discriminator output without transformation. Next, the RaD is defined as $D_{Ra}\,(x\_r, x\_f\,) = \sigma(C(x\_r\,) - E\_xf\,[C(x\_f\,)])$, where $E\_xf\,[0]$ denotes averaging all fake data in the mini batch [104].

The loss of the discriminator is subsequently determined as:

$$L_D^{Ra} = -E_{x_r}[log(DRa(x_r, x_f))] - E_{x_f}[log(1 - DRa(x_f, x_r))] \qquad 3\text{-}1$$

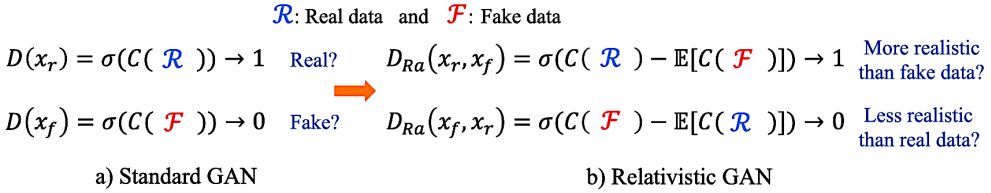

Fig. 3.11 Difference between standard discriminator and relativistic discriminator [104].

The adversarial loss for generator is in a symmetrical form:

$$L_G^{Ra} = -E_{x_r}[log(1 - DRa(x_r, x_f))] - E_{x_f}[log(DRa(x_f, x_r))], \quad 3\text{-}2$$

when x_f is equal to the output of $G(xi)$ and x_i represents the initial LR image. The adversarial loss for the generator is noted to include both x_r and x_f. Hence, this generator leverages gradients from both synthetic and authentic data during adversarial training, whereas SRGAN only utilizes the generated portion [104].

Chapter 4: Experimental setup and Sample preparation

In this chapter, we describe the experimental set-up for SHG microscopy (and P-SHG). Initially, the laser that was used as a source for SHG microscopy will be described. We then detail the microscopy setup used for SHG imaging. Next, we explain the experimental conditions needed for conducting SHG polarization microscopy. Finally, we describe the various procedures involved in preparing the collagen samples.

4.1 SHG and P-SHG imaging setup

4.1.1 Laser Source for SHG Microscopy

The theoretical foundation of nonlinear light-matter interactions has existed for over 50 years, but non-destructive nonlinear microscopy only became feasible in the past decade due to advancements in ultrafast (femtosecond) pulsed lasers. High peak power is essential for efficient harmonic generation as the q^{th} order nonlinear optical effect relies on the photon density of the created photon. Specification of the pulsed lasers including the pulse duration, pulse energy, pulse repetition rate, and the wavelength are significant factors in the field of nonlinear microscopy because not only they determine the efficiency of the nonlinear processes, but they also define whether the laser source can be used for nonlinear microscopy of biological specimen without causing photobleaching or photodamage to the sample. Additionally, factors such as tunable central wavelength, the price of the laser, and its ease of transport may also influence the choice of laser source.

The signal in second-order nonlinear processes like SHG is directly related to the square of the photon density, as explained in Eq. 2-40. This implies that if the pulse duration is reduced by half, the peak intensity of the SHG signal can be increased by a factor of four. Nevertheless, it is important to point out that reducing the pulse duration by a factor of two will cause the pulse to be active for only half the time, leading to the SHG signal being roughly proportional to the inverse of the pulse duration. Therefore, it is beneficial to increase the peak power by minimizing the pulse duration for a given average laser power. Nevertheless, it is important to note

that the ultrashort pulses exhibit a broad spectral range, leading to an increase in group velocity dispersion caused by microscope optics. Stretching the pulses will cause a decrease in peak power. Additionally, if longer pulse durations are employed, a higher average incident power is required to maintain a constant nonlinear signal intensity. A higher average incident power may cause sample damage through linear absorption or heating [178,179]. Considering all these factors, pulse durations in the range of 70–200 fs are optimal for nonlinear microscopy [180].

Pulse repetition rate refers to the frequency of pulses in a pulsed laser, determined by the time between each pulse. The pulse repetition rate in mode-locked lasers depends on the laser cavity's geometry. For a constant average power on the sample with a given pulse width, as the repetition rate increases, the pulse peak power decreases. Hence, higher repetition rates at a given average power will result in a lower signal-to-noise (SNR) ratio. It is also capable of causing harm to the sample by generating heat.

While the general pulse repetition rate used in nonlinear microscopy lies in the range of 10 to 100 MHz [139], there are applications where even SHG imaging is performed using laser sources in the kHz regime. Such kHz repetition rate lasers, often based on a femtosecond or picosecond amplifier system, become especially favorable when higher pulse energies are needed or when thicker samples are in operation and require greater depths of penetration and signal generation. Utilizing a kHz amplifier laser system enables the generation of femtosecond pulses with tens of microjoules of energy, allowing the beam to be defocused to prevent optical breakdown while maintaining reasonable signal acquisition times. This capability makes such systems highly versatile for a wide range of applications [181,182].

The laser wavelength is also a crucial aspect to consider when choosing a laser source, as it is heavily influenced by the optical properties of the sample. The range of wavelengths commonly utilized for biological samples is 800–1700 nm, encompassing the 700–1200 nm spectrum recognized as the "optical window of cells and tissues". Most unstained cells and tissues have low one-photon absorption and

scattering coefficients in this spectral range [180]. It has been suggested that the best excitation wavelength for SHG microscopy of collagenous tissues, the main topic of this thesis, falls within the 800-900 nm range, where SHG intensity is optimal [181,182]. Nevertheless, it is important to acknowledge that the autofluorescence of the biological tissue exists in the same excitation wavelength range, but it is negligible. Additionally, one must consider the varying sensitivity of the detectors to different signal wavelengths caused by different laser excitations. Hence, the laser excitation source must be carefully selected for every sample. Among the various laser sources available, the Ti:Sapphire laser is frequently utilized for nonlinear microscopy because of its short pulse duration and wide tunability from 700–1000 nm. This allows the photoexcitation of a variety of fluorophores. On the other hand, longer wavelengths (> 1μm) are preferred since they have the ability to be utilized in both SHG and THG (Third harmonic generation) microscopy, enhance the depth of penetration by minimizing scattering at the laser wavelength, enable better collection of signals by reducing scattering of harmonic signal wavelength inside the sample, and decrease the excitation of intrinsic fluorophores [183,184]. Thus, lasers with longer wavelengths, like Ytterbium-based lasers which operate in the range of 1020–1050 nm, have gained popularity not only for these optical advantages but also for their operational efficiency, reliability, and ease of use in various applications.

For all the SHG microscopy experiments in this thesis, a mode-locked fiber Ytterbium (Yb) laser (MPB Communications Inc., Montréal, CA) was used. The laser operates at 1040 nm, producing 125 fs pulses at 25 MHz with an average power of 3 W.

4.1.2 SHG Imaging configuration

SHG microscopy was performed using a custom laser stage inverted scanning microscope. The schematic of the main components of the SHG microscope is illustrated in Fig. 4.1. As previously stated, a mode-locked fiber Yb-based laser was utilized as the source. This laser is capable of emitting pulses with an average power of 3 W. However, such a high power is unnecessary for imaging and risks damaging

the samples. To solve this, various techniques can be employed to control the laser power effectively.

Neutral density (ND) filters are a straightforward solution, but they don't offer much flexibility when it comes to adjusting the power range. Another option is an acousto-optic modulator (AOM), which controls the laser power by changing the radio frequency (RF) drive power. Although AOMs can be effective, they can be difficult to align at first, and maintaining alignment between the laser and the microscope can be challenging. For individuals seeking a more automated solution, electro-optic Pockels cells present a viable alternative. These devices deliver comparable performance and can be conveniently controlled through computer interfaces. However, their high cost may limit their practicality, unless the additional functionalities they offer are essential for the application.

A better choice for our setup is using polarization-based methods. Unlike ND filters or AOMs, polarization methods do not deflect the laser beam, making them more reliable for maintaining alignment throughout the optical path. Additionally, polarization techniques offer a broader and continuously variable dynamic range, making them highly suitable for precise power adjustments.

In our case, we utilized an optical approach that combines a half-wave plate ($\lambda/2$) and a polarizer (Glan-Thompson), as shown in Fig. 4.1. The polarizer sets the laser's output to a fixed linear polarization. By rotating the half-wave plate's angle relative to the laser polarization—either by hand or with a motorized control—we can adjust the laser power by a factor of about 100. This translates to a dynamic range of up to 10^4 for the SHG intensity, which is more than enough for our needs. By this method, the average power of our laser can be adjusted from 20 to 125 mW (0.8 to 5 nJ energy per pulse).

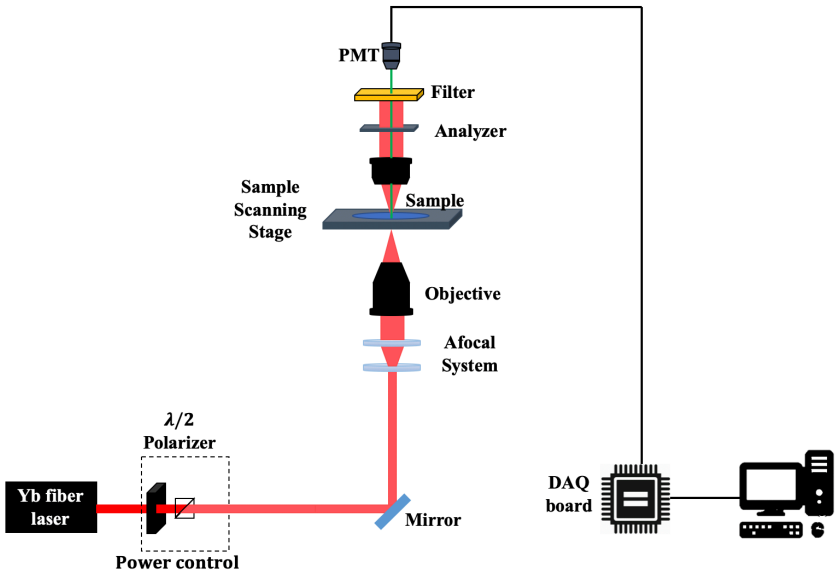

Fig. 4.1 Imaging configuration for SHG setup

The large size of the samples required for imaging made it crucial to use a scanning approach that was both precise and efficient. To address this, a high-speed motorized XY scanning stage (MLS203; Newton, NJ, USA) was employed. This system offered the accuracy and speed necessary to cover wide sample areas without compromising image quality. Focusing the imaging system involved a two-step process: coarse adjustments were carried out using mechanical motors to get the sample roughly aligned, while fine adjustments relied on highly sensitive piezoelectric motors (PI Nano-Z, USA) to achieve optimal focus with precision. Illumination was performed using an air objective (UPlanSApo 10X, NA 0.3, Olympus, Japan), which provided a suitable balance between resolution and working distance, making it an ideal choice for SHG imaging.

To capture the SHG signal emitted by the sample, a high-efficiency condenser was employed. This ensured maximum light collection while minimizing signal loss, which was particularly important given the weak nature of the SHG signals. The collected light was then directed to a photomultiplier tube (PMT; R6357, Hamamatsu Photonics) operating at 800 V, offering the sensitivity required to detect the signal. To further enhance the accuracy of signal detection, a pair of carefully chosen spectral

filters was placed before the PMT. A short-pass filter was used to block any wavelengths longer than 720 nm, effectively eliminating residual input laser light, while a bandpass filter centered at 515 nm isolated the SHG signal, ensuring only SHG reached the detector.

Signal acquisition and synchronization were managed by a multichannel input/output (I/O) board (National Instruments) that worked in conjunction with a custom-developed Python program. This combination allowed for precise control of timing and seamless data acquisition, accommodating the high-speed demands of the imaging process. Despite the efficiency of the system, the relatively large sample size and the acceleration and deceleration periods of the motorized scanning stage resulted in each SHG image requiring several minutes of acquisition time.

Once imaging was completed, the raw data were processed and visualized using Fiji-ImageJ software (NIH, USA). This software provided robust tools for both data analysis and image enhancement, enabling detailed examination of the acquired images. The complete imaging configuration, including the scanning stage, optics, and detection components, is depicted in Fig. 4.1 for clarity. This setup was specifically designed to deliver consistent, high-quality SHG images of collagen samples, ensuring the data collected were reliable and suitable for further analysis.

4.1.3 P-SHG Imaging experimental setup

Polarization analysis, applied to both the excitation and emission in SHG imaging, offers valuable insights into the tissue structural data, particularly their fiber packing [185]. This technique takes advantage of the fact that SHG intensity is strongly influenced by the alignment between the laser's polarization and the orientation of the fibers in the sample. By analyzing this relationship, researchers can measure SHG anisotropy, which provides detailed information about the directional organization of the fibers.

However, this approach has a limitation in that it often fails to measure the direction of fibers oriented orthogonally to the laser polarization. This indicates that while

polarization analysis is highly effective for studying fibers aligned with the polarization, it is less suitable for capturing signals from orthogonal orientations, as stated in Eq. 2-41. Additionally, this principle primarily applies to fibers in the transverse plane, as discussed in Section 2.4. Along the axial propagation direction of the laser beam (Fig. 2.4), the generation of SHG signals is minimal due to the constraints imposed by the rules governing electric dipole interactions, as illustrated in Fig. 1.7.

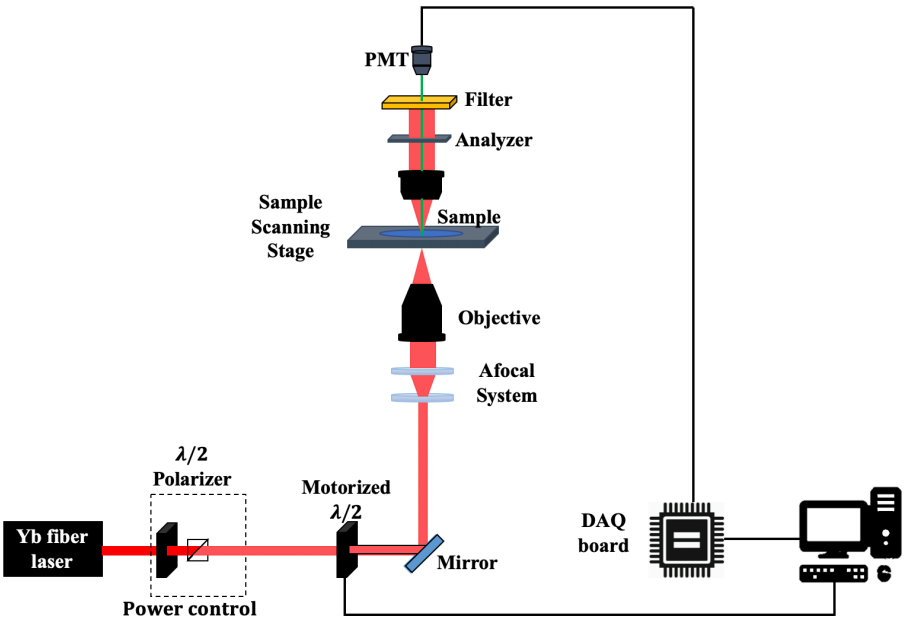

Fig. 4.2 Schematic of P-SHG Imaging setups. The configuration builds upon the SHG imaging setup (Fig. 4.1) by incorporating a motorized half-wave plate to control and rotate the linear polarization of the incident laser beam. This addition enables the acquisition of images at various polarization states.

Extending this method further, polarization analysis can be used to map out spatial variations in fiber organization within tissues, which can reveal changes associated with diseases or developmental processes. By systematically varying the laser's polarization and analyzing the resulting SHG signals, researchers can build a comprehensive picture of the sample's structural anisotropy. Such detailed imaging has applications in fields like cancer research, where changes in the extracellular

matrix's organization often correlate with tumor progression, or in regenerative medicine, where tissue structure plays a key role in functionality [213].

Therefore, for P-SHG imaging, we used the same SHG imaging configuration shown in Fig. 4.1, with adding a motorized half-wave plate to control and rotate the linear polarization of the incident laser beam, which allowed us to capture images at different polarization states. To fully map the polarization dependence of the SHG signal, we recorded images at 18 distinct polarization angles, stepping in increments of 10° from 0° to 170°. This systematic rotation enabled us to gather comprehensive data about the sample's structural anisotropy. The entire process was carefully coordinated using a custom-built Python program, which synchronized the movement of the motorized half-wave plate with the sample scanning. This integration ensured seamless data acquisition, minimizing errors, and maximizing efficiency.

For high-quality P-SHG imaging, random regions of interest of 1000 × 1000 μm were imaged from different samples, and an air objective (UplanSApo 20X, NA 0.75, Olympus, Japan) was used for focusing.

4.2 Sample preparation

Sterol-CoA knockout, wild-type, and heterozygous mice were studied at three critical stages of mammary gland development: the prepubertal stage (week 4), pubertal stage (week 6), and adulthood (week 10). For the adult female mice, their reproductive cycle was carefully monitored using an impedance meter, which measured resistance in the vaginal mucosa. A peak reading indicated the mice were in proestrus; mice were sampled at estrus.

The mice were sacrificed using CO_2 asphyxiation, followed by cervical dislocation. All animal procedures followed the guidelines set out by the Canadian Council of Animal Care (CCAC) and the ARRIVE guideline and were approved by the Institutional Animal Care and Use Committee of the INRS.

To harvest mammary glands, each mouse was secured on a foam pedestal, and the abdomen was carefully opened to expose the mammary glands. The left inguinal mammary glands were quickly harvested to preserve tissue integrity and placed on glass slides for further preparation. The glands were gently stretched to approximate their natural shape using pliers. A layer of parafilm was placed over the gland, which was then flattened under the weight of a heavy metal block for a few minutes. This step ensured uniform thickness and structural consistency. The prepared slides were immediately immersed in Carnoy's fixative solution (60% ethanol, 30% chloroform and 10% glacial acetic acid) for four hours at room temperature. This fixation process preserved the tissue morphology for downstream analysis.

Following fixation, the tissues were rehydrated stepwise by immersion in graded ethanol baths (95%, 75%, 50%, and 25%) and finally in distilled water. The slides were then stained in a carmine alum solution (2% carmine and 5% potassium aluminum sulfate in water) for three hours. This staining imparted a vivid violet color to the mammary epithelium, enhancing the contrast for visualization.

After staining, the tissues underwent gradual dehydration through increasing concentrations of ethanol (25%, 50%, 75%, and 95% EtOH) before being incubated overnight in xylene. This final step cleared the tissues and prepared them for imaging.

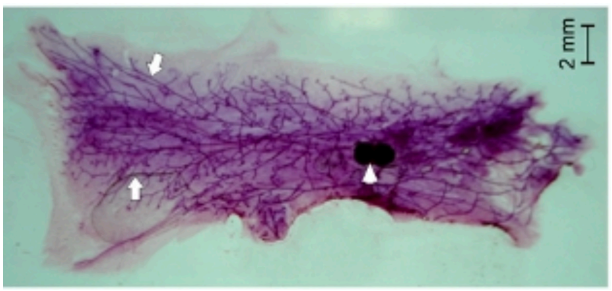

Fig. 4.3 Whole mount of mouse mammary gland. arrows depict the epithelium ducts and arrowhead shows the lymph, modified from Plante et al. [186].

The stained and cleared mammary glands were imaged using a lightbox setup with a camera and measurement key, allowing for detailed comparison between samples (Fig. 4.3). Once digitized, the images were analyzed using ImageJ software. This

analysis focused on quantifying key structural features of the mammary glands, including the extent of epithelial branching, the number of terminal buds, and overall gland architecture. These meticulous procedures provided valuable insights into the developmental changes and structural differences between the various genotypes [186].

Chapter 5: Accelerating P-SHG Imaging with Machine Learning Upscaling

The experimental outcomes of the SHG and P-SHG imaging setup are presented in this chapter. First, the high-quality SHG imaging results of the entire mammary gland are shown, along with a description of their limitations. The low-quality P-SHG images of the entire sample are then described, followed by a discussion of machine learning techniques used to upscale these images in order to improve image quality and speed up imaging time. As demonstrated in our recent published paper [62], machine learning-based approaches can effectively enhance P-SHG image resolution while preserving structural information. High-quality P-SHG images of selected regions of various samples are then shown, and a comparison with the upscaled P-SHG image results is made to assess the method's accuracy. Finally, image quality metric evaluations are performed to ensure the structure of both the original and upscaled images was preserved.

5.1 High-quality SHG imaging

5.1.1 SHG images

Using the SHG imaging configuration (Fig. 4.1), we captured a high-resolution image of mammary gland samples, which is shown in Fig. 5.1. These original high-quality SHG images had a size of 1800 × 800 pixels with the pixel size of 10 μm, allowing for clear capture of intricate structural details. This level of resolution ensured that the delicate features of the mammary gland tissues were accurately recorded, resulting in a clear and comprehensive visualization of their architecture. These images, with their sharpness and rich visual content, were critical tools for analyzing the samples' morphological features. The detailed resolution allowed for the study of key aspects of mammary gland development, such as epithelial structure branching, terminal bud formation, and tissue organization. This high-quality imaging provided structural assessments, and a solid foundation for comparing structural differences across sample groups.

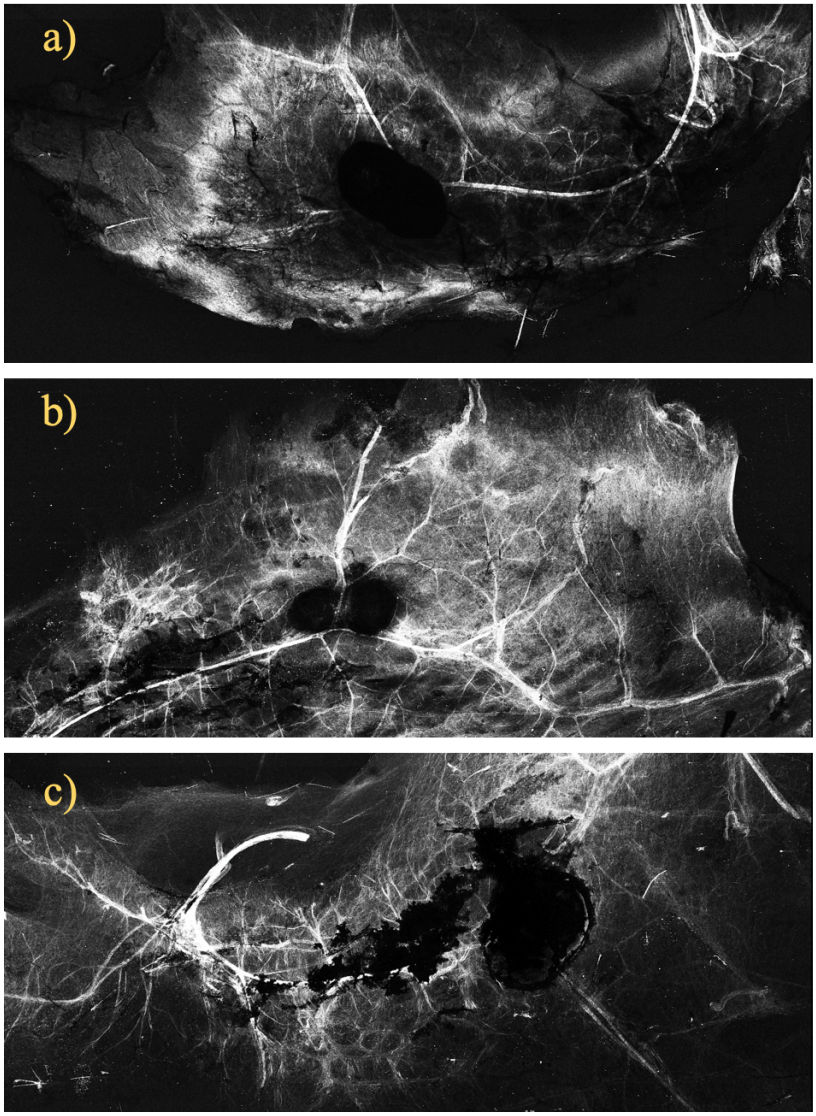

Fig. 5.1 High-quality SHG images of three different mammary gland samples. The size of these images is 1800×800 pixels, which indicated a substantial amount of detail and clarity in each image. The imaging time for each image was approximately 18 min, given the speed of the scanning stage and chosen pixel size of 10 μm.

5.1.2 Histological images

A histological image is a microscopic representation of a sectioned and stained tissue sample. Histological images help in the identification and characterization of diseases, especially cancer, in medical research and diagnostics. Because histological

analysis directly affects medical decisions and the comprehension of intricate biological processes, its accuracy is crucial.

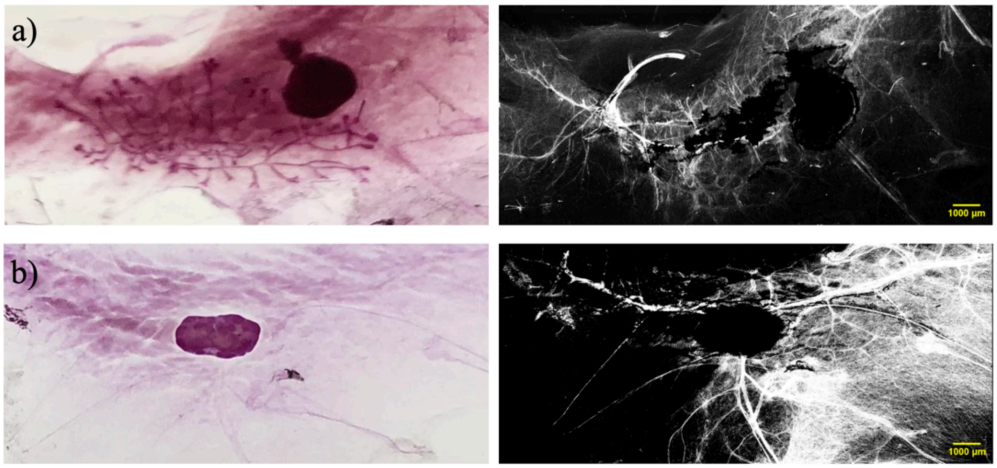

Fig. 5.2 Histological and SHG images of two different mammary gland samples provide a comprehensive view of tissue microstructures.

Fig. 5.2 displays the histological images along with their corresponding SHG imaging counterparts for two different mammary gland samples. A complete knowledge of tissue structure and organization can be obtained by comparing histological images with their SHG imaging counterparts. In order to preserve the structural integrity of the tissue in the improved SHG images, this integration assists in the upscaling process by offering structural guidance from the histological images.

5.2 SHG limitations and P-SHG microscopy

Although SHG microscopy has played an important role in collagen research, depending just on SHG intensity for orientation studies may cause interference and hinder fibril orientation imaging [63]. To overcome these limitations, polarization-resolved SHG microscopy (P-SHG) has emerged, which combines the advantages of SHG microscopy and polarimetry [51,63,187]. P-SHG is commonly used in collagen research due to its ability to provide precise information about fibril structures within the imaging plane. This is especially useful in mammary gland research [188]. In traditional P-SHG imaging, smaller sample areas are imaged and investigated.

However, this approach runs the risk of overlooking critical spatial information, particularly in developmental studies where the macroenvironment is crucial.

As the imaging process expands to larger areas, the coherent nature of the SHG signal can lead to interference effects, potentially canceling out certain structural variations in the sample. While this may limit the detection of finer details, it is an inherent characteristic of SHG imaging and is considered an acceptable trade-off in the context of our research. In cancer boundary research, the wide alignment of the collagen barrier is useful [189]. Similarly, understanding macroenvironmental effects on mammary gland development requires whole-sample P-SHG imaging. While this approach may lack some smaller variations and fibers, the comprehensive perspective it provides on collagen alignment across the entire gland is critical for a thorough understanding of the developmental processes at work.

Fig. 4.2 shows an imaging configuration that can be used for P-SHG imaging. Changing the half-wave plate in this imaging setup allows us to control the polarization direction of the incident laser pulse to scan the polarization dependence of the SHG signal.

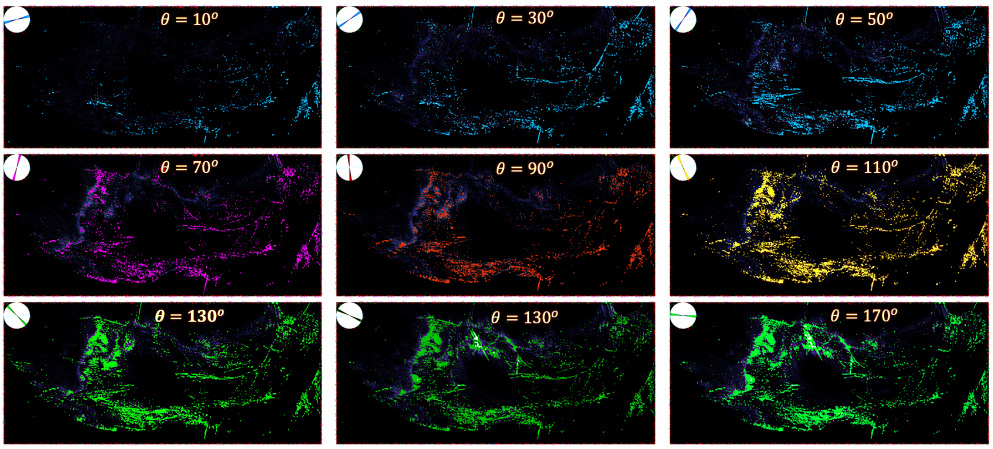

Fig. 5.3 High-quality P-SHG images of a mammary gland sample captured at nine different input laser polarization angles.

Fig. 5.3 shows P-SHG images of a mammary gland sample at various laser beam polarization angles. The incident laser beam polarization can be aligned by controlling and rotating the half-wave plate, as shown in the P-SHG setup (Fig. 4.2).

According to Eq. 2-39, the SHG intensity of a particular fiber is maximized when the incident laser polarization is parallel to the fiber direction, and both are in the same plane. The P-SHG results in Fig. 5.3 show that fibers aligned with the laser polarization exhibit the highest SHG signal intensity. In the visualization, different polarization angles are represented by distinct colors to illustrate the signal variation with polarization. As a result, we can easily estimate the fiber direction for different mammary gland samples using P-SHG images, as discussed in the following section.

We need to capture 18 high-resolution images for complete polarization scanning using the P-SHG imaging method. Our setup uses high-quality SHG or P-SHG images with a size of 1800 × 800 pixels (with pixel size of 10 μm), allowing for clear capture of structural details. The imaging time for each image is approximately 18 minutes, based on the scanning stage speed and pixel size of 10 μm. As a result, it will take more than 4 hours to image each sample, implying a continuous laser-sample interaction that could damage or dry the sample. To address these issues and prevent sample damage, we can reduce imaging time by lowering image quality. Compared to high-quality images, the original low-quality images have a lower resolution of 225×100 pixels with pixel size of 80 μm. This lower resolution implies a significant loss of detail and sharpness when compared to higher-quality counterparts.

To reduce imaging time and mitigate potential sample damage, we opted to lower image resolution, which significantly decreases acquisition time. While high-quality P-SHG images have a size of 1800 × 800 pixels (pixel size of 10 μm) and require approximately 18 minutes per image, reducing the resolution to 225 × 100 pixels (pixel size of 80 μm) reduces the imaging time to just 45 seconds per image. This allows us to capture all 18 polarization angles for P-SHG in the same amount of time required for a single high-resolution image. However, the lower resolution results in a substantial loss of detail and sharpness, making the images unsuitable for P-SHG

analysis with the existing method. To overcome this limitation and retain the advantages of faster imaging, we employed machine learning-based image upscaling techniques. These methods enhance the resolution and quality of low-resolution images, making them compatible with the P-SHG analysis while maintaining significantly reduced imaging times.

5.3 Machine Learing models for Upscaling images

Multiple models were used for image upscaling, including Ultrasharp_4X [190], ESRGAN_Nomos2 K [191], NMKD [191], 4X-UniScaleV2_Sharp [192], and ESRGAN [193]. The upscaling was carried out using the ChaiNNer program, which can be found at [194]. Furthermore, we investigated guided upscaling techniques using PixTransform [195], using high-quality SHG images as references to guide the upscaling of 18 distinct P-SHG images over a range of iterations (1,000-30,000) and channel-split modes. This process was optimized for performance by combining an RTX 3060Ti GPU with a local computing setup.

5.3.1 Quality Metrics

To make sure that the structure and integrity of original images were preserved, quality metric evaluations were performed. There are various quality metrics for comparing the output of image upscaling models to the original high-quality SHG images. So, in the following section, we will present some of these quality metrics, including the Peak Signal-to-Noise Ratio (PSNR), Structural Similarity Index (SSIM), Perceptual Image Quality Evaluator (PIQE), and Naturalness Image Quality Evaluator (NIQE) are the ones that were used in this study. Since one metric is not appropriate for considering every aspect of a generated image, multiple image quality metrics were used [172].

The PSNR measures the maximum pixel value ratio to the mean squared error in an image [197]. Higher PSNR values indicate better image quality and correlate well with perceived visual quality. SSIM evaluates the luminance, contrast, and structure between two images and considers human visual perception. The SSIM ranges from

-1 to 1, where 1 indicates identical images, 0 indicates no similarity, and -1 indicates anticorrelation [197]. PIQE is designed to evaluate the visual quality of images in a manner that closely aligns with human perception [198]. It incorporates various visual features such as contrast, luminance, and texture to compute a quality score that reflects perceived image quality [198]. NIQE explicitly targets the assessment of naturalness in images [199]. It computes features related to the distribution of pixel values, luminance, contrast, and other statistical properties [199]. Unlike SSIM and PSNR, which require a reference image, NIQE and PIQE do not require a reference image [198,199].

To give a thorough evaluation of the models and upscaled images, we also looked at the intensity, texture, and contrast metrics. The intensity metrics comprised minimum and maximum intensity values, the median intensity, mean intensity, and standard deviation of intensity. While the standard deviation of the intensity quantifies the variation in pixel intensities, the mean intensity represents the average pixel intensity of the image [62]. The minimum and maximum intensities show the range of pixel values in the image, while the median intensity gives the middle value of pixel intensities [62].

Michelson contrast and root mean square (RMS) contrast were among the contrast metrics used [200]. While the Michelson contrast assesses the contrast between the maximum and minimum pixel intensities, the RMS contrast measures the image's overall contrast, indicating the degree of contrast enhancement [200].

Gray-level co-occurrence matrix (GLCM) metrics like dissimilarity, homogeneity, energy, and correlation were used in texture analysis [201]. The difference between neighboring pixel values is measured by dissimilarity; lower values denote a more homogeneous texture. A uniform texture is indicated by homogeneity, which is the proximity of the GLCM diagonal to the element distribution [201]. Textural homogeneity is measured by the energy, or angular second moment, and the linear dependence of pixel values is measured by the correlation [201].

Additionally, we included sophisticated metrics like the Edge Preservation Ratio (EPR) for evaluating edge retention [202], Visual Information Fidelity (VIF) for quantifying visual information preservation [203], the Feature Similarity Index (FSIM) for evaluating structural similarity [204], and local binary patterns (LBP) for texture analysis [205]. The statistical characteristics of the images were compared using histogram-based metrics like Kullback-Leibler divergence, histogram correlation, and histogram intersection [206].

5.3.2 Model performance and selection criteria

To objectively evaluate the performance of each upscaling method, we applied the quality metrics introduced in the previous section. The results of this evaluation are shown in Table 5.1.

Table 5.1 Comprehensive performance comparison of upscaling models

Method	mSSIM Ratio	NRMSE Ratio	PSNR Absolute Improvement	PSNR Percentage Improvement	Visual Inspection
UltraSharp	0.939	1.036	-0.92	-5.02%	Most true to original
ESRGAN	0.953	1.047	-0.70	-3.84%	Introduced noticeable artifacts in complex patterns
NMKD	0.691	1.164	-1.83	-10.08%	Tended to oversmooth, losing fine details
NOMOS	0.866	1.127	-1.44	-7.90%	Better detail preservation but tended to oversmooth and artifact
PixTransform	1.335	1.100	-1.13	-6.22%	Not suitable for P-SHG application
UniScale	0.627	1.209	-2.20	-12.12%	Significant loss of detail and increased blurring

This table offers a comprehensive side-by-side comparison of the evaluated upscaling models based on key performance metrics, providing insight into their effectiveness. One of the primary metrics, the mSSIM ratio, measures how well the upscaled image retains structural similarity to the original image, with higher values signifying better preservation. Among the models tested, Ultrasharp_4X (0.939) and ESRGAN (0.953)

excelled in maintaining structural integrity, while UniScale (0.627) lagged significantly, indicating poor performance in this area.

Another critical metric, the NRMSE ratio, quantifies the level of error introduced compared to the original image. Values closer to 1 suggest minimal error, and again, Ultrasharp_4X (1.036) and ESRGAN (1.047) performed remarkably well. These results highlight their capability to minimize discrepancies during the upscaling process.

The PSNR improvement, which measures the change in image quality, further supports the findings. In this case, smaller values close to zero indicate better preservation of quality. While all models experienced some degree of degradation, ESRGAN (-0.70, -3.84%) and Ultrasharp_4X (-0.92, -5.02%) demonstrated the least quality loss, reaffirming their reliability in retaining critical image details.

In addition to the quantitative metrics, visual inspection played a crucial role in evaluating the models. This qualitative assessment focused on the ability to preserve fine details, texture, and the overall integrity of the original images without introducing noticeable artifacts. Ultrasharp_4X emerged as a standout performer, striking an excellent balance across all metrics. Its high mSSIM score reflects robust structural preservation, while the minimal error indicated by its NRMSE ratio underscores its precision. Despite a slight PSNR degradation, visual inspection confirmed that Ultrasharp_4X produced upscaled images that were strikingly true to the originals, maintaining essential details and avoiding any significant distortions.

This balanced performance positions Ultrasharp_4X as an ideal choice for applications where high fidelity and minimal error are critical, demonstrating its superiority over the other tested models. Its ability to consistently deliver high-quality results makes it a dependable tool for advanced imaging needs.

While Table 5.1 compares upscaled models using fundamental image quality metrics (MSSIM, PSNR, and NRMSE), a more specialized analysis is required to fully understand how each upscaled image compares to the original high-quality image

across various image quality dimensions. To accomplish this, we used a set of specialized metrics centred on feature similarity, visual information fidelity, edge preservation, texture similarity, and intensity distribution. Table 5.2 shows the results of these analyses. These metrics provide complementary information about how well each upscaling method maintains or improves the various aspects of the original image quality.

Table 5.2 presents additional insights based on the comparison metrics. FSIM scores were high for all models (ranging from 0.896 to 0.919), with NOMOS slightly outperforming the others. VIF scores vary more, with UniScale (0.117) being the highest, followed by NOMOS (0.103) and NMKD (0.090). LBP_Similarity demonstrated significant improvements for all models when compared to the low-quality image (0.471), with PixTransform (0.960) and UniScale (0.891) performing the best.

Table 5.2 Specialized Image Quality Metrics for Upscaled vs. Original Image Comparison

Metric	Original vs Low	Ultrasharp_ 4X	ESRGAN	NMKD	NOMOS	Pix-Transform	UniScale
FSIM	0.884	0.910	0.904	0.914	0.919	0.918	0.896
VIF	0.046	0.062	0.054	0.090	0.103	0.089	0.117
EPR	0.042	0.019	0.017	0.013	0.016	0.673	0.014
LBP Similarity	0.471	0.758	0.836	0.886	0.693	0.960	0.891
Histogram Intersection	0.898	0.894	0.884	0.959	0.863	0.708	0.728
Histogram Correlation	0.964	0.962	0.937	0.990	0.935	0.839	0.722
KL Divergence	0.130	0.049	0.084	0.014	0.086	1.377	0.237

NMKD performs particularly well in histogram-based metrics, with high scores in histogram_intersection (0.959) and histogram_correlation (0.990), indicating that it is very effective at preserving the original image's overall intensity distribution. The Kullback-Leibler Divergence reveals that NMKD (0.014) and Ultrasharp_4X (0.049) outperform other models, indicating better preservation of the original image's intensity distribution. However, PixTransform had a higher KL_Divergence (1.377), indicating less similarity to the original distribution in this regard.

In our investigation into various upscaling techniques, we first considered the PixTransform-guided upscaling approach, which has the potential to use high-quality SHG images as references to improve the upscaling process. In theory, this method provides a promising avenue for improving the resolution and detail of P-SHG images, which is critical for accurately identifying and analyzing collagen fiber orientation and other microstructural details. However, P-SHG imaging has unique features, where image properties such as signal intensity and fiber orientation change dynamically with different input laser polarization angles. These dynamic changes present unexpected challenges. During preliminary trials, we discovered that while PixTransform effectively filled in missing details in regions with low signal-to-noise ratio (SNR) or where details had been lost due to low resolution, it did so without considering the critical angle-dependent variation properties of P-SHG images. Specifically, the guided upscaling process, in its attempt to interpolate and enhance image details based on high-quality references, introduced artifacts and inaccuracies by "filling in the gaps" in a way that was inconsistent with actual, angle-dependent SHG signal variations. This discrepancy stems from the model's inherent design to generalize from reference images, resulting in misrepresentations where P-SHG imaging relies on precise laser angle-specific signal variations to accurately establish fiber orientations. The consequent images, while visually improved in terms of sharpness and resolution, misrepresented the fundamental biological structures. This was due to the overlaying or amplifying details that did not correspond to the actual orientation and distribution of collagen fibers, as determined by varying laser angles.

Furthermore, we investigated the ESRGAN, another sophisticated upscaling model known for its impressive improvements in a variety of imaging contexts. Despite its capabilities, ESRGAN did not meet the stringent requirements for accuracy and detail preservation in P-SHG image upscaling. Similar to guided upscaling attempts, ESRGAN introduced changes that compromised the integrity of our imaging technique, making it an unsuitable option.

After careful evaluation, it became clear that not all models performed equally. Despite each method's potential, only Ultrasharp_4X proved to be a viable solution that closely approximates the quality and fidelity of original high-quality SHG images. This finding was critical because our primary goal was to ensure that the upscaled images retained as much original detail and structural integrity as possible while avoiding artifacts or distortions that might compromise analytical accuracy.

A visual comparison of the upscaling methods reveals differences in performance and outcome quality, as depicted in Fig. 5.4.

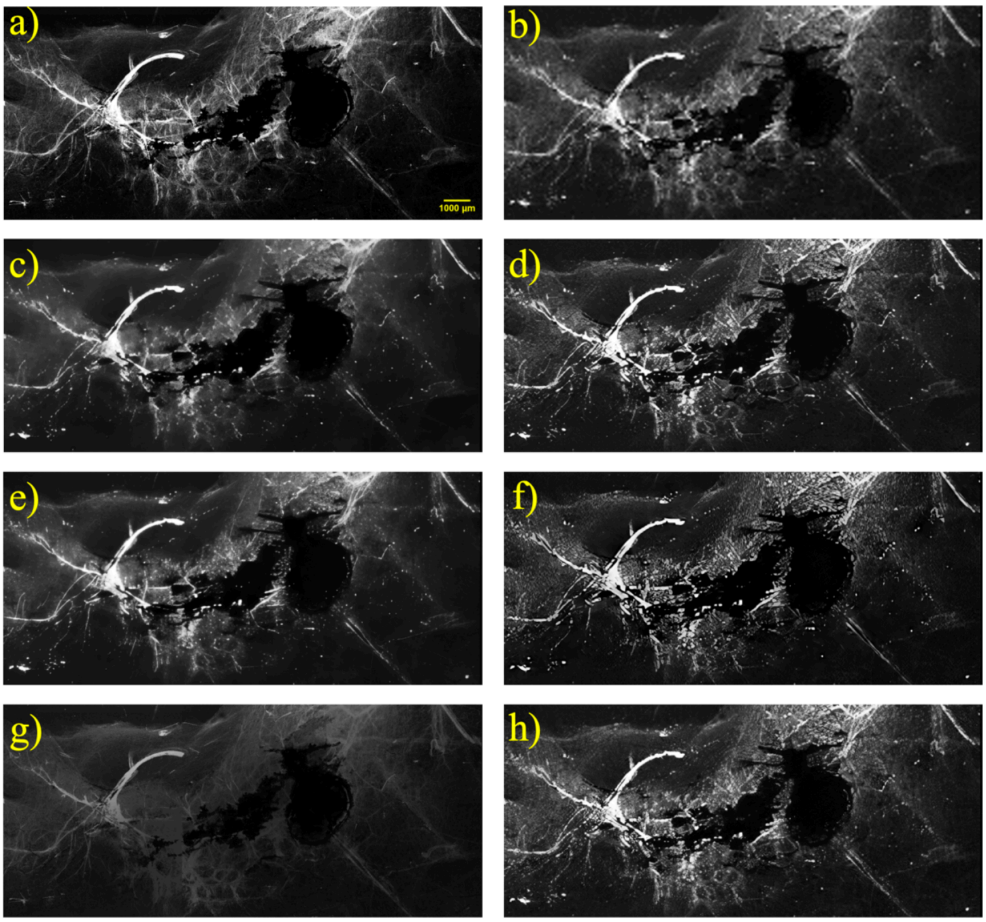

Fig. 5.4 A comparison of upscaled models for P-SHG imaging. This figure shows a side-by-side comparison of a) original high-quality and b) low-quality SHG images versus images upscaled using various models such as c) ESRGAN, d) Nomos2K, e) Ultrasharp_4X, f) NMKD, g) guided upscaling via PixTransform, and h) Uniscale.

P-SHG requires absolute precision and detail fidelity. Implementing "Ultrasharp_4X" with the ChaiNNer program represents a significant step toward expanding advanced P-SHG imaging enhancement. Despite its impressive capabilities, accessibility is limited. The program was designed for ease of use and required little deep learning knowledge from users. The hardware requirements were clearly documented, and the computational resources of most modern research laboratories were found to be adequate for basic operations.

5.4 Original vs. upscaled SHG images

The high-quality original image of the sample, along with the low-quality image and its upscaled counterpart of two different mammary gland samples, are shown in Fig. 5.5.

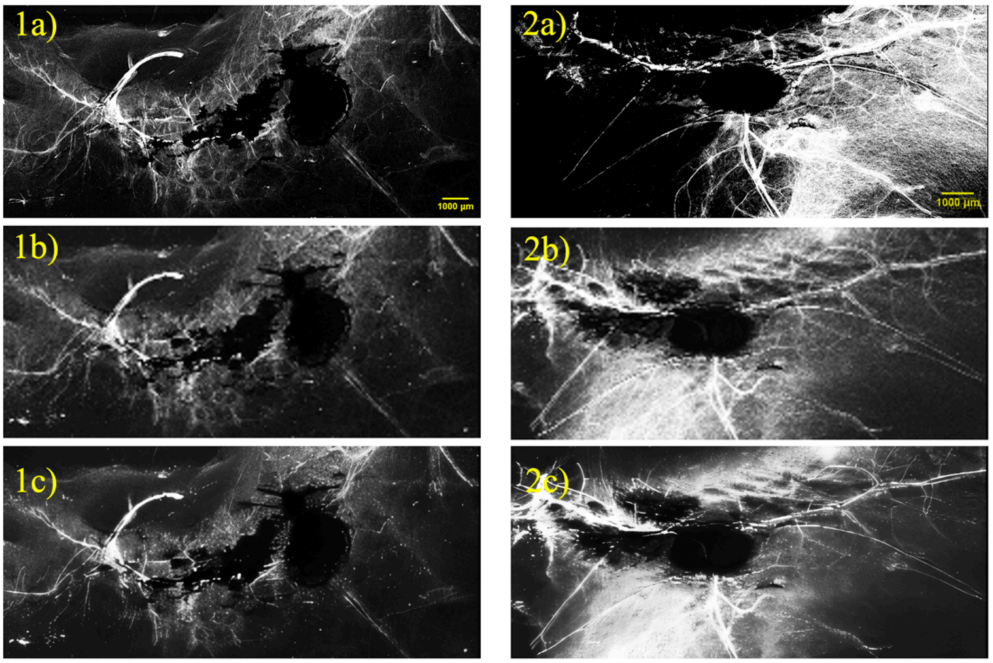

Fig. 5.5 This figure divides images into three categories: original high quality (1a, 2a), original low quality (1b, 2b), and upscaled images (1c, 2c) from two different samples. High-quality images (1a,2a) had a resolution of 1800 × 800 pixels, while low-quality images (1b,2b) had a resolution of 225 × 100 pixels. Upscaled images (1c,2c) had a size of 3600 × 1600 pixels.

The original high-quality images provided detailed visual information whereas the low-quality images had reduced resolutions of 225 × 100 pixels and hence did not contain detailed information sharp enough for P-SHG analysis.

To address this limitation, we employed the Ultrasharp_4X model, based on ESRGAN, to upscale the low-quality images. This method was selected from among upscaling approaches since it gives the best performance for our use case. This method did not work well because in P-SHG, changing the laser input angle causes changes in the SHG based on fiber alignment. We discovered that the model attempted to fill in missing intensities and omit specific pixels in order to shape the image based on the reference image; Thus, individually upscaling each P-SHG image was best for our needs. Using Ultrasharp_4X twice increased image resolution by 16x, resulting in 3600 × 1600 pixels. While upscaled images appear more detailed and visually larger than their original counterparts, they frequently suffer from quality degradation due to the interpolation and extrapolation involved in the upscaling process. To mitigate these issues, detailed quality control measures were implemented to evaluate the fidelity of the upscaled images.

5.5 Quality control of upscaled SHG images

At this stage, we have used the ESRGAN (Ultrasharp_4X) model to upscale low-quality P-SHG images of the entire mammary gland sample. Now, we can obtain high-quality P-SHG images of a few areas of various samples and compared the outcomes with upscaled P-SHG image results in order to assess the accuracy of the method. Our evaluation strategy included a combination of no-reference and full-reference image quality metrics, as well as statistical analysis using analysis of variance (ANOVA), to provide a comprehensive understanding of the upscaled image quality in comparison to their original high-quality counterparts.

5.5.1 No-reference quality metrics

We started with no-reference quality metrics, specifically the NIQE and the PIQE, which evaluate image quality without requiring a reference image. These metrics are

especially useful in determining the perceptual quality of upscaled images. The results for two different mammary gland samples are summarized in Table 4.

Table 5.3 No-reference quality metrics for two different mammary gland samples

Sample	Method	Low-quality image	Upscaled image	High-quality image
a	NIQE	8.940	3.186	6.707
	PIQE	40.797	23.234	46.404
b	NIQE	9.908	2.749	7.532
	PIQE	89.992	31.906	52.931

The lower scores for upscaled images across both the NIQE and PIQE metrics indicate an improvement in image quality after upscaling. This indicates that our method effectively improved the perceptual quality of the images, making them more natural and visually appealing than the original high-quality images. These findings support the effectiveness of our upscaling method, though it is important to note that there may be a difference between computational quality assessments and human perception. PIQE and NIQE make sense in this context because they are non-reference image quality metrics that are ideal for assessing the quality of upscaled images when there is no high-quality original to compare.

Their application provides a quantitative method for evaluating image quality improvements that may not be immediately apparent through visual inspection alone. Despite concerns that these metrics may be tuned for "computer perception," the lower scores for predicted images compared to source images indicate a successful enhancement. However, the difference between these scores and human perception emphasizes the importance of using a variety of metrics, including full-reference metrics like MS-SSIM, PSNR, and NRMSE, to obtain a comprehensive evaluation of image quality post-upscaling.

5.5.2 Full-reference quality metrics

Next, we used the full-reference metrics MS-SSIM, PSNR, and NRMSE to evaluate the quality of the images. These metrics, which emphasize structural similarity, signal fidelity, and error, provide different perspectives on image quality but requires a reference image for comparison. Table 5 provides a summary of the findings.

Table 5.4 Full-reference quality metrics for two different mammary gland samples

Sample	Method	Low-quality image	Upscaled image
a	MS-SSIM	0.33	0.31
	PSNR	18.31	17.39
	NRMSE	0.28	0.29
b	MS-SSIM	0.01	0.01
	PSNR	9.14	9.14
	NRMSE	0.56	0.56

This upscaling algorithm's ability to preserve the structural integrity and signal fidelity of the images is demonstrated by the comparable MS-SSIM, PSNR, and NRMSE values between the source and prediction images for both samples. The general similarity in the scores indicates that our approach is capable of improving the images without sacrificing the original quality, despite minor differences in a few metrics. In order to statistically determine the variations in image quality among the Low-quality, Upscaled, and High-quality image groups, we performed ANOVA in addition to an extensive evaluation of the no-reference and full-reference quality metrics. We were able to thoroughly test for significant variations in the image quality generated by our upscaling procedure thanks to this statistical method. Following, we combine the results of the ANOVA with the quality metric assessments that have already been addressed.

5.5.3 Analysis of variance (ANOVA) results

We used ANOVA to statistically compare the no-reference and full-reference metrics applied to assess the image quality across high-quality and upscaled image groups.

The effectiveness of our upscaling techniques was assessed quantitatively by using ANOVA to find any statistically significant variations in the image quality. Table 5.5 presents the findings.

Table 5.5 ANOVA results

Metric Category	Metric Details	F-Value Range	P-Value Range	Highest Effect Size (η^2)
No-reference Quality Metrics	NIQE and PIQE combined	0.654	0.543	0.109
Full-reference Quality Metrics	MS-SSIM, PSNR, and NRMSE combined	0.003 to 0.006	0.948 to 0.982	0.001
Texture	Various texture metrics	0.442-1.651	0.216-0.811	0.248 (Homogeneity)
Contrast	Various contrast metrics	0.233-1.199	0.359-0.941	0.194 (RMS Contrast)
Comparison	Various comparison metrics	0.087-2.239	0.112-0.993	0.309 (Hist. Correlation)

In Table 5.5, the F-value represents the ratio of the variance between groups to the variance within groups, with larger values indicating greater differences between groups [207]. A p-value indicates the probability of obtaining test results at least as extreme as the observed results, assuming that the null hypothesis is correct [207]. A p-value less than 0.05 is typically considered statistically significant. The effect size (η2) quantifies the magnitude of the difference between groups with values of 0.01, 0.06, and 0.14 typically considered small, medium, and large effects, respectively [208].

For every set of metrics, the ANOVA results showed no statistically significant differences between the source and prediction groups or between upscaling techniques ($p > 0.05$). However, the variation in effect sizes (η^2) and F-values indicates practical differences that should be considered. The no-reference quality metrics (NIQE and PIQE) showed a medium effect size ($\eta^2 \approx 0.109$), indicating a noticeable impact on perceptual image quality. In contrast, the full-reference quality

metrics (MS-SSIM, PSNR, and NRMSE) show a very small effect size ($\eta^2 \approx 0.001$), suggesting high preservation of structural similarity and signal fidelity.

Among the specific metric categories, comparison metrics, particularly Histogram Correlation, showed the largest effect size ($\eta^2 \approx 0.309$), followed by texture metrics (homogeneity, $\eta^2 \approx 0.248$) and contrast metrics (RMS Contrast, $\eta^2 \approx 0.194$). These moderate effect sizes suggest practical differences in these aspects of image quality across the upscaling methods, despite the lack of statistical significance.

It is crucial to maintain that a lack of statistical significance doesn't always mean that no significant differences exist. Numerous factors could be to blame for this, including the nature of the improvements generated by our upscaling method, which may be consistent but subtle, high variability within groups, and our relatively small sample size, which may limit the power of statistical tests.

Even though some measurements didn't show statistically significant improvements, they still had a noticeable impact. This suggests that when choosing an image upscaling technique for specific P-SHG imaging applications, it's important to consider both statistical significance and practical benefits. Our research shows that our ESRGAN-based method can effectively improve the quality of low-resolution images without compromising their original structure or appearance. This makes it a promising tool for various bioimaging applications.

Therefore, our upscaling techniques were thoroughly validated by combining the ANOVA results with the no-reference and full-reference quality metrics. This analysis shows that low-resolution images can be improved while maintaining their quality using our ESRGAN-based method. The moderate effect sizes in some metrics and the absence of statistically significant differences imply that the upscaling procedure has no noticeable effect on the structural or perceived quality of the images.

This validation highlights the method's potential use in bioimaging and other fields where image integrity is crucial and validates its effectiveness. The subtle variations identified by the effect size analysis offer helpful direction for refining upscaling

techniques for particular imaging scenarios, guaranteeing that the most important elements of image quality are maintained in every application.

5.6 P-SHG analysis results

Before examining the P-SHG analysis, we used CurveAlign measurements to see if this technique could be applied to low-quality images. CurveAlign is a popular tool for measuring fibrillar collagen at the tumour boundary [209]. This feature is a fibrillar collagen quantification platform based on curvelet transform. Curvelet transform (CT) offers special capabilities for edge enhancement and image denoising. Additionally, curvelets can track individual fibers and fiber branches, whether they are straight or curvy, by directly providing an optimal sparse representation of the collagen image [210].

CurveAlign analysis consists of a few steps; first, a two-dimensional fast discrete curvelet transform is performed. Second, based on the scale of interest and the threshold of the remaining coefficients, the center and spatial orientation of each curvelet is found, and by grouping the adjacent curvelets, the local fiber orientations are estimated [211]. Fig. 5.6 presents the results of the CurveAlign measurements conducted on low-quality images of the two mammary gland samples.

Using CurveAlign software, we compared two sets of samples in Fig. 5.6: the original high-quality images (1a, 2a), their lower-quality versions (1b, 2b), and images enhanced through ESRGAN-based upscaling (1c, 2c). CurveAlign effectively detects the orientation of collagen fibers in high-quality images (1a, 2a), demonstrating the efficiency of software with images of sufficient resolution and clarity. However, as mentioned. However, obtaining the 18 high-quality images needed for P-SHG analysis necessitated prolonged laser exposure, which could damage the samples and affect experimental reproducibility. Furthermore, extended periods outside of the chemical bath may cause the samples to dry, altering their morphology and potentially extinguishing or reducing the SHG signal. As a result, it is preferable to reduce laser exposure and speed up imaging times.

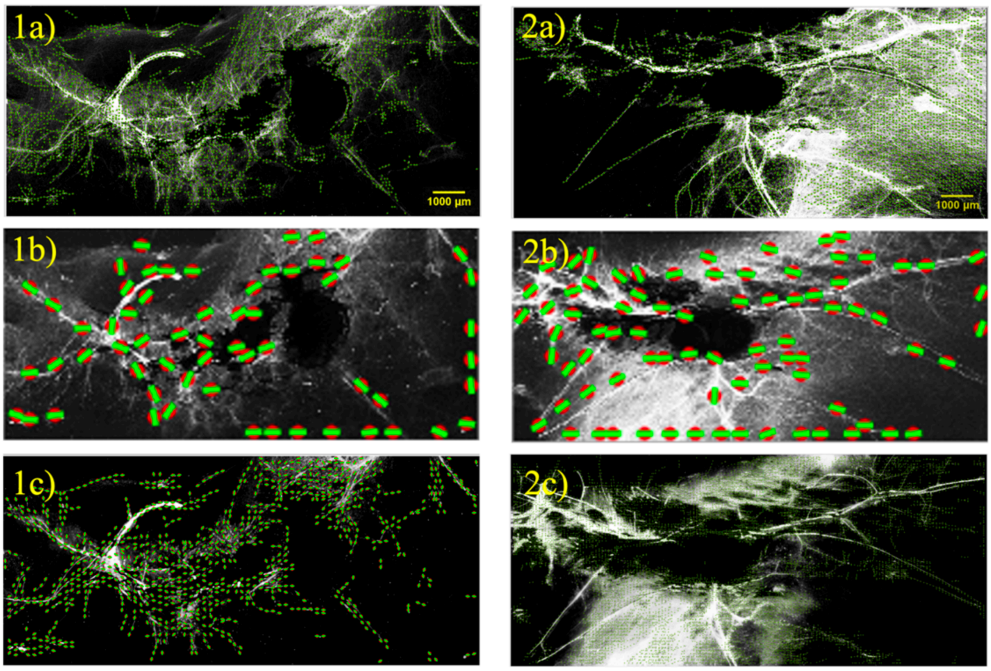

Fig. 5.6 CurveAlign analysis of original high-quality (1a, 2a), low-quality (1b, 2b), and GAN-upscaled (1c, 2c) images.

Examining the lower-quality images (Fig. 5.6, 1(b), 2(b)) showed that CurveAlign and our special P-SHG algorithm had serious limitations. Only a few larger collagen fibers were detected by these tools and their performance in accurately identifying the orientation of the fibers was compromised. This demonstrates the challenges that image analysis software encounters when images are of suboptimal quality. therefore, for low-quality images both the precision and comprehensiveness of the P-SHG analysis suffer significantly by the loss of detail. Many of the common P-SHG analysis tools are optimized for higher-resolution inputs and often failing to detect finer structures or misinterpret noise as significant features when applied to low-resolution images.

Remarkably, CurveAlign's performance on the ESRGAN-upscaled images is comparable to the original high-quality images, demonstrating significant improvements (Fig. 5.6, 1(c), 2(c)).

The need for our upscaling method instead of doing P-SHG analysis directly on low-resolution images is highlighted by this comparative analysis. Our analysis shows that the upscaled images offer a better approximation of the original high-quality images across multiple metrics. For example, the LBP similarity increased from 0.471 to 0.758, and the FSIM improved from 0.884 (low quality) to 0.910 (Ultrasharp_4X). Upscaling achieves a balance between noise reduction and detail preservation, even though it does not recover all fine details.

The importance of this upscaling technique is evident from the notable improvements in fiber orientation discernibility shown in Fig. 5.6 (1c, 2c). These improvements are essential for precise P-SHG analysis because they improve collagen structure differentiation and make orientation measurements more accurate. Our method provides a workable solution to the trade-off between imaging speed and analysis accuracy in P-SHG studies by utilizing the speed of low-resolution imaging while producing analysis results that closely resemble those from high-resolution images. To sum up, this GAN-based upscaling technique significantly expands the range of image qualities that CurveAlign software and other tools can be used with, making lower-quality images much more useful for in-depth analysis. It overcomes the disadvantages of lower-quality images and technical limitations of sample preparation by offering an effective solution that combines shorter laser exposure times with image upscaling. It may also pave the way for new opportunities for quick, nondestructive P-SHG imaging in a range of biological applications.

A custom Python program was then used to synchronize the images taken at 18 polarization states, ranging from 0° to 170° degrees in 10-degree increments. The first attempt to get the analysis software to function using low-quality images failed because there was too much detail loss for an accurate analysis. Initially, we tried to perform analyses using low-quality images, but this method ran into serious problems because of the considerable loss of detail, which affected the precision of our analyses. In order overcome this problem, the Ultrasharp_4X model was used to upscale each image separately, improving the clarity and resolution necessary for

precise P-SHG analysis. For processing upscaled P-SHG images, a custom MATLAB script was required [146,212]. This script performs a Fourier transform on intensity measurements taken from various angles using a spatial FFT algorithm. A summary of the analysis's results for 2 different mammary glands are shown in Fig. 5.1.

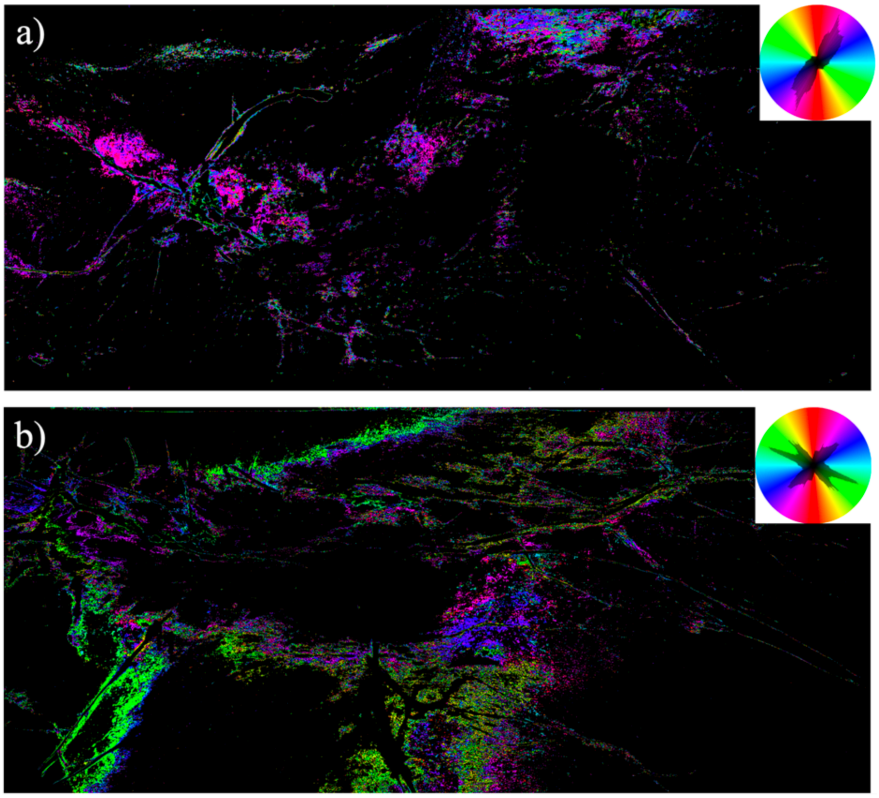

Fig. 5.7 P-SHG imaging of the orientation of collagen fibers in the mammary glands. The SHG signals of two different tissues are shown in panels (a) and (b), with the colours corresponding to the orientations of the collagen fibers in relation to the incident light's polarization angle. These orientations are mapped by the colour wheel insets, which show the complex diverse arrangement of the fibers within the samples. Each colour corresponds to a distinct angle of polarization. Interestingly, both pictures showed dark spots inside the fibers, which were identified as spots where the SHG signal's intensity didn't change. This suggested that the collagen fibers were uniformly oriented across the polarization states that were imaged. Because of this homogeneity, the spatial fast Fourier transform algorithm is unable to identify differences, so no colour assignment occurs in these areas.

18 SHG images (32-bit TIFF) taken in 10-degree increments from 0° to 170° are included in our P-SHG analysis protocol, which is shown in Fig. 6. A visually intuitive representation of the fiber orientation throughout the sample is provided by

the distinct colours assigned to each angle (0-360 degrees). A fibrillar histogram, which provides a quantitative analysis of the fiber orientations, is also included with the images. The analyzed images show some areas that are darker than the originals. Because of the consistent fiber orientation across polarization states, dark areas develop within the fiber network. This is caused by the upscaling algorithm's smoothing effect, which makes it more difficult for the FFT to identify internal fiber variations.

The resulting map of fiber orientations is further processed to plot a histogram of the orientations within the field of view. Since tissue relaxation is minimal during P-SHG image acquisition [146], we can safely quantify parameters from this histogram, specifically, determine the entropy r of this orientation distribution. Using angular bins of 1~ or 10o, r is defined as the typical statistical entropy. It is normalized to be independent of the number of bins $nb(\theta)$ [146]:

$$r = \frac{-1}{Ln[nb(\theta)]} \sum_{\theta=-90^\circ}^{90^\circ} P(\theta)\, Ln[P(\theta)] \qquad 5\text{-}1$$

where $P(\theta)$, which is taken straight from the orientation histogram, is the normalized number of pixels in the image that have the orientation θ. The degree of orientation disorder in the field of view is then evaluated by the entropy r, which decreases toward 0 for thinner orientation distributions and equals 1 for a fully isotropic orientation distribution. As an alternative, the entropy is calculated from orientation maps that are produced by processing the SHG images using the morphological filtering method [43]. Briefly, to reduce the effect of polarization versus fiber orientation on the SHG intensity, all of the SHG images acquired for various linear polarization of the incident beam are added together. The local orientation of the fibres in each pixel is then extracted by a rotating linear structuring element using morphological filtering, as shown by the various colours in Fig. 5.7.

However, in Fig. 5.7, It is important to note that FFT is still able to recognize fiber borders and their periphery. Importantly, the fiber borders were aligned with the

interior, providing a coherent overall fiber direction. This consistency between the interior and border orientations guarantees that the technique still effectively expresses the general directionality of the fibers even in the face of its limitations in identifying internal variations. To overcome the limitations of these smoother, homogeneous sections, a targeted focus on specific internal areas of the fiber is necessary for analyses where these areas are of interest (see Fig. 5.8).

Additionally, in order to improve the clarity and focus of the collagen fiber analysis, background elements and unnecessary muscle structures surrounding the fibers were carefully removed, resulting in dark areas surrounding the sample. The spectrum of colours found in the tissue in Fig. 5.7(a) indicates a network of collagen fibers with different alignments; each colour represents a different fiber orientation with respect to the incident light's polarization angle. These orientations can be interpreted using the colour wheel inset as a guide. With pink tones signifying fibers oriented in one direction and other colours denoting different angles, the vibrant colours imply a diverse and complex arrangement of fibers.

Collagen fiber alignment is shown by a collage of colours in Fig. 5.7(b). The fibers appear to have different orientations than those in the first image, as indicated by the bright green and yellow hues. This sample might have a denser or more aligned collagen network than the first one, based on the colour intensity and distribution. The results, including the color wheel, orientation map, anisotropy parameter map, and histogram data, were meticulously compiled for each sample.

We concentrate on analyzing regions of interest (ROI) that were taken from various samples and their counterparts, which were improved by upscaling, in Fig. 5.8. This analysis is crucial for determining how faithfully upscaling methods maintain the optical and structural characteristics necessary for precise P-SHG analysis. A 20X objective was used to take pictures of the chosen P-SHG ROIs for our analysis. In order to resolve the complex patterns of collagen fiber orientation while maintaining sufficient field coverage, 20X is ideal. Interestingly, the images designated for

upscaling were first captured with a 10X objective, then digitally cropped, and zoomed in.

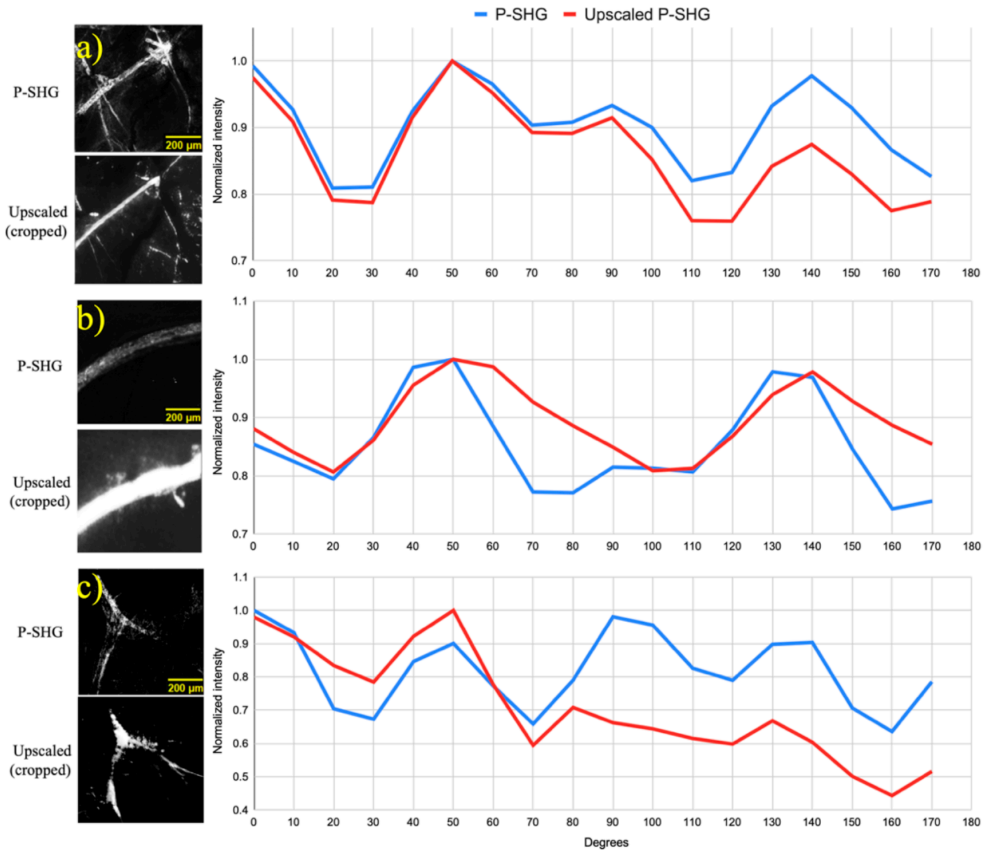

Fig. 5.8 Comparative Analysis of P-SHG in three region of interests (ROI)s. Each row displays original high-quality images (20X objective), low-quality images that were first taken with a 10X objective and then digitally zoomed and cropped, and their GAN-upscaled counterparts. Each row represents a unique ROI from various samples. Upscaling restores smoothness and detail despite the initial lower resolution, producing a fiber orientation analysis that is on the same level with the original high-quality images. The accuracy of collagen fiber orientation details in the upscaled images is confirmed by the normalized intensity vs. laser input angle graphs for each set, which show the consistency of P-SHG responses across all imaging modalities.

In order to replicate a real-world situation where upscaling could be especially helpful, this method was purposefully used for low-quality images to simulate situations in which high-resolution data were not easily accessible or practical to obtain. One important finding when comparing the original and upscaled (but zoomed and cropped) P-SHG images was how smooth the upscaled images were. This smoothness did not detract from the structural details within the images, but rather

enhanced the visual clarity, making the interpretation of collagen fiber orientations more straightforward.

More significantly, we found that the P-SHG response was remarkably consistent when we plotted the normalized intensity against the laser input angle for both the original and upscaled images. Because the upscaling process tends to reduce noise and interpolate between data points to create a more continuous representation of the intensity response, the graph corresponding to the upscaled P-SHG images showed a smoother curve.

Furthermore, the general form and trend of the P-SHG intensity responses did not change, even though the graphs in the upscaled images appeared smoother. This coherence suggests that the upscaling procedure did not change the basic biophysical characteristics recorded by P-SHG imaging, even though it improved the images' visual quality. The usefulness of upscaling as a practical technique for enhancing image quality in P-SHG analysis without sacrificing the accuracy of collagen fiber orientation information was thus highlighted by the validation of the fidelity of fiber orientation details in the upscaled images.

Chapter 6: Conclusion

P-SHG imaging with deep learning-based upscaling offers distinct advantages in specific applications that demand label-free, structurally detailed visualization of collagen architecture. For instance, while differential interference contrast (DIC) microscopy provides valuable phase contrast for general morphology, it lacks the molecular specificity needed to distinguish collagen structures effectively [214]. Similarly, picrosirius red staining enhances collagen birefringence under polarized light, offering a complementary approach for certain analyses, though it requires fixation and staining, which may alter tissue properties and restrict its use in longitudinal studies. In contrast, P-SHG, with its sensitivity to non-centrosymmetric molecular arrangements, combined with ESRGAN, enables rapid acquisition while preserving structural fidelity. This approach is particularly advantageous for applications requiring quantitative analysis of fiber orientation and anisotropy in intact, unstained tissue. While each imaging modality has strengths suited to specific contexts, the proposed P-SHG with ESRGAN framework enhances high-resolution, label-free imaging capabilities, especially where sample preservation, speed, and depth-resolved contrast are priorities.

The inherent trade-offs between spatial resolution, acquisition speed, and the risk of sample damage due to prolonged laser exposure have long constrained the practical deployment of high-resolution biological imaging techniques. While P-SHG imaging is highly effective for visualizing non-centrosymmetric structures such as collagen fibers, achieving high-resolution images over large tissue areas remains time-intensive and technically demanding. In this thesis, we first acquired high-resolution SHG images of whole mammary gland samples to establish a structural reference. To overcome the limitations of P-SHG in large-scale imaging, we then captured low-resolution P-SHG images of the entire sample and applied a novel deep learning-based upscaling strategy. Specifically, we integrated a state-of-the-art ESRGAN (Enhanced Super-Resolution Generative Adversarial Network) model to iteratively upscale the images by a factor of 16×, significantly enhancing both structural detail and perceptual quality while preserving key biological features such as fiber

orientation and anisotropy. This approach enabled a dramatic reduction in acquisition time—from approximately 4.5 hours to just 13.5 minutes—representing more than a 95% improvement, without compromising the integrity of the biological information.

Comprehensive evaluation using both no-reference and full-reference image quality metrics confirmed the method's reliability in preserving key structural features essential for accurate P-SHG analysis. Metrics such as MS-SSIM, PSNR, and NRMSE consistently demonstrated high similarity between the upscaled images and their original high-resolution counterparts, validating the fidelity of the reconstructions. By incorporating this method into the imaging workflow, the traditional trade-off between acquisition speed and spatial resolution is effectively mitigated, enabling rapid acquisition of low-resolution images that can be upscaled to high-quality outputs suitable for detailed biological analysis. The high-resolution SHG images (1800 × 800 pixels) provided detailed visual information, while the low-resolution images (225 × 100 pixels) were enhanced to a resolution of 3600 × 1600 pixels using Ultrasharp_4X, maintaining structural features as validated by CurveAlign analysis (Fig. 5.6). This enhancement is very useful in situations with limited imaging conditions because it minimizes laser exposure times, prevents sample damage, and preserves the chemical and morphological integrity of tissues. The ability to generate high-resolution, high-fidelity images from low-resolution data paves the way for broader applications, including high-throughput imaging, clinical diagnostics, and tissue engineering.

While conventional image quality metrics are sufficient for validating the structural fidelity of upscaled images, they may not fully capture the nuanced features most relevant to biological interpretation. Subtle morphological patterns—such as fiber continuity, alignment, or textural irregularities—are often critical for histological assessment but may be overlooked by general-purpose metrics like MS-SSIM or PSNR. To ensure that AI-enhanced images meet the interpretive standards of clinical and research experts, future efforts should prioritize the development of domain-specific evaluation tools tailored to P-SHG applications. Such metrics would help

bridge the gap between computational validation and expert perception, enabling more confident integration of AI-upscaled images into diagnostic and analytical workflows.

One particularly promising avenue for future development is the integration of this AI-based upscaling approach into multimodal nonlinear imaging pipelines. For instance, combining AI-based P-SHG with techniques like coherent anti-Stokes Raman scattering (CARS) could enable simultaneous visualization of collagen and lipid structures within biological tissues. While P-SHG excels in mapping non-centrosymmetric proteins such as collagen, CARS provides chemically selective imaging of lipids without the need for labeling. The application of ESRGAN-based upscaling to both modalities could enhance spatial resolution and acquisition speed, facilitating high-content, multi-dimensional tissue characterization. Such multimodal strategies hold strong potential for advancing diagnostic accuracy and supporting personalized medicine by revealing interactions between extracellular matrix remodeling and lipid metabolism, particularly in complex pathologies like cancer.

Beyond the technical validation, the potential biological and clinical applications of accelerated P-SHG imaging are substantial. The approach could enable rapid screening of large-scale tissue specimens in pathology, reduce time burdens on clinical imaging workflows, and make advanced diagnostics more widely available in resource-constrained environments. By decreasing imaging time and optical component requirements, our method addresses both throughput and cost barriers, helping to democratize access to advanced nonlinear optical microscopy.

Despite these promising outcomes, several challenges remain. Finer internal variations within fibers may be obscured by the smoothing and interpolation that the upscaling process sometimes introduces, especially in uniform regions. Future developments in deep learning models could address these issues by concentrating on maintaining internal structural fidelity without compromising noise reduction, even though the approach is excellent at maintaining overall orientation and boundary details. Future work should explore the limitations of applying pre-trained networks

to more diverse tissue types, such as muscle and tendon samples. While our results indicate strong performance in mammary gland tissues, domain-specific artifacts or failures may arise in unfamiliar biological contexts. Additional studies are needed to test the robustness and reliability of this method in such scenarios.

Furthermore, the qualitative usefulness of upscaled images for expert interpretation—such as visual assessment by pathologists or biologists—requires further validation. Controlled studies comparing diagnostic outcomes using original high-resolution images and upscaled counterparts could help determine whether AI-enhanced images can substitute or augment traditional imaging workflows in real clinical or research settings.

In conclusion, this thesis presents a validated framework that combines nonlinear optical imaging with deep learning to achieve high-resolution, rapid, and cost-effective imaging of biological tissues. The use of ESRGAN-based upscaling significantly reduces acquisition time without compromising critical image features, and the methodology has been carefully evaluated using structural similarity metrics and lower-cost optical components. With further development and validation, this approach has the potential to expand the practical reach of P-SHG imaging, support automation in histopathology, and contribute to high-throughput, label-free diagnostics and tissue research. By integrating AI with optical microscopy, this work represents a meaningful advancement toward faster, more accessible, and scalable biomedical imaging.

References

1. R. Hooke, Micrographia, or, some physiological descriptions of minute bodies made by magnifying glasses, with observations and inquiries thereupon, Printed by J. Martyn and J. Allestry, London, (1665).
2. J. R. Porter, "Antony van Leeuwenhoek: tercentenary of his discovery of bacteria," Bacteriological reviews, 40(2), (1976) 260-269.
3. A. van Leeuwenhoek, Den Waaragtigen Omloop des Bloeds. London, (1688).
4. M. F. X. Bichat, "Traite des membranes en general et de diverses membranes en particulier," M´equignon-Marvis, Gabon, Paris, (1827).
5. C. R. Virchow, "Die Cellularpathologie in ihrer Begru¨ndung auf physiologische und pathologische Gewebelehre." van August Hirschwald, Berlin, Germany, (1858).
6. A. R. Hall, "The Leeuwenhoek Lecture," (1988), Antoni Van Leeuwenhoek 1632-1723, Notes and Records, 43(2), (1989) 249–273.
7. Ruzin, S. E. (2024). *Techniques in Light Microscopy*. Oxford University Press.
8. T. H. Maiman, "Stimulated optical radiation in Ruby," Nature, 187(4736), (1960) 493–494.
9. D. Spence, P. Kean, and W. Sibbett, "60-fsec pulse generation from a self-mode-locked Ti: sapphire laser," Optics Letters, 16(1), (1991) 42–44.
10. W. S. Boyle and G. E. Smith, "Charge coupled semiconductor devices," Bell System Technical Journal, 49, (1970) 593–600.
11. S. Cova, M. Ghioni, A. Lacaita, C. Samori, and F. Zappa, "Avalanche photodiodes and quenching circuits for single-photon detection," Applied Optics, 35(12), (1996) 1956–1976.
12. B. Huang, M. Bates, and X. Zhuang, "Super-resolution fluorescence microscopy," Annual Review of Biochemistry, 78(1), (2009) 993–1016.
13. D. J. Stephens and V. J. Allan, "Light microscopy techniques for live cell imaging," Science, 300 (5616), (2003) 82–86.
14. B. R. Masters and P. T. C. So, eds., "Handbook of biomedical nonlinear optical microscopy," Oxford University Press, (2008).
15. M. Goppert-Mayer, "Uber Elementarakte mit zwei Quantensprungen," Annalen der Physik, 401(3), (1931) 273–294.
16. P. A. Franken, A. E. Hill, C. W. Peters, and G. Weinreich, "Generation of optical harmonics," Physical Review Letters, 7(4), (1961) 118–119.
17. R. Hellwarth and P. Christensen, "Nonlinear optical microscopic examination of structure in poly-crystalline ZnSe," Optics Communications, 12(3), (1974) 318–322.
18. P. J. Campagnola and C. Y. Dong, "Second harmonic generation microscopy: Principles and applications to disease diagnosis," Laser and Photonics Reviews, 5(1), (2011) 13–26.
19. B. Weigelin, G.-J. Bakker, and P. Friedl, "Third harmonic generation microscopy of cells and tissue organization," Journal of Cell Science, 129(2), (2016) 245–255.
20. E. O. Potma and X. S. Xie, "CARS for biology and medicine," Optics and Photonics News 15, (2004) 40–45.
21. R. C. Prince, R. R. Frontiera, and E. O. Potma, "Stimulated Raman scattering: from bulk to nano," Chemical Reviews, 117(7), (2016) 5070–5094.
22. P. T. C. So, C. Y. Dong, B. R. Masters, and K. M. Berland, "Two-photon excitation fluorescence microscopy," Annual Review of Biomedical Engineering, 2, (2000) 399–429.

23. Y. Han, J. Hsu, N.-H. Ge, and E. O. Potma, “Polarization-sensitive sum-frequency generation microscopy of collagen fibers,” Journal of Physical Chemistry B, 119(8), (2015) 3356–3365.
24. J. Brocious and E. O. Potma, “Lighting up micro-structured materials with four-wave mixing microscopy,” Materials Today, 16(9), (2013) 344–350.
25. B. R. Masters, P. T. C. So, and E. Gratton, “Multiphoton excitation fluorescence microscopy and spectroscopy of in vivo human skin,” Biophysical Journal, 72(6), (1997) 2405–2412.
26. J. T. Trachtenberg, B. E. Chen, G. W. Knott, G. Feng, J. R. Sanes, E. Welker, and K. Svoboda, “Long-term in-vivo imaging of experience-dependent synaptic plasticity in adult cortex,” Nature, 420, (2002) 788–94.
27. J. M. Squirrell, D. L. Wokosin, J. G. White, and B. D. Bavister, “Long-term two-photon fluorescence imaging of mammalian embryos without compromising viability,” Nature Biotechnology, 17(8), (1999) 763–767.
28. A. Karunendiran, R. Cisek, D. Tokarz, V. Barzda, and B. A. Stewart, “Examination of Drosophila eye development with third harmonic generation microscopy,” Biomedical Optics Express, 8(10), (2017) 4504–4513.
29. A. Tuer, D. Tokarz, N. Prent, R. Cisek, J. Alami, D. J. Dumont, L. Bakueva, J. Rowlands, and V. Barzda, “Nonlinear multicontrast microscopy of hematoxylin-and-eosin-stained histological sections,” Journal of Biomedical Optics, 15(2), (2010) 026018.
30. S.-W. Chu, I.-H. Chen, T.-M. Liu, P. C. Chen, C.-K. Sun, and B.-L. Lin, “Multimodal nonlinear spectral microscopy based on a femtosecond Cr:forsterite laser,” Optics Letters, 26(23), (2001) 1909.
31. L. Kontenis, M. Samim, S. Krouglov, and V. Barzda, “Third-harmonic generation Stokes-Mueller polarimetric microscopy,” Optics Express, 25(12), (2017)13174.
32. A. Golaraei, R. Cisek, S. Krouglov, R. Navab, C. Niu, S. Sakashita, K. Yasufuku, M.-S. Tsao, B. C. Wilson, and V. Barzda, “Characterization of collagen in non-small cell lung carcinoma with second harmonic polarization microscopy,” Biomedical Optics Express, 5(10), (2014) 3562–3567.
33. D. Tokarz, R. Cisek, A. Golaraei, S. L. Asa, V. Barzda, and B. C. Wilson, “Ultrastructural fea- tures of collagen in thyroid carcinoma tissue observed by polarization second harmonic generation microscopy,” Biomedical Optics Express, 6(9), (2015) 3475–81.
34. H. Bao, A. Boussioutas, R. Jeremy, S. Russell, and M. Gu, “Second harmonic generation imaging via nonlinear endomicroscopy,” Optics Express, 18(2), (2010) 1255–1260.
35. S. Roth and I. Freund, “Second harmonic generation in collagen,” Journal of Chemical Physics, 70(4), (1979) 1637–1643.
36. I. Gusachenko, V. Tran, Y. G. Houssen, J. M. Allain, and M.-C. Schanne-Klein, “Polarization- resolved second-harmonic generation in tendon upon mechanical stretching,” Biophysical Journal, 102(9), (2012) 2220–2229.
37. F. Tiaho, G. Recher, and D. Rou`ede, “Estimation of helical angles of myosin and collagen by second harmonic generation imaging microscopy,” Optics Express, 15(9), (2007) 12286–12295.
38. P. J. Su, W. L. Chen, Y. F. Chen, and C. Y. Dong, “Determination of collagen nanostructure from second-order susceptibility tensor analysis,” Biophysical Journal, 100(8), 2053–2062, (2011).
39. S. R. Oakes, H. N. Hilton, C. J. Ormandy, “The alveolar switch: coordinating the proliferative cues and cell fate decisions that drive the formation of lobuloalveoli from ductal epithelium,” Breast cancer research: BCR, 8 (2006) 207-207.

40. K. Bach, S. Pensa, M. Grzelak, J. Hadfield, D. J. Adams, J. C. Marioni, W. T. Khaled, "Differentiation dynamics of mammary epithelial cells revealed by single-cell RNA sequencing," Nature communications, 8 (2017) 1-11.
41. C. Frantz, K. M. Stewart, V. M. Weaver, "The extracellular matrix at a glance," Journal of cell science, 123 (2010) 4195-4200.
42. W. Chen, W. Wei, L. Yu, Z. Ye, F. Huang, L. Zhang, S. Hu, C. Cai, "Mammary development and breast cancer: a notch perspective," Journal of mammary gland biology and neoplasia, 26 (2021) 309-320.
43. J. J. Poole, L. B. Mostaço-Guidolin, "Optical microscopy and the extracellular matrix structure: a review," Cells, 10 (2021) 1760.
44. J. R. Reed, K. L. Schwertfeger, "Immune cell location and function during post-natal mammary gland development," Journal of mammary gland biology and neoplasia, 15 (2010) 329-339.
45. P. Schedin, P. J. Keely, "Mammary gland ECM remodeling, stiffness, and mechanosignaling in normal development and tumor progression," Cold Spring Harbor perspectives in biology, 3 (2011) a003228.
46. P. Lu, K. Takai, V. M. Weaver, Z. Werb, "Extracellular matrix degradation and remodeling in development and disease," Cold Spring Harbor perspectives in biology, 3 (2011) a005058.
47. T. Rozario, D. W. DeSimone, "The extracellular matrix in development and morphogenesis: a dynamic view," Developmental biology, 341 (2010) 126-140.
48. D. A. Parry, & A. S. Craig, "Growth and development of collagen fibrils in connective tissue," Ultrastructure of the connective tissue matrix. Boston, MA: Springer US, (1984).
49. J. Bella, & D. J. Hulmes, "Fibrillar collagens," Fibrous proteins: structures and mechanisms, 457-490, (2017).
50. M. D. Shoulders, R. T. Raines, "Collagen structure and stability," Annual review of biochemistry, 78 (2009) 929-958.
51. R. Cisek, A. Joseph, M. Harvey, D. Tokarz, "Polarization-sensitive second harmonic generation microscopy for investigations of diseased collagenous tissues," Frontiers in Physics, 9 (2021) 726996.
52. K. E. Kadler, C. Baldock, J. Bella, R. P. Boot-Handford, "Collagens at a glance," Journal of cell science, 120 (2007) 1955-1958.
53. T. J. Wess, "Collagen fibril form and function," Advances in protein chemistry, 70 (2005) 341-374.
54. I. N. Amirrah, Y. Lokanathan, I. Zulkiflee, M.M.R. Wee, A. Motta, M. B. Fauzi, "A comprehensive review on collagen type I development of biomaterials for tissue engineering: From biosynthesis to bioscaffold," Biomedicines, 10 (2022) 2307.
55. J. Brinckmann, "Collagens at a glance, Collagen: primer in structure," processing and assembly, (2005) 1-6.
56. P.-J. Su, W.-L. Chen, Y.-F. Chen, C.-Y. Dong, "Determination of collagen nanostructure from second-order susceptibility tensor analysis," Biophysical journal, 100 (2011) 2053-2062.
57. Y. Komai, T. Ushiki, "The three-dimensional organization of collagen fibrils in the human cornea and sclera," Investigative ophthalmology & visual science, 32 (1991) 2244-2258.
58. N. Mazumder, N. K. Balla, G. Y. Zhuo, Y. V. Kistenev, R. Kumar, F. J. Kao, ... & N. A. Krivova, "Label-free non-linear multimodal optical microscopy—basics, development, and applications," Frontiers in Physics, 7, (2019)170.
59. V. Magidson, & A. Khodjakov, "Circumventing photodamage in live-cell microscopy," Methods in cell biology, 114 (2013) 545-560.

60. I. Freund, M. Deutsch, “Second-harmonic microscopy of biological tissue,” Optics letters, 11 (1986) 94-96.
61. Y. Ezura, S. Chakravarti, Å. Oldberg, I. Chervoneva, D. E. Birk, “Differential expression of lumican and fibromodulin regulate collagen fibrillogenesis in developing mouse tendons,” The Journal of cell biology, 151 (2000) 779-788.
62. A. Aghigh, J. Cardot, M.S. Mohammadi, G. Jargot, H. Ibrahim, I. Plante, F. Légaré, “Accelerating whole-sample polarization-resolved second harmonic generation imaging in mammary gland tissue via generative adversarial networks,” Biomedical Optics Express, 15 (2024) 5251-5271.
63. P. Stoller, K. M. Reiser, P. M. Celliers, A. M. Rubenchik, “Polarization-modulated second harmonic generation in collagen,” Biophysical journal, 82 (2002) 3330-3342.
64. P. Stoller, P. M. Celliers, K. M. Reiser, A. M. Rubenchik, “Quantitative second-harmonic generation microscopy in collagen,” Applied optics, 42 (2003) 5209-5219.
65. B. K. Robinson, E. Cortes, A. J. Rice, M. Sarper, and del A. Río Hernández, “Quantitative analysis of 3D extracellular matrix remodelling by pancreatic stellate cells.” Biology open, 5(6), (2016) 875-882.
66. O. Nadiarnykh, R. LaComb, P. J. Campagnola, W. A. Mohler, “Coherent and incoherent SHG in fibrillar cellulose matrices,” Optics express, 15 (2007) 3348-3360.
67. R. M. Williams, W. R. Zipfel, W. W. Webb, “Interpreting second-harmonic generation images of collagen I fibrils,” Biophysical journal, 88 (2005) 1377-1386.
68. J. Mertz, L. Moreaux, “Second-harmonic generation by focused excitation of inhomogeneously distributed scatterers,” Optics communications, 196 (2001) 325-330.
69. F. Tiaho, G. Recher, D. Rouède, “Estimation of helical angles of myosin and collagen by second harmonic generation imaging microscopy,” Optics express, 15 (2007) 12286-12295.
70. A. E. Tuer, S. Krouglov, N. Prent, R. Cisek, D. Sandkuijl, K. Yasufuku, B. C. Wilson, V. Barzda, “Nonlinear optical properties of type I collagen fibers studied by polarization dependent second harmonic generation microscopy,” The Journal of Physical Chemistry B, 115 (2011) 12759-12769.
71. S. V. Plotnikov, A. C. Millard, P. J. Campagnola, W. A. Mohler, “Characterization of the myosin-based source for second-harmonic generation from muscle sarcomeres,” Biophysical journal, 90 (2006) 693-703.
72. V. Nucciotti, C. Stringari, L. Sacconi, F. Vanzi, L. Fusi, M. Linari, G. Piazzesi, V. Lombardi, F.S. Pavone, “Probing myosin structural conformation in vivo by second-harmonic generation microscopy,” Proceedings of the National Academy of Sciences, 107 (2010) 7763-7768.
73. K. E. Kadler, D. F. Holmes, J. A. Trotter, J. A. Chapman, “Collagen fibril formation,” Biochemical Journal, 316 (1996) 1-11.
74. S. Bancelin, C. Aimé, I. Gusachenko, L. Kowalczuk, G. Latour, T. Coradin, and M. C. Schanne-Klein, “Determination of collagen fibril size via absolute measurements of second-harmonic generation signals,” Nature Communications, 5 (4920), (2014) 1-8.
75. R. LaComb, O. Nadiarnykh, S. S. Townsend, P. J. Campagnola, “Phase matching considerations in second harmonic generation from tissues: effects on emission directionality, conversion efficiency and observed morphology,” Optics communications, 281 (2008) 1823-1832.
76. L. Tian, H. Wei, Y. Jin, H. Liu, Z. Guo, X. Deng, “Backward emission angle of microscopic second-harmonic generation from crystallized type I collagen fiber,” Journal of biomedical optics, 16 (2011) 075001-075008.

77. M. M. Fejer, G. Magel, D.H. Jundt, R.L. Byer, “Quasi-phase-matched second harmonic generation: tuning and tolerances,” IEEE Journal of quantum electronics, 28 (1992) 2631-2654.
78. M. Rivard, M. Laliberté, A. Bertrand-Grenier, C. Harnagea, C.P. Pfeffer, M. Vallières, Y. St-Pierre, A. Pignolet, M.A. El Khakani, F. Légaré, “The structural origin of second harmonic generation in fascia,” Biomedical optics express, 2 (2010) 26-36.
79. T. Yasui, Y. Tohno, T. Araki, “Determination of collagen fiber orientation in human tissue by use of polarization measurement of molecular second-harmonic-generation light,” Applied optics, 43 (2004) 2861-2867.
80. R. Hristu, S.G. Stanciu, D.E. Tranca, G.A. Stanciu, “Improved quantification of collagen anisotropy with polarization-resolved second harmonic generation microscopy,” Journal of Biophotonics, 10 (2017) 1171-1179.
81. Y. LeCun, Y. Bengio, G. Hinton, “Deep learning,” nature, 521 (2015) 436-444.
82. Y. Yuan, L. Mou, X. Lu, “Scene recognition by manifold regularized deep learning architecture,” IEEE transactions on neural networks and learning systems, 26 (2015) 2222-2233.
83. R. Chalasani, J. C. Principe, “Context dependent encoding using convolutional dynamic networks,” IEEE Transactions on Neural Networks and Learning Systems, 26 (2014) 1992-2004.
84. L. Deng, D. Yu, “Deep learning: methods and applications, Foundations and trends,” signal processing, 7 (2014) 197-387.
85. F. Xing, L. Yang, “Robust nucleus/cell detection and segmentation in digital pathology and microscopy images: a comprehensive review,” IEEE reviews in biomedical engineering, 9 (2016) 234-263.
86. A. Krizhevsky, I. Sutskever, G. E. Hinton, “Imagenet classification with deep convolutional neural networks,” Advances in neural information processing systems, 25 (2012).
87. G. Hinton, L. Deng, D. Yu, G.E. Dahl, A.-r. Mohamed, N. Jaitly, A. Senior, V. Vanhoucke, P. Nguyen, T.N. Sainath, “Deep neural networks for acoustic modeling in speech recognition: The shared views of four research groups,” IEEE Signal processing magazine, 29 (2012) 82-97.
88. S. Min, B. Lee, S. Yoon, “Deep learning in bioinformatics,” Briefings in bioinformatics, 18 (2017) 851-869.
89. M. Veta, P.J. Van Diest, S.M. Willems, H. Wang, A. Madabhushi, A. Cruz-Roa, F. Gonzalez, A.B. Larsen, J.S. Vestergaard, A.B. Dahl, “Assessment of algorithms for mitosis detection in breast cancer histopathology images,” Medical image analysis, 20 (2015) 237-248.
90. J. Ma, R.P. Sheridan, A. Liaw, G.E. Dahl, V. Svetnik, “Deep neural nets as a method for quantitative structure–activity relationships,” Journal of chemical information and modeling, 55 (2015) 263-274.
91. Y. LeCun, Y. Bengio, and G.Hinton, “Deep learning,” Nature, 521(7553), (2015) 436-444.
92. Y. LeCun, L. Bottou, Y. Bengio, P. Haffner, “Gradient-based learning applied to document recognition,” Proceedings of the IEEE, 86 (1998) 2278-2324.
93. A. Krizhevsky, I. Sutskever, G.E. Hinton, “ImageNet classification with deep convolutional neural networks,” Communications of the ACM, 60 (2017) 84-90.
94. R. Girshick, J. Donahue, T. Darrell, J. Malik, “Rich feature hierarchies for accurate object detection and semantic segmentation,” Proceedings of the IEEE conference on computer vision and pattern recognition, (2014), 580-587.

95. H. Greenspan, B. Van Ginneken, R.M. Summers, "Guest editorial deep learning in medical imaging: Overview and future promise of an exciting new technique," IEEE Transactions on Medical Imaging, 35 (2016) 1153-1159.
96. Y. LeCun, K. Kavukcuoglu, C. Farabet, "Convolutional networks and applications in vision," Proceedings of 2010 IEEE international symposium on circuits and systems, IEEE, (2010), 253-256.
97. M. Mohammed, M.B. Khan, E.B.M. Bashier, "Machine learning: algorithms and applications," Crc Press, (2016).
98. H. Lee, R. Grosse, R. Ranganath, A.Y. Ng, "Convolutional deep belief networks for scalable unsupervised learning of hierarchical representations," Proceedings of the 26th annual international conference on machine learning, (2009), 609-616.
99. F. Xing, Y. Xie, H. Su, F. Liu, L. Yang, "Deep learning in microscopy image analysis: A survey," IEEE transactions on neural networks and learning systems, 29 (2017) 4550-4568.
100. P. Nandal, S. Pahal, A. Khanna, P. R. Pinheiro, "Super-resolution of medical images using real ESRGAN," IEEE Access, (2024).
101. P. Shamsolmoali, M. Zareapoor, E. Granger, H. Zhou, R. Wang, M.E. Celebi, J. Yang, "Image synthesis with adversarial networks: A comprehensive survey and case studies," Information Fusion, 72 (2021) 126-146.
102. T. Iqbal, H. Ali, "Generative adversarial network for medical images (MI-GAN)," Journal of medical systems, 42 (2018) 231.
103. C. Ledig, L. Theis, F. Huszár, J. Caballero, A. Cunningham, A. Acosta, A. Aitken, A. Tejani, J. Totz, Z. Wang, "Photo-realistic single image super-resolution using a generative adversarial network," Proceedings of the IEEE conference on computer vision and pattern recognition, (2017), 4681-4690.
104. X. Wang, K. Yu, S. Wu, J. Gu, Y. Liu, C. Dong, Y. Qiao, C. Change Loy, "ESRGAN: Enhanced super-resolution generative adversarial networks," Proceedings of the European conference on computer vision (ECCV) workshops, (2018).
105. K. Jiang, Z. Wang, P. Yi, G. Wang, T. Lu, J. Jiang, "Edge-enhanced GAN for remote sensing image superresolution," IEEE Transactions on Geoscience and Remote Sensing, 57 (2019) 5799-5812.
106. D. Mahapatra, B. Bozorgtabar, S. Hewavitharanage, R. Garnavi, "Image super resolution using generative adversarial networks and local saliency maps for retinal image analysis," Medical Image Computing and Computer Assisted Intervention− MICCAI 2017: 20th International Conference, Quebec City, QC, Canada, September 11-13, (2017), Proceedings, Part III 20, Springer, (2017), 382-390.
107. F. Helmchen, W. Denk, "Deep tissue two-photon microscopy," Nature methods, 2 (2005) 932-940.
108. F. S. Pavone, P. J. Campagnola, "Second harmonic generation imaging," CRC Press Boca Raton, 2014.
109. M. Göppert-Mayer, "Über elementarakte mit zwei quantensprüngen," Annalen der Physik," 401 (1931) 273-294.
110. P. Franken, A.E. Hill, C.e. Peters, G. Weinreich, "Generation of optical harmonics," Physical review letters, 7 (1961) 118.
111. A. Aghigh, S. Bancelin, M. Rivard, M. Pinsard, H. Ibrahim, F. Légaré, "Second harmonic generation microscopy: a powerful tool for bio-imaging," Biophysical Reviews, 15 (2023) 43-70.
112. K. E. Rieckhoff, W. L. Peticolas, "Optical second-harmonic generation in crystalline amino acids," Science, 147 (1965) 610-611.

113. S. Fine, W. Hansen, "Optical second harmonic generation in biological systems," Applied optics, 10 (1971) 2350-2353.
114. J. Gannaway, C. Sheppard, "Second-harmonic imaging in the scanning optical microscope," Optical and Quantum Electronics, 10 (1978) 435-439.
115. C. Sheppard, J. Gannaway, R. Kompfner, D. Walsh, "The scanning harmonic optical microscope," IEEE Journal of Quantum electronics, 13 (1977) 912-912.
116. W. Denk, J. H. Strickler, W. W. Webb, "Two-photon laser scanning fluorescence microscopy," Science, 248 (1990) 73-76.
117. R.W. Boyd, A.L. Gaeta, E. Giese, "Nonlinear optics, in: Springer Handbook of Atomic, Molecular, and Optical Physics," Springer, (2008), 1097-1110.
118. G. Cox, "Biological applications of second harmonic imaging," Biophysical reviews, 3 (2011) 131-141.
119. P. J. Campagnola, H. A. Clark, W. A. Mohler, A. Lewis, L. M. Loew, "Second-harmonic imaging microscopy of living cells," Journal of biomedical Optics, 6 (2001) 277-286.
120. E. E. Hoover, J. A. Squier, "Advances in multiphoton microscopy technology," Nature photonics, 7 (2013) 93-101.
121. E. Hemmer, A. Benayas, F. Légaré, F. Vetrone, "Exploiting the biological windows: current perspectives on fluorescent bioprobes emitting above 1000 nm," Nanoscale horizons, 1 (2016) 168-184.
122. G. Hall, K. B. Tilbury, K. R. Campbell, K. W. Eliceiri, P. J. Campagnola, "Experimental and simulation study of the wavelength dependent second harmonic generation of collagen in scattering tissues," Optics letters, 39 (2014) 1897-1900.
123. S. -W. Chu, I. -H. Chen, T. -M. Liu, P. C. Chen, C. -K. Sun, B. -L. Lin, "Multimodal nonlinear spectral microscopy based on a femtosecond Cr: forsterite laser," Optics letters, 26 (2001) 1909-1911.
124. P. J. Campagnola, L. M. Loew, "Second-harmonic imaging microscopy for visualizing biomolecular arrays in cells, tissues and organisms," Nature biotechnology, 21 (2003) 1356-1360.
125. A.C. Millard, P.J. Campagnola, W. Mohler, A. Lewis, L.M. Loew, "Second harmonic imaging microscopy," Methods in enzymology, Elsevier, (2003), 47-69.
126. X. Chen, O. Nadiarynkh, S. Plotnikov, P. J. Campagnola, "Second harmonic generation microscopy for quantitative analysis of collagen fibrillar structure," Nature protocols, 7 (2012) 654-669.
127. J.A. Squier, M. Müller, G. Brakenhoff, K.R. Wilson, "Third harmonic generation microscopy," Optics express, 3 (1998) 315-324.
128. R. Stolen, A. Ashkin, "Optical Kerr effect in glass waveguide," Applied Physics Letters, 22 (1973) 294-296.
129. F. Shimizu, "Frequency broadening in liquids by a short light pulse," Physical Review Letters, 19 (1967) 1097.
130. M. N. Islam, L. F. Mollenauer, R. H. Stolen, J. R. Simpson, H. -T. Shang, "Cross-phase modulation in optical fibers," Optics letters, 12 (1987) 625-627.
131. M. A. Houle, R. C. Burruss, A. Ridsdale, D. J. Moffatt, F. Légaré, A. Stolow, "Rapid 3D chemical-specific imaging of minerals using stimulated Raman scattering microscopy," Journal of Raman Spectroscopy, 48 (2017) 726-735.
132. I. Gusachenko, V. Tran, Y. G. Houssen, J. -M. Allain, M. -C. Schanne-Klein, "Polarization-resolved second-harmonic generation in tendon upon mechanical stretching," Biophysical journal, 102 (2012) 2220-2229.
133. W. Mohler, A.C. Millard, P.J. Campagnola, "Second harmonic generation imaging of endogenous structural proteins," Methods, 29 (2003) 97-109.

134. P. Fratzl, “Collagen: structure and mechanics, an introduction,” Collagen: structure and mechanics, Springer, (2008), 1-13.
135. D. A. Kleinman, “Theory of second harmonic generation of light,” Physical Review, 128 (1962) 1761.
136. P. Paufler, P. N. Butcher, D. Cotter, “The elements of nonlinear optics,” Cambridge University Press. Cambridge 1990, ISBN 0-521-34183-3, Wiley Online Library, (1991).
137. S. Sioncke, T. Verbiest, A. Persoons, “Second-order nonlinear optical properties of chiral materials,” Materials Science and Engineering: R: Reports, 42 (2003) 115-155.
138. T. Verbiest, S. Houbrechts, M, Kauranen, K. Clays, A. Persoons, “Second-order nonlinear optical materials: recent advances in chromophore design,” J. Mater. Chem, 7 (1997) 2175-2189.
139. A. Golaraei, “Polarimetric second-harmonic generation microscopy for histopathology,” University of Toronto (Canada), (2018).
140. C. Stringari, “Second-Harmonic Generation Imaging of Muscle Tissue”, Citeseer, 2008.
141. C. Odin, T. Guilbert, A. Alkilani, O.P. Boryskina, V. Fleury, Y.L. Grand, “Collagen and myosin characterization by orientation field second harmonic microscopy,” Optics express, 16 (2008) 16151-16165.
142. S. JamesDarian, J. CampagnolaPaul, “Recent advancements in optical harmonic generation microscopy: Applications and perspectives,” BME frontiers, (2021).
143. P. Stoller, B.-M. Kim, A.M. Rubenchik, K.M. Reiser, L.B. Da Silva, “Polarization-dependent optical second-harmonic imaging of a rat-tail tendon,” Journal of biomedical optics, 7 (2002) 205-214.
144. M. Pinsard, S. Laverty, H. Richard, J. Dubuc, M.-C. Schanne-Klein, F. Légaré, “Maturation of the meniscal collagen structure revealed by polarization-resolved and directional second harmonic generation microscopy,” Scientific Reports, 9 (2019) 18448.
145. S. Psilodimitrakopoulos, V. Petegnief, G. Soria, I. Amat-Roldan, D. Artigas, A.M. Planas, P. Loza-Alvarez, “Estimation of the effective orientation of the SHG source in primary cortical neurons,” Optics express, 17 (2009) 14418-14425.
146. G. Ducourthial, J.S. Affagard, M. Schmeltz, X. Solinas, M. Lopez-Poncelas, C. Bonod-Bidaud, R. Rubio-Amador, F. Ruggiero, J.M. Allain, E. Beaurepaire, “Monitoring dynamic collagen reorganization during skin stretching with fast polarization-resolved second harmonic generation imaging,” Wiley Online Library, (2019), e201800336.
147. G. Latour, I. Gusachenko, L. Kowalczuk, I. Lamarre, M.-C. Schanne-Klein, “In vivo structural imaging of the cornea by polarization-resolved second harmonic microscopy,” Biomedical optics express, 3 (2011) 1-15.
148. M. I. Jordan, T. M. Mitchell, “Machine learning: Trends, perspectives, and prospects,” Science, 349 (2015) 255-260.
149. S. Angra, S. Ahuja, “Machine learning and its applications: A review,” international conference on big data analytics and computational intelligence (ICBDAC), IEEE, (2017) 57-60.
150. P. P. Shinde, S. Shah, “A review of machine learning and deep learning applications,” Fourth international conference on computing communication control and automation (ICCUBEA), IEEE, (2018) 1-6.
151. E. S. Brunette, R. C. Flemmer, and C. L. Flemmer, “A review of artificial intelligence,” 4th International Conference on Autonomous Robots and Agents, IEEE, (2009) 385-392.
152. A. M. Turing, “Computing machinery and intelligence”, Mind, 59, (1950) 433-460.
153. S. Hayman, “The mcculloch-pitts model,” International Joint Conference on Neural Networks, Proceedings (Cat. No. 99CH36339) (Vol. 6, 4438-4439), IEEE, (1999).
154. O. L. Hebb, "The organisation of behaviour", Wiley, New York, (1949).

155. F. Rosenblatt, Principles of neurodynamics. perceptrons and the theory of brain mechanisms. Cornell Aeronautical Lab Inc Buffalo NY (1961).
156. B. Widrow, and M. A. Lehr, 30 years of adaptive neural networks: perceptron, madaline, and backpropagation. Proceedings of the IEEE, 78(9), (1990) 1415-1442.
157. M. Chibuluma, J. Kalezhi, "Application of a modified perceptron learning algorithm to monitoring and control," IEEE PES PowerAfrica, IEEE, (2017) 317-321.
158. D. E. Rumelhart, J. L. McClelland, and PDP Research Group, "Parallel distributed processing," volume 1: Explorations in the microstructure of cognition: Foundations. The MIT presses.
159. A. Crisanti, D. J. Amit, and H. Gutfreund, "Saturation level of the Hopfield model for neural network," Europhysics Letters, 2(4), (1986) 337.
160. G. E. Hinton, and T. J. Sejnowski, "Learning and relearning in Boltzmann machines," Parallel distributed processing: Explorations in the microstructure of cognition, 1 (1986) 282-317.
161. C. Cortes, and V.N. Vapnik, "Support Vector Network, Machine learning," 20, (1995) 1-25.
162. Y. Freund, and R. E. Schapire, "A decision-theoretic generalization of on-line learning and an application to boosting," Journal of computer and system sciences, 55(1), (1997) 119-139.
163. L. Breiman, "Random forests," Machine learning, 45 (2001) 5-32.
164. A. Singh, N. Thakur, A. Sharma, "A review of supervised machine learning algorithms," 3rd international conference on computing for sustainable global development (INDIACom), IEEE, (2016)1310-1315.
165. NobelPrize.org. (2024). The 2024 Nobel Prize in Physics. Retrieved from https://www.nobelprize.org/prizes/physics/2024/summary/.
166. I. H. Sarker, "Machine learning: Algorithms, real-world applications and research directions," SN computer science, 2 (2021) 160.
167. W. I. D. Mining, "Data mining: Concepts and techniques," Morgan Kaufinann, 10 (2006) 4.
168. I. H. Sarker, A. Kayes, S. Badsha, H. Alqahtani, P. Watters, A. Ng, "Cybersecurity data science: an overview from machine learning perspective," Journal of Big data, 7 (2020) 1-29.
169. J. Han, J. Pei, H. Tong, Data mining: concepts and techniques, Morgan kaufmann, 2022.
170. Y. Bengio, A. Courville, and P. Vincent, "Representation learning: A review and new perspectives," IEEE transactions on pattern analysis and machine intelligence, 35(8), (2013) 1798-1828.
171. F. Pedregosa, G. Varoquaux, A. Gramfort, V. Michel, B. Thirion, O. Grisel, M. Blondel, P. Prettenhofer, R. Weiss, V. Dubourg, "Scikit-learn: Machine learning in Python," the Journal of machine Learning research, 12 (2011) 2825-2830.
172. H. Mohamed, A. Negm, M. Zahran, O.C. Saavedra, "Assessment of artificial neural network for bathymetry estimation using high resolution satellite imagery in shallow lakes: Case study el burullus lake," International water technology conference, (2015) 12-14.
173. B. Goodfellow, I. Goodfellow, Y. Bengio, A. Courville, Y. Bengio, "Deep learning," MIT press Cambridge, 2016.
174. R. Yasrab, M. P. Pound, A. P. French, T. P. Pridmore, "PhenomNet: bridging phenotype-genotype gap: a CNN-LSTM based automatic plant root anatomization system," bioRxiv, (2020).

175. N. C. Rakotonirina, A. Rasoanaivo, “ESRGAN+: Further improving enhanced super-resolution generative adversarial network,” IEEE International Conference on Acoustics, Speech and Signal Processing (ICASSP), IEEE, (2020) 3637-3641.
176. I. Goodfellow, J. Pouget-Abadie, M. Mirza, B. Xu, D. Warde-Farley, S. Ozair, A. Courville, Y. Bengio, “Generative adversarial networks,” Communications of the ACM, 63 (2020) 139-144.
177. A. Jolicoeur-Martineau, “The relativistic discriminator: a key element missing from standard GAN,” arXiv preprint arXiv:1807.00734, (2018).
178. K. König, P. So, W. Mantulin, E. Gratton, “Cellular response to near-infrared femtosecond laser pulses in two-photon microscopes,” Optics letters, 22 (1997) 135-136.
179. I. Saytashev, S.N. Arkhipov, N. Winkler, K. Zuraski, V.V. Lozovoy, M. Dantus, “Pulse duration and energy dependence of photodamage and lethality induced by femtosecond near infrared laser pulses in Drosophila melanogaster,” Journal of Photochemistry and Photobiology B: Biology, 115 (2012) 42-50.
180. B. R. Masters, P. So, “Handbook of biomedical nonlinear optical microscopy,” Oxford University Press, (2008).
181. J. Mund, D. Fröhlich, D. R. Yakovlev, and M. Bayer, “High-resolution second harmonic generation spectroscopy with femtosecond laser pulses on excitons in Cu_2O,” Physical Review B, 98(8), (2018) 085203.
182. M. D. Peterson, P. L. Hayes, I. S. Martinez, L. C. Cass, J. L. Achtyl, E. A. Weiss and F. M. Geiger, “Second harmonic generation imaging with a kHz amplifier,” Optical Materials Express, 1(1), (2011) 57-66.
183. I.-H. Chen, S.-W. Chu, C.-K. Sun, P.-C. Cheng, B.-L. Lin, “Wavelength dependent damage in biological multi-photon confocal microscopy: a micro-spectroscopic comparison between femtosecond Ti: sapphire and Cr: forsterite laser sources,” Optical and Quantum electronics, 34 (2002) 1251-1266.
184. R. Cisek, L. Spencer, N. Prent, D. Zigmantas, G. S. Espie, V. Barzda, “Optical microscopy in photosynthesis,” Photosynthesis research, 102 (2009) 111-141.
185. O. Nadiarnykh, R. B. LaComb, M. A. Brewer, P. J. Campagnola, “Alterations of the extracellular matrix in ovarian cancer studied by Second Harmonic Generation imaging microscopy,” BMC cancer, 10 (2010) 1-14.
186. I. Plante, M. K. Stewart, D. W. Laird, “Evaluation of Mammary Gland Development and Function in Mouse Models,” Journal of Visualized Experiments, 53 (2011) 2828.
187. S. G. Stanciu, F. J. Ávila, R. Hristu, J. M. Bueno, “A study on image quality in polarization-resolved second harmonic generation microscopy,” Scientific reports, 7 (2017) 15476.
188. H. Katsuno-Kambe, J. L. Teo, R. J. Ju, J. Hudson, S. J. Stehbens, “Collagen polarization promotes epithelial elongation by stimulating locoregional cell proliferation,” Elife, 10 (2021) e67915.
189. J. N. Ouellette, C. R. Drifka, K. B. Pointer, Y. Liu, T. J. Lieberthal, W. J. Kao, J. S. Kuo, A. G. Loeffler, K. W. Eliceiri, “Navigating the collagen jungle: the biomedical potential of fiber organization in cancer,” Bioengineering, 8 (2021) 17.
190. “4x UltraSharp.” OpenModelDB. [Online]. Available: https://openmodeldb.info/models/4x-UltraSharp.
191. “Model Database - Upscale Wiki, [Online]. https://upscale.wiki/w/index.php?title=Model_Database&oldid=1571.
192. “4x UniScaleV2 Sharp,” [Online]. https://openmodeldb.info/models/4x-UniScaleV2-Sharp.
193. “Official Research Models - Upscale Wiki,” [Online]. https://upscale.wiki/wiki/Official_Research_Models.

194. The chaiNNer Organization, “chaiNNer,” [Online]. https://github.com/chaiNNer-org/chaiNNer, Github (2024).
195. R. D. Lutio, S. D'aronco, J. D. Wegner, K. Schindler, “Guided super-resolution as pixel-to-pixel transformation,” Proceedings of the IEEE/CVF international conference on computer vision, (2019) 8829-8837.
196. A. Hore, D. Ziou, “Image quality metrics: PSNR vs. SSIM,” 20th international conference on pattern recognition, IEEE, (2010) 2366-2369.
197. D.M. Rouse, S.S. Hemami, “Understanding and simplifying the structural similarity metric,” 15th IEEE international conference on image processing, IEEE, (2008) 1188-1191.
198. N. Venkatanath, D. Praneeth, M. C. Bh, S. S. Channappayya, S. S. Medasani, “Blind image quality evaluation using perception-based features,” twenty first national conference on communications (NCC), IEEE, (2015)1-6.
199. A. Mittal, R. Soundararajan, A.C. Bovik, “Making a completely blind image quality analyzer,” IEEE Signal processing letters, 20 (2012) 209-212.
200. E. Peli, Contrast in complex images, JOSA A, 7 (1990) 2032-2040.
201. N. Iqbal, R. Mumtaz, U. Shafi, S.M.H. Zaidi, “Gray level co-occurrence matrix (GLCM) texture-based crop classification using low altitude remote sensing platforms,” PeerJ Computer Science, 7 (2021) e536.
202. L. Chen, F. Jiang, H. Zhang, S. Wu, S. Yu, Y. Xie, “Edge preservation ratio for image sharpness assessment,” 12th World Congress on Intelligent Control and Automation (WCICA), IEEE, (2016) 1377-1381.
203. H.R. Sheikh, A.C. Bovik, “Image information and visual quality,” IEEE Transactions on Image Processing, 15 (2006) 430-444.
204. L. Zhang, L. Zhang, X. Mou, D. Zhang, “FSIM: A feature similarity index for image quality assessment,” IEEE Transactions on Image Processing, 20 (2011) 2378-2386.
205. Z. Pan, S. Hu, X. Wu, P. Wang, “Adaptive center pixel selection strategy in local binary pattern for texture classification,” Expert Systems with Applications, 180 (2021) 115123.
206. W. Zhao, R. Chellappa, “Face Processing: Advanced Modeling and Methods,” Elsevier, (2011).
207. T.K. Kim, “Understanding one-way ANOVA using conceptual figures,” Korean Journal of Anesthesiology, 70 (2017) 22-26.
208. G.M. Sullivan, R. Feinn, “Using effect size or why the P value is not enough,” Journal of Graduate Medical Education, 4 (2012) 279-282.
209. Y. Liu, A. Keikhosravi, G. S. Mehta, C. R. Drifka, K. W. Eliceiri, “Methods for quantifying fibrillar collagen alignment,” Fibrosis: Methods and Protocols, (2017) 429-451.
210. Y. Liu, A. Keikhosravi, C. Pehlke, J. Bredfeldt, M. Dutson, H. Liu, G. Mehta, R. Claus, A. Patel, M. Conklin, “Fibrillar collagen quantification with curvelet transform based computational methods,” Frontiers in Bioengineering and Biotechnology, 8 (2020) 198.
211. A. Aghigh, S.E. Preston, G. Jargot, H. Ibrahim, S.V. Del Rincón, F. Légaré, “Nonlinear microscopy and deep learning classification for mammary gland microenvironment studies,” Biomedical Optics Express, 14 (2023) 2181-2195.
212. C. Teulon, I. Gusachenko, G. Latour, M.-C. Schanne-Klein, “Theoretical, numerical and experimental study of geometrical parameters that affect anisotropy measurements in polarization-resolved SHG microscopy,” Optics Express, 23 (2015) 9313-9328.
213. M.C. Chen, W.H.Wang, G. Raju, N. Mazumder, G.Y. Zhuo, “Polarization-Resolved Second-Harmonic Generation for Tissue Imaging.” In: Mazumder, N., Kistenev, Y.V., Borisova, E., Prasada K., S. (eds) Optical Polarimetric Modalities for Biomedical

Research. Biological and Medical Physics, Biomedical Engineering. Springer, Cham (2023).
214. S. M. Siadat, A. A. Silverman, C. A. DiMarzio, & J. W. Ruberti, Measuring collagen fibril diameter with differential interference contrast microscopy. Journal of Structural Biology, 213(1), (2021)107697.